UNIVERSITÀ DEGLI STUDI DI PADOVA

Dipartimento di Fisica e Astronomia “Galileo Galilei”

Master degree in Astrophysics and Cosmology

Final Dissertation

Constraining the Very High-Energy Pulsed Emission from Crab Pulsar with LST-1

Thesis supervisor:
Prof. Elisa Prandini

Candidate:
Irene Albanese

Thesis co-supervisors:
Dr. Rubén López-Coto
Dr. Stefano Menchiari

Academic Year 2024/25

"Non so
Se è soltanto fantasia
O se è solo una follia
Quella stella lontana laggiù
Però
Io la seguo e anche se so
Che non la raggiungerò
Potrò dire
Ci sono anch'io."
Max Pezzali, ne *Il Pianeta Del Tesoro*.

Contents

Abstract 1

Introduction 3

1 Gamma-ray astronomy: an overview 6

- 1.1 Origins of gamma-ray astronomy . . . 6
- 1.2 Emission of gamma rays . . . 9
- 1.3 Sources of gamma rays . . . 9
- 1.4 Detection techniques . . . 16
- 1.5 Multiwavelength connections . . . 20
- 1.6 Multimessenger connections . . . 21

2 Gamma-ray pulsars 22

- 2.1 Pulsars and neutron stars . . . 23
  - 2.1.1 General properties . . . 24
  - 2.1.2 Pulsar population and classification . . . 29
  - 2.1.3 Phaseograms . . . 31
  - 2.1.4 Magnetospheres . . . 33
  - 2.1.5 Emission across the electromagnetic spectrum . . . 36
- 2.2 Pulsars in the gamma-ray regime . . . 37
  - 2.2.1 High-energy regime . . . 37
  - 2.2.2 Very-high energy regime . . . 40
- 2.3 Emission models for gamma-ray pulsars . . . 41
  - 2.3.1 Classical models . . . 44
  - 2.3.2 Current very-high energy models . . . 46
- 2.4 Crab pulsar . . . 52
  - 2.4.1 Crab nebula . . . 53
  - 2.4.2 Pulsed emission . . . 54

3 Imaging Atmospheric Cherenkov Telescopes (IACTs) 58

- 3.1 Cherenkov Telescopes Array Observatory (CTAO) . . . 60

3.1.1 Design and configuration of CTAO 61
3.1.2 Performance and sensitivity 63
3.2 First Large-Sized Telescope (LST-1) 64
3.2.1 Design and configuration of LST-1 65
3.2.2 Commissioning and first results 66
3.3 Impact on pulsar research 66

4 Crab pulsar analysis with LST-1 **68**
4.1 LST analysis chain: an overview 68
4.1.1 Observation modes 70
4.1.2 Data quality selection 71
4.1.3 Low-level analysis 74
4.1.4 Event reconstruction 77
4.1.5 Gamma/hadron separation and cut optimization 78
4.1.6 Instrument Response Functions (IRFs) and DL3 production 80
4.1.7 High-level analysis 82
4.2 Crab pulsar analysis 85
4.2.1 Data quality selection of the Crab pulsar 86
4.2.2 DL2 to DL3 89
4.2.3 DL3 to DL3_pulsar 90
4.2.4 Phaseograms 93
4.2.5 Spectral energy distributions (SEDs) 95

5 Results and discussion **97**
5.1 Phaseogram 97
5.2 Spectral energy distributions (SEDs) of the peaks 100
5.3 Future prospects 107

Conclusions **108**

A Radiative processes **112**

B Cherenkov radiation **117**

C Extensive air showers **120**

Abstract

Pulsars are neutron stars formed from the collapse of massive stars after a supernova explosion. They rotate rapidly and emit pulsed radiation with periods of seconds, or even milliseconds. Their strong magnetic field creates a magnetosphere where particles are accelerated up to very-high energies.

To date, about than 300 gamma-ray pulsars have been detected by *Fermi*-LAT in the high energy range (HE, 100 MeV < E < 100 GeV). However, only two of them, Crab and Vela, have been detected by ground-based Imaging Atmospheric Cherenkov Telescopes (IACTs) at TeV energies. IACTs operate above tens of GeV, where *Fermi*-LAT sensitivity drops. Pulsed emission at TeV energies detected by IACTs challenges existing pulsar emission models, such as the polar cap and the slot gap model, which predict an exponential cutoff at 1 GeV and do not account for a very high-energy (VHE, 100 GeV < E < 100 TeV) component. Thus, new scenarios such as the wind-zone and current-sheet models have been proposed to explain the VHE emission.

To enhance our understanding of gamma-ray emission from pulsars, advanced instrumentation with improved flux sensitivity is required. This calls for a new generation of IACTs, the upcoming Cherenkov Telescope Array Observatory (CTAO). It will comprise telescopes of different sizes and sensitivities. The largest ones are called Large-Sized Telescopes (LSTs) and are optimized for the lowest energies, starting from 20 GeV. The prototype is the LST-1, operational since 2018 and producing first scientific results.

In this work, an analysis of VHE pulsed gamma-ray emission from the Crab pulsar using data from LST-1 of the Northern site of the CTAO is presented. The study aims to detect pulsed emission up to 1 TeV or, alternatively, to establish upper limits on its flux, with the goal of extending previous measurements.

The full dataset, collected between October 2018 and July 2025, corresponds to $\sim$180 hours of observations. Data were processed with the standard LST-1 pipeline and a dedicated pulsar timing package, producing phaseograms and phase-resolved spectra between 20 GeV and 1 TeV.

Both expected peaks were detected with high significance (11.47σ for P1, 11.96σ for P2, and 15.72σ for P1+P2 combined). The phase-resolved spectra are well described by power laws, with spectral indices $\Gamma_{P1} = 3.0 \pm 0.1$ and $\Gamma_{P2} = 2.80 \pm 0.07$. Compared with

previous LST-1 and MAGIC results, this analysis provides one additional spectral point for the first peak P1 (for both MAGIC and LST-1 datasets) and for the second one P2 (only for the LST-1 dataset), extending the measurements up to 1 TeV. The analysis also confirms the compatibility with both LST-1 and MAGIC results.

These findings confirm that the Crab pulsar spectrum shows no clear evidence of a cutoff up to the TeV domain. The next step will be to test whether the observed Crab pulsar emission can be consistently reproduced within the new theoretical models recently proposed for Vela, which may provide more insight into the origin of pulsar emission in the VHE regime. The outcome of this work also highlights the potential of future observations with the array of four LSTs and, eventually, the full CTAO, to detect pulsed VHE emission from the Crab and other gamma-ray pulsars.

Introduction

Gamma-ray astronomy probes the highest-energy electromagnetic regime (> 100 keV), where non-thermal processes dominate and particles are accelerated to relativistic energies (Schönfelder, 2002). It offers the possibility to constrain the origin of cosmic rays (Ter Haar, 1950), to investigate the extreme astrophysical environments in both Galactic sources such as pulsars, supernova remnants, pulsar wind nebulae, TeV halos, binaries, star clusters and superbubbles, and extragalactic sources such as active galactic nuclei, gamma-ray bursts, and starburst galaxies, and to explore fundamental physics questions, including dark matter searches and tests of Lorentz invariance (Schönfelder, 2002). Moreover, in recent years, gamma-ray astronomy has been linked to multiwavelength and multimessenger studies, through radio, optical, and X-ray observations (Illiano et al., 2023) and through neutrino emission (Ansoldi, Antonelli, Arcaro, et al., 2018) and gravitational wave detections (Abbott et al., 2017), to provide a complete picture of the astrophysical processes at work. Energy bands in this field are commonly split into several ranges. This thesis focuses on the very-high-energy regime (VHE, 100 GeV – 100 TeV).

Pulsars are one of the most relevant sources in this field. They are rapidly rotating and highly magnetized neutron stars (Carroll and Ostlie, 2017). Their strong magnetic fields and compactness generate extreme environments such that, in their magnetospheres, particles are accelerated to ultra-relativistic energies, producing pulsed emission that spans the entire electromagnetic spectrum, from radio to gamma rays (Carroll and Ostlie, 2017). Before the launch of *Fermi*-LAT in 2008, only a few detections of pulsars in the gamma-ray regime were confirmed by EGRET (D. J. Thompson, 2008). The Third *Fermi*-LAT Catalog (Smith et al., 2023) lists about 300 gamma-ray pulsars up to $\sim$70 GeV. Their spectra are described by a power law with an exponential cutoff, and typical cutoff energies are near 1 GeV (McCann, 2015).

According to classical models, gamma-ray emission is supposed to originate inside the pulsar magnetosphere. In the polar cap (PC) model (A. K. Harding, 2013), particles are accelerated by strong electric fields near the star surface at the magnetic poles, producing gamma rays via curvature radiation (CR). The outer gap (OG) model (Romani, 1996) assumes that particles are accelerated in vacuum gaps between the null surface and the last closed field lines, radiating via synchro-curvature radiation (SCR). Finally, the slot gap (SG) model

(Arons, 1981) places the acceleration region along the last open magnetic field lines, where the parallel electric field vanishes. Emission occurs through CR and inverse Compton (IC) scattering. All of them predict an exponential cutoff in their spectra, in agreement with *Fermi*-LAT observations.

However, contrary to early expectations (F. Aharonian, A. G. Akhperjanian, et al., 2007), IACTs revealed pulsar emissions at VHE energies. To date, two pulsars are detected above 100 GeV: the Crab pulsar (VERITAS Collaboration, 2011; Aleksić et al., 2012), the main topic of this work, and the Vela pulsar (H. E. S. S. Collaboration, F. Aharonian, et al., 2023). The Crab pulsar, located at the center of the Crab Nebula, is the most studied object of this class. It is not only one of the brightest sources across multiple wavelengths (Lyne, Jordan, et al., 2015) but also the first pulsar detected at energies extending into the TeV range (Ansoldi et al., 2016). These findings challenge classical gamma-ray pulsar models, providing the motivation to propose new mechanisms to explain their emission at such VHE.

Alternative VHE scenarios include the modified OG model, the wind-zone model, and current-sheet model. In particular, H.E.S.S. observations of Vela up to 20 TeV (H. E. S. S. Collaboration, F. Aharonian, et al., 2023) require IC scattering in the Klein–Nishina regime occurring in the equatorial current sheet or in the wind zone, well beyond the light cylinder.

Due to current instrumental limits, only a handful of pulsars are detected above 100 GeV, as mentioned before. The upcoming Cherenkov Telescope Array Observatory (CTAO; Gueta, 2022), expected to improve sensitivity by a factor of 5-10 compared to current Imaging Atmospheric Cherenkov Telescopes (IACTs), with LST-1, the first prototype for Large-Sized Telescopes in the Northern array already operational, will be decisive in probing pulsars in the VHE domain, providing the main motivation for this thesis.

Thus, the aim of this work is to constrain the VHE pulsed emission, up to TeV energies, from the Crab pulsar using all the data collected with LST-1 so far by applying advanced analysis techniques and producing phase-resolved spectra. In particular, the goal is to extend previous results reported by Ansoldi et al. (2016) and Abe et al. (2024) using MAGIC and LST-1, in which they report the emission from the Crab pulsar up to 450 GeV for the first peak P1 and 700 GeV for the second peak P2 (LST-1 results) and 600 GeV for P2 (MAGIC results).

The analysis followed the standard LST-1 pipeline (`lstchain-v0.10.18`; López-Coto et al., 2022, Moralejo et al., 2025), starting from raw data calibration and image cleaning, through event reconstruction and gamma/hadron separation using Random Forests trained on

Monte Carlo simulations, up to the production of DL3 files with instrument response functions (IRFs). Pulsar-specific analysis was then performed with the `PulsarTimingAnalysis` package (Mas and Morcuende, 2024), which corrects photon arrival times to the Solar System barycenter and assigns rotational phases using updated ephemeris. From these datasets, phaseograms and phase-resolved spectra were obtained employing `Gammapy` (Deil et al., 2017; Donath et al., 2023), enabling flux extraction between 20 GeV and 1 TeV for the two emission peaks and contributing to the field by providing the opportunity to test new emission models in the VHE regime.

The thesis is organized as follows. Chapter 1 introduces the field of gamma-ray astronomy, Chapter 2 reviews the main physical properties of pulsars, with particular attention to the VHE pulsar and the Crab pulsar. Chapter 3 presents IACTs, emphasizing the properties of LST-1, while Chapter 4 provides an overview of the LST-1 analysis chain and details the pulsar analysis chain adopted for the Crab pulsar data collected with LST-1. Finally, Chapter 5 reports and discusses the results of the analyzed dataset.

1. Gamma-ray astronomy: an overview

For centuries, astronomical studies relied on observations limited to the optical band, which represent only a small portion of the electromagnetic spectrum. Despite this restriction, major discoveries were achieved. However, most of the Universe remained hidden at other wavelengths. The technological revolution of the past century opened multiple observational windows, each providing unique insights into astrophysical phenomena. Modern astronomy now combines data across all the electromagnetic spectrum, from radio to gamma rays, through multiwavelength observations. This approach has recently expanded into multimessenger astronomy, incorporating neutrinos, gravitational waves, and cosmic rays.

Gamma rays occupy the highest-energy domain of the electromagnetic spectrum, from 100 keV to above 100 PeV, far beyond the reach of thermal processes that dominate optical emission. Their production requires non-thermal mechanisms involving ultrarelativistic particles in extreme environments. The gamma-ray sky features both Galactic and extragalactic sources, described in Section 1.3.

At higher energies, the gamma-ray regime extends over 12 energy decades, subdivided as follows:

- **Low energy (LE)**: below 100 MeV;
- **High energy (HE)**: between 100 MeV and 100 GeV;
- **Very high energy (VHE)**: between 100 GeV and 100 TeV;
- **Ultra high energy (UHE)**: between 100 TeV and 100 PeV;
- **Extreme high energy (EHE)**: above 100 PeV.

Different energy ranges requires different detection techniques due to energy-dependent interaction processes. This thesis focuses on the VHE gamma-ray regime.

1.1 Origins of gamma-ray astronomy

In 1912, Victor Hess (1912) demonstrated that most ionizing radiation measured at Earth originates from space, leading to the discovery of cosmic rays. The cosmic ray spectrum, shown in Fig. 1.1, is well described by a broken power law ($dN/dE \propto E^{-\gamma}$) with the following features: its spectral index is $\gamma \sim 2.7$ up to the so-called knee, located at $\sim 4.5 \times 10^{15}$ eV; beyond it, the spectrum steepens to a spectral index $\gamma \sim 3$, and a second knee appears at $\sim 10^{17}$ eV, where it becomes even softer; at energies above $\sim 4 \times 10^{18}$ eV, the slope flattens again to a spectral index $\gamma \sim 2.6$, up to the ankle; finally, above $4 \times 10^{20} eV$, the spectrum undergoes a sharp suppression.

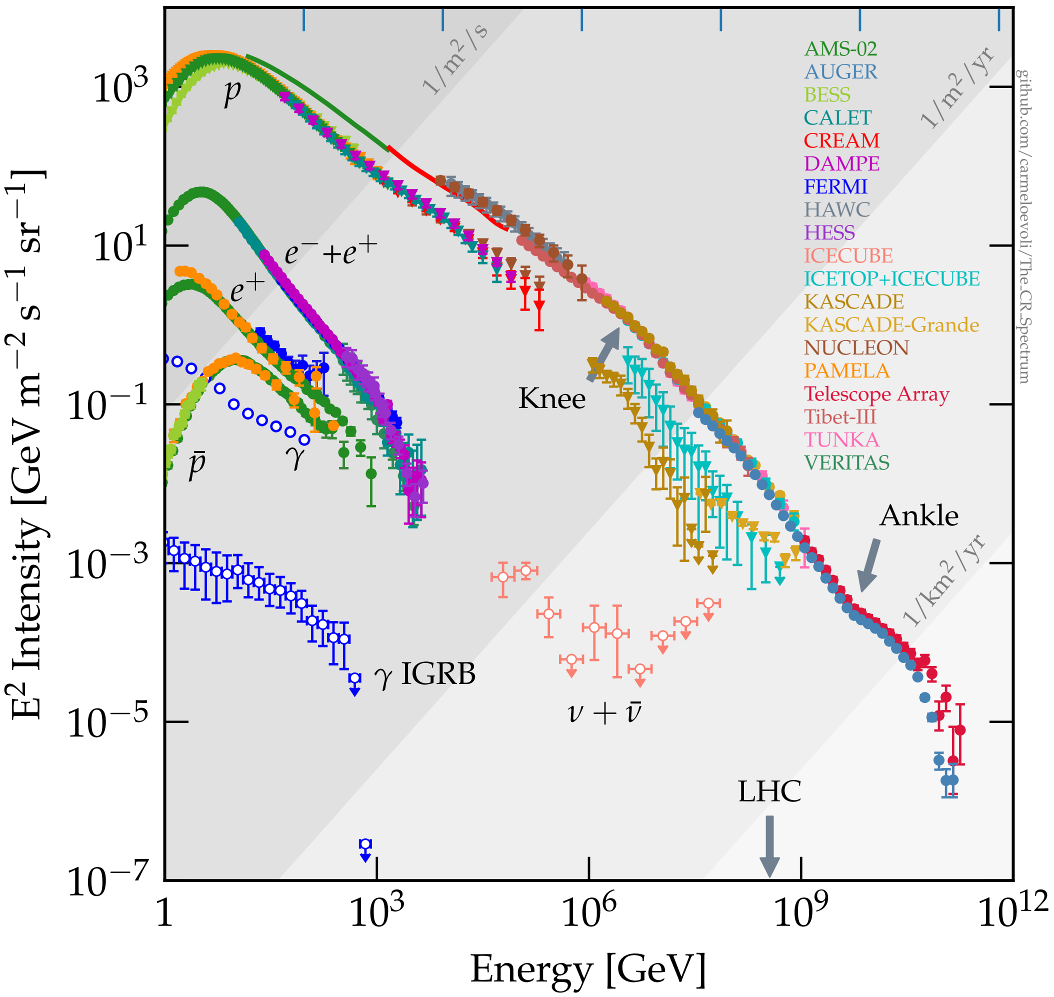

Figure 1.1: Spectrum of cosmic rays measured by several experiments (after 2000). It follows a power law with distinct features: the knee at $\sim 4.5 \times 10^{15}$ eV, the second knee at $\sim 10^{17}$ eV, the ankle at $\sim 4 \times 10^{18}$ eV, and a final suppression above $\sim 4 \times 10^{20}$ eV. The ankle is generally interpreted as the transition to an extragalactic origin rather than a Galactic one.

Credit: Evoli, 2020.

At sub-GeV energies, cosmic rays are largely influenced by Solar System processes. A notable component is the Anomalous Cosmic Rays, accelerated at the solar wind termination shock. At higher energies, up to the ankle, they are generally attributed to Galactic sources. Between the knee and the ankle, the spectrum steepens at the so-called second knee, which is often interpreted as the maximum energy achievable by Galactic accelerators. The ankle is associated with the transition to a predominantly extragalactic origin.

Gamma-ray astronomy emerged in the mid-20th century, when the connection between nuclear reactions, cosmic rays and gamma-ray production was already established. Specifically, processes such as neutral pion decay in hadronic interactions and inverse Compton scattering by relativistic electrons were recognized as channels for gamma-ray emission (see Section 1.2). Several astrophysical objects were expected to emit high-energy photons, but their fluxes were below the sensitivity of early balloon experiments (Morrison, 1958). This limitation drove nuclear physicists to develop dedicated detectors for cosmic gamma rays, linking the rise of gamma-ray astronomy to advances in nuclear physics (Schönfelder, 2002). Opening this observational window was a milestone, enabling the study of non-thermal processes and extreme environments in the Universe. These efforts were driven by three major goals:

1. Identify cosmic-ray sources (e.g., supernova remnants, active galactic nuclei).
2. Probe extreme astrophysical environments and relativistic outflows.
3. Test fundamental physics, including dark matter searches and Lorentz invariance.

Direct detection of gamma rays at ground level is impossible due to atmospheric absorption at that wavelengths. Early balloon experiments (Morrison, 1958) lacked sensitivity, prompting the deployment of satellite detectors. In 1961, Explorer XI detected photons above 50 MeV (William L. Kraushaar and George W. Clark, 1962), marking the birth of gamma-ray astronomy. Later missions such as OSO (Orbiting Solar Observatory) and Vela satellites revealed the first Galactic emissions and gamma-ray bursts (W. L. Kraushaar, G. W. Clark, and G. Garmire, 1969, Klebesadel, Strong, and Olson, 1973).[1] By the 1980s-1990s, improved instrumentation detected active galactic nuclei and pulsars at MeV energies. A short description of space-based telescopes is included in Section 1.4.

---

[1] The Vela satellites were originally military instruments, developed to detect nuclear detonations during the Cold War. The discovery of gamma-ray bursts was therefore completely unexpected.

Parallel efforts developed ground-based methods exploiting atmospheric showers (see Appendix C) induced by gamma rays. Imaging Atmospheric Cherenkov Telescopes (IACTs), detailed in Chapter 3, capture Cherenkov light (see Appendix B) from these showers, enabling energy and direction reconstruction. The Whipple telescope (Cawley et al., 1990) became operational in 1969 and pioneered this technique, leading to the current generation of IACTs.

1.2 Emission of gamma rays

Gamma rays originate from non-thermal processes, as thermal emission would require unrealistically high temperatures ($T > 10^8 K$) for astrophysical sources. Two primary categories of mechanisms exist, depending on the nature of the radiating particles: leptonic and hadronic.

According to leptonic mechanisms, relativistic electrons or positrons emit high-energy photons when accelerated in magnetized environments, as observed in pulsars, the main topic of this work. Main radiative processes (detailed in Appendix A) are synchrotron radiation (SR), curvature radiation (CR), inverse Compton (IC) scattering, synchrotron self-Compton (SSC), and bremsstrahlung emission (Rybicki and Lightman, 1979).

While, according to hadronic models, gamma rays primarily originate from neutral pion decay ($\pi^0 \to \gamma + \gamma$) following collisions between high-energy protons and interstellar medium particles. These interactions can also produce charged pions, which decay into neutrinos via $\pi^+ \to \nu_\mu + \mu^+$ and $\pi^- \to \bar{\nu}_\mu + \mu^-$.

Hadronic and leptonic processes can be distinguished by their spectral signatures, variability properties, and by the presence of neutrinos, which are exclusively produced in hadronic interactions.

1.3 Sources of gamma rays

The number of gamma-ray sources has drastically increased in recent years, mainly due to advances in observational techniques and improved telescope sensitivity. They are typically categorized by their location (Galactic or extragalactic), spatial extent (diffuse, point-like, or extended), and variability (steady or transient).

Diffuse emission

Diffuse emission is produced mainly by the interactions of cosmic rays with matter and radiation fields, and represents one of the dominant components of the gamma-ray sky. It arises both within our Galaxy and on extragalactic scales.

Galactic diffuse emission

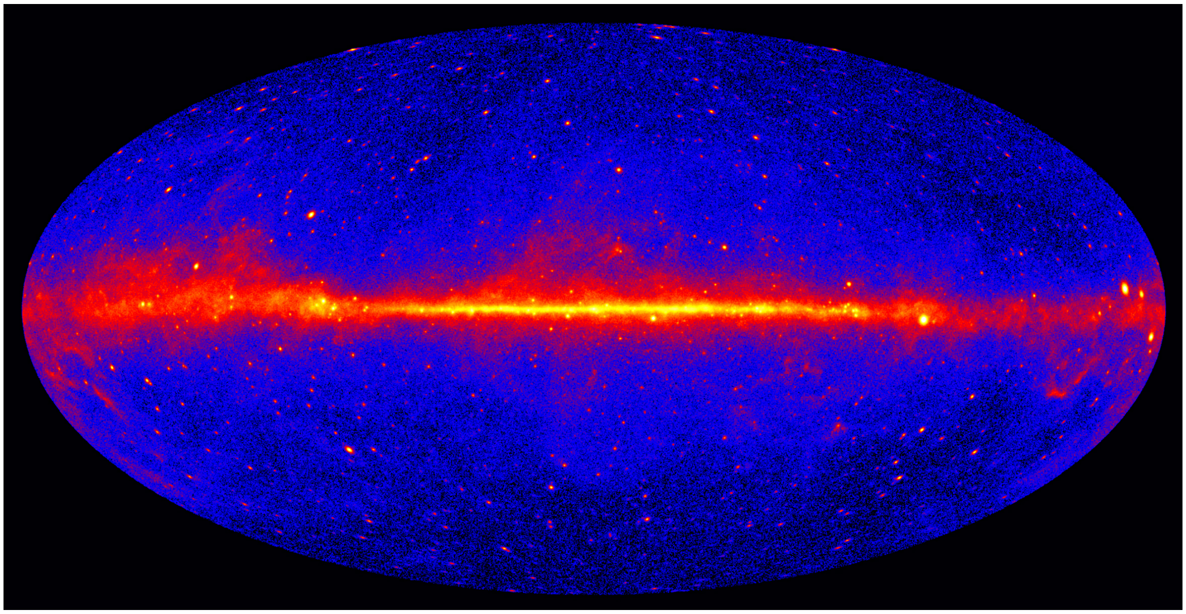

Figure 1.2: This image displays the entire sky at energies above 1 GeV, derived from five years of observations with *Fermi*-LAT. Brighter regions correspond to more intense gamma-ray emission. The points represent the resolved gamma-ray sources, while the diffuse Galactic emission mainly originates from the interactions of cosmic rays with the interstellar medium and radiation fields. While unresolved sources contributing only a minor fraction.
Credit: NASA/DOE/Fermi LAT Collaboration, `https://fermi.gsfc.nasa.gov/ssc/Fermi_5_year.jpg`.

Shown in Fig. 1.2 from *Fermi*-LAT data, it originates from cosmic rays interactions with the interstellar medium and radiation fields (Su, Slatyer, and Finkbeiner, 2010). Recent measurements from LHAASO extend this emission up to PeV energies (Cao, F. Aharonian, An, B. Axikegu Y. X., et al., 2023), while the Tibet ASγ experiment detected emission from 100 TeV to 1 PeV in the Galactic plane (Amenomori, Bao, et al., 2021). Competing models suggest either a uniform cosmic rays spectrum across the Galaxy or spectral hardening near the Galactic center (Vecchiotti et al., 2024, and references therein). Unresolved gamma-ray sources may also contribute to the Galactic diffuse emission (R. Zhang et al., 2023, Menchiari et al., 2025), though this remains under discussion.

Extragalactic diffuse emission

After removing the Galactic diffuse component and resolved extragalactic sources from the gamma-ray sky map, a residual diffuse signal, referred to as the Isotropic Gamma-Ray Background (IGRB), remains. The IGRB has been extensively investigated by *Fermi*-LAT at MeV energies (Ackermann, Ajello, et al., 2015). Because high-energy gamma rays interact with the extragalactic background light (EBL), extragalactic emission is heavily attenuated at multi-TeV energies, leading to the observed cutoff of the IGRB at a few hundred GeV. Several processes may contribute to the IGRB, including faint or unresolved gamma-ray sources and interactions of cosmic rays within fields located in the Galactic halo.

Fermi Bubbles

Observations from the *Fermi*-LAT satellite reveal a large-scale, double-bubble structure extending roughly 50-55 deg from the Galactic Center (Su, Slatyer, and Finkbeiner, 2010). They are also visible in radio and X-ray bands (Ackermann, Albert, et al., 2014), while in the gamma-ray regime, Fermi bubbles exhibit a spectral cutoff near a few hundred GeV. Multiple models have been proposed to explain their origin, including hadronic scenarios, where particles are accelerated near the Galactic Center and transported by AGN, driven or nuclear star formation winds, and leptonic models, supported by the observed microwave emission (Yang, Ruszkowski, and Zweibel, 2018).

Galactic gamma-ray sources

This subsection provides an overview of the most relevant Galactic gamma-ray sources, all shown in Fig. 1.3.

Pulsars

Rapidly rotating neutron stars with strong magnetic fields that produce pulsed emission via leptonic mechanisms. They are a primary focus of current gamma-ray research and the subject of this work. Further details are provided in Chapter 2.

Supernova remnants (SNRs)

Result from core-collapse supernovae, producing shock fronts that can accelerate particles to PeV energies. These are good candidates for Galactic cosmic-ray origins (Ter Haar, 1950) but lack definitive proof as PeVatrons[2] (Cristofari, 2021) despite several detections above 100 TeV (Albert et al., 2020, Tibet ASγ Collaboration et al., 2021).

Pulsar wind nebulae (PWNe)

Structures powered by a central pulsar, where particle acceleration is believed to occur at the termination shock of the relativistic wind of the pulsar. Gamma rays are primarily produced via synchrotron and inverse Compton processes, including synchrotron self-Compton in younger systems. These mechanisms also generate lower-energy radiation, including radio emission (Gaensler and Slane, 2006).

A notable example is the Crab Nebula, detailed in Chapter 2.4.1, which is the most extensively studied PWN. It also serves as a standard calibration source for all modern IACTs (see Chapter 3).

TeV halos

TeV halos are diffuse and extended TeV emission regions surrounding some pulsars. Their emission is attributed to inverse Compton (IC) scattering of background photons by very energetic leptons that were accelerated at the PWN termination shock and subsequently escaped (Linden et al., 2017). They are observed around middle-aged pulsars like Geminga (Abdo, B. Allen, et al., 2007, Abeysekara, Albert, Alfaro, Alvarez, Álvarez, Arceo, et al., 2017) but not in younger systems such as the Crab (Sudoh, Linden, and Beacom, 2019).

Binary systems

These systems consist of a compact object and a massive, typically young companion star. Based on the nature of the compact object, two primary classes are distinguished: microquasars (black hole + companion) like Cygnus X-3 (Fermi LAT Collaboration et al., 2009),

---

[2] A PeVatron is a source of cosmic rays capable of accelerating a significant fraction of particles up to PeV energies.

and pulsar binaries (pulsar + companion). Gamma-ray emission arises from jet interactions or pulsar wind collisions with stellar fields. Their orbital modulation can aid in identifying the compact object.

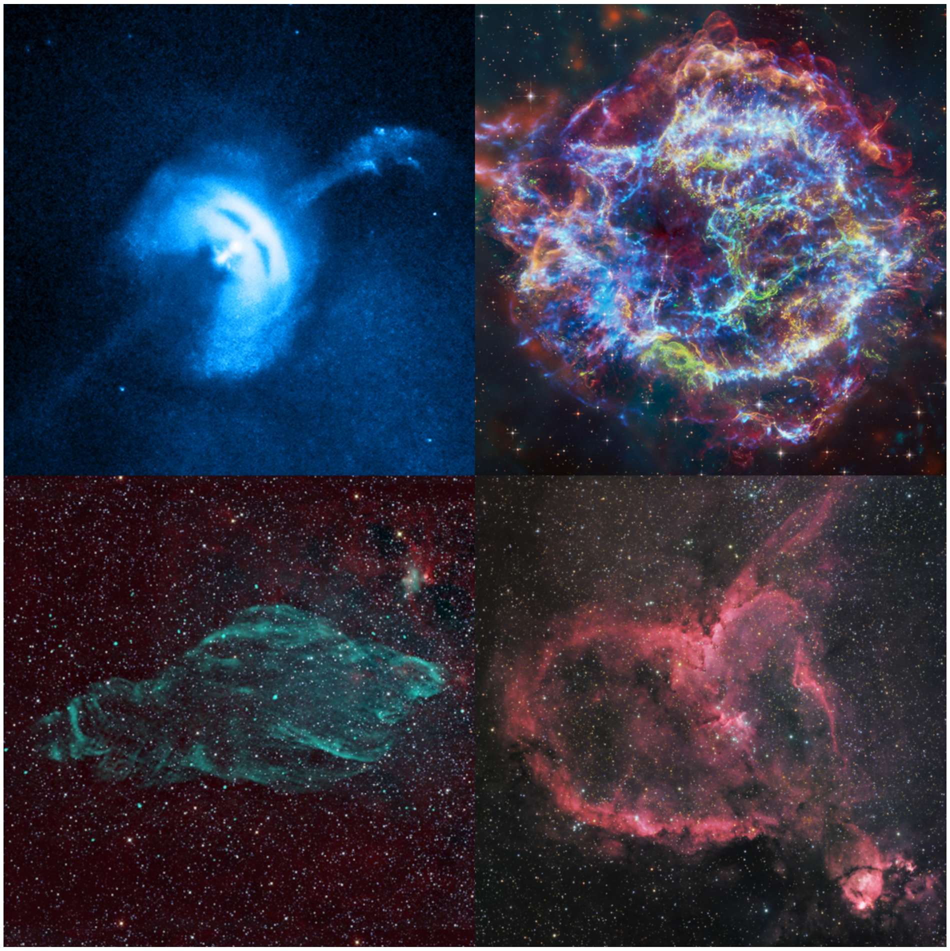

Figure 1.3: Upper left: Vela pulsar with its wind nebula. Credit: NASA/CXC/Univ of Toronto/M.Durant et al., https://chandra.harvard.edu/photo/2013/vela/.
Upper right: Cassiopeia A, an example of SNR. Credit: NASA/CXC/SAO/ESA/STScI/CSA/JPL/CalTech/Milisavljevic et al., https://chandra.harvard.edu/photo/2024/casa/.
Lower left: SS 433, an example of microquasar. Credit: NRAO/AUI/NSF, K. Golap, M. Goss; NASA's Wide Field Survey Explorer (WISE). https://www.nrao.edu/pr/2013/w50/index.shtml.
Lower right: the Heart nebula, an example of star cluster. Credit: John Corban, ESA/ESO/NASA. Software used Photoshop and FITS Liberator. https://www.esa.int/ESA_Multimedia/Images/2013/02/The_Heart_nebula.

Star clusters and superbubbles

Star clusters host dense stellar populations with intense activity, producing powerful winds capable of accelerating particles to PeV energies and forming low-density cavities known as superbubbles. A notable example is the Cygnus Cocoon region, which drew significant attention after LHAASO detected gamma rays above 1 PeV (Cao, F. A. Aharonian, et al., 2021), suggesting that star clusters may act as PeVatrons and emit high-energy gamma rays through hadronic interactions. For older clusters, it is still debated whether the emission originates from unresolved individual sources such as SNRs or PWNe rather than from collective stellar wind activity. In very young clusters, however, the absence of SNRs and PWNe as in M16 and RCW38 (Stoop et al., 2023; Winston et al., 2011) implies that the emission must be produced by cosmic rays accelerated by stellar winds.

Extragalactic gamma-ray sources

Active galactic nuclei (AGNs)

They are distant galaxies with an extremely luminous center powered by a supermassive black hole (SMBH). The flow of matter onto the SMBH generates hot regions in an accretion disk and, together with the spin of the black hole, can eventually drive relativistic jets. According to the unified model proposed by Antonucci (1993), all AGNs share some of the same characteristics and their diversity depends on the viewing angle. In Fig. 1.4 are illustrated the main classes as a function of orientation: blazars (the relativistic jet is aligned with the line of sight), quasars (at intermediate angles relative to the jets), Seyfert galaxies (similar to quasars but with lower overall luminosities) and radio galaxies (near the plane of the accretion disk). To date, the number of VHE-detected AGNs is ~ 90 according to the TeVCat (Wakely and Horan, 2008).[3]

---

[3] `https://tevcat2.tevcat.org`.

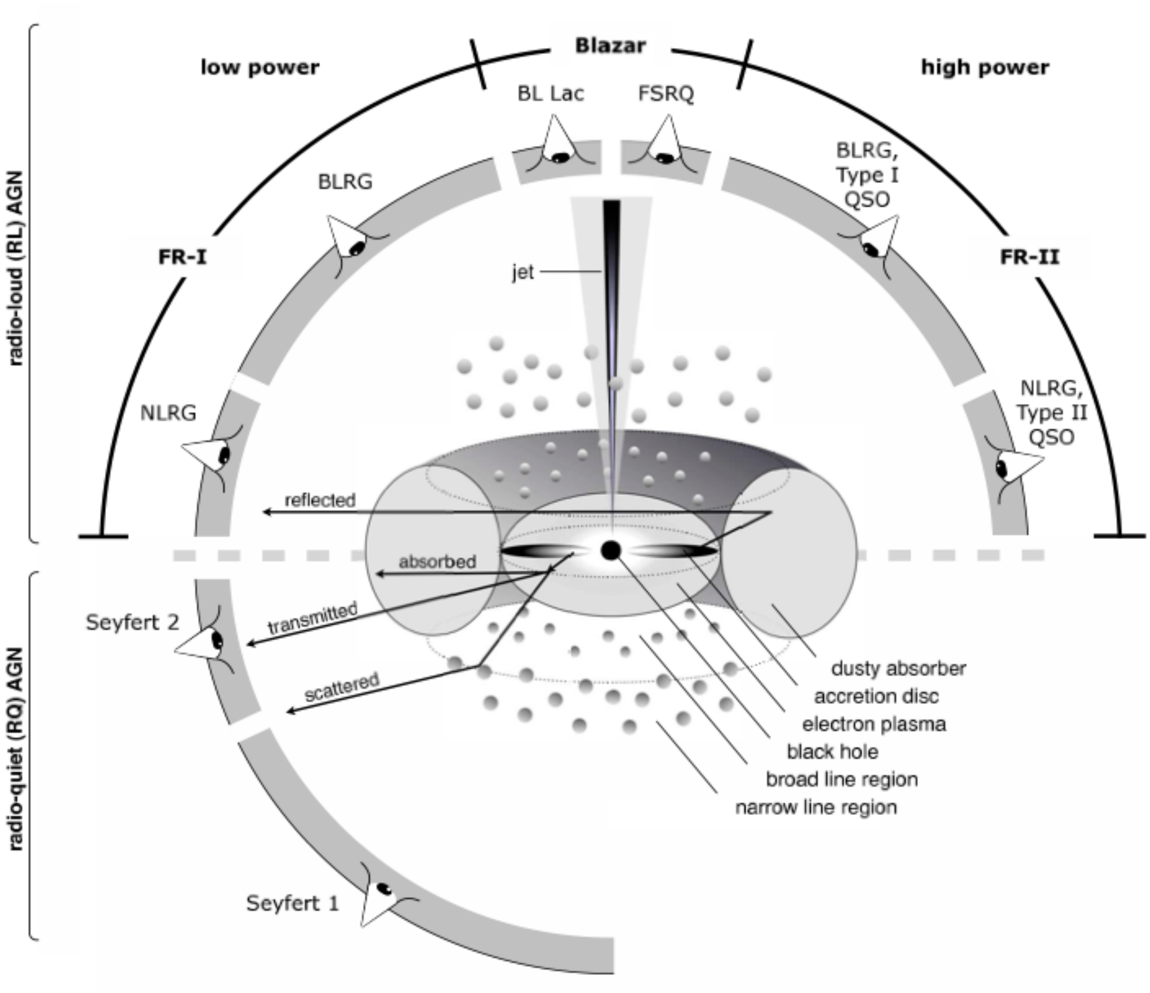

Figure 1.4: Schematic representation of the AGN structure and its classification within the unified model (Antonucci, 1993). The observed type depends on the viewing angle, the presence and strength of jet emission, and the power of the central engine.
Credit: Beckmann and Shrader, 2012.

Gamma-ray bursts (GRBs)

They are brief but extremely energetic explosions. GRB emission occurs in two phases. The first (prompt phase) is the most violent, attributed to internal shocks. Depending on the progenitor, the prompt emission can be short (lasting less than two seconds, typically produced by the merger of compact objects, or kilonovae) or long (associated with extreme core-collapse events). The second phase (afterglow) lasts much longer, radiating across the electromagnetic spectrum. Observing GRBs at VHE remains challenging due to instrumental limitations and is generally feasible only during the afterglow phase. Nonetheless, notable detections have been achieved with current telescopes such as MAGIC (MAGIC Collaboration et al., 2019). As of today, TeVCat lists five VHE-detected GRBs.

Starburst galaxies (SBGs)

They are systems experiencing intense star formation episodes. The elevated rates of supernovae and stellar winds enrich the interstellar medium with dense gas, making the environment efficient at accelerating cosmic rays. Their gamma-ray emission has been confirmed in only two SBGs (Ohm, 2016). Their emission is modeled by both leptonic processes and hadronic processes. Observations above 100 GeV favor the hadronic scenario, though secondary leptonic contributions cannot be excluded (Bose et al., 2022).

1.4 Detection techniques

The detection of high-energy photons in gamma-ray astronomy presents challenges due to the opacity of the Earth's atmosphere at these wavelengths. As a result, direct detection necessitates space-based telescopes. Additionally, gamma rays cannot be refracted or reflected by conventional optical mirrors, requiring different detection schemes based on photon-matter interactions.[4]. However, the low gamma-ray flux and their small collection area restrict their sensitivity at energies above a few tens of GeV, preventing the detection of VHE sources.

In recent years, efforts to improve sensitivity at higher energies have focused on detecting secondary particles produced when gamma rays interact with the Earth's atmosphere (see Appendix B and C). Several ground-based gamma-ray detectors now use this method, reaching energies up to the PeV range. Among these, Imaging Atmospheric Cherenkov Telescopes (IACTs) stand out. The first Large-Sized Telescope (LST-1), which is central to this work, is an example. LST-1 will be part of the Cherenkov Telescope Array Observatory (CTAO), a new generation of IACTs expected to significantly advance gamma-ray astronomy in the near future due to its improved sensitivity.

---

[4] Primarily Compton scattering and pair production (Rybicki and Lightman, 1979). Compton scattering dominates below 100 MeV, while pair production dominates above 100 MeV. The interaction cross-sections guide the design of gamma-ray telescopes across various energy regimes.

Space-based telescopes are typically sensitive to energies ranging from 100 keV to 100 GeV, in the HE regime. In contrast, ground-based telescopes operate efficiently in the VHE and UHE domains, between 100 GeV and up to 1 PeV, depending on the technique employed (IACTs, water Cherenkov arrays, or scintillator-based detectors; see later). These complementary thresholds define the multi-instrument strategy necessary for complete coverage of the gamma-ray sky.

Space-based telescopes

Compton telescopes

They detect gamma rays through the Compton scattering effect, and operate in the 0.1 - 10 MeV band. They usually employ a two-layer structure (C. Kierans, Takahashi, and Kanbach, 2022): an initial scatterer (often liquid scintillator) followed by an absorber (thick solid scintillators) and anti-coincidence shielding to minimize background from cosmic rays.

The most successful mission of a Compton telescope is the COMPTEL telescope (Schoenfelder et al., 1993), which flew aboard the Compton Gamma-Ray Observatory (CGRO) launched in 1991. COMPTEL was able to observe intense sources like AGNs, GRBs, and the Crab and Vela pulsars. Its notable contribution was the creation of galactic sky maps across multiple energy bands, which helped to track the distribution of some isotopes in the Galaxy, contributing to studies of supernova remnants (Schonfelder, 1995). New initiatives such as e-ASTROGRAM (de Angelis, Tatischeff, et al., 2018), AMEGO (C. A. Kierans, 2021), and COSI (Tomsick and COSI Team, 2024) aim to enhance sensitivity at these energies.

Pair-production telescopes

They detect the electron-positron pairs generated when an incoming gamma ray interacts with the detector, making them sensitive to energies above 10 MeV. They typically consist of the following components (David J. Thompson and Moiseev, 2022): a tracker which basically tracks the $e^- - e^+$ pair produced traveling through a set of metal plates (early detectors employed spark chambers filled with gas ionized by the incident particles, while modern detectors now use silicon-based trackers); an anti-coincidence detector, which identifies charged particles and differentiates them from gamma rays; a calorimeter, which provides energy measurements of particles by absorbing all secondary particles produced by the gamma-ray interaction.

The first pair-production telescopes were developed in the 1960s and 1970s, with notable examples being OSO-3 (W. L. Kraushaar, G. W. Clark, G. P. Garmire, et al., 1972) and COS-B (Bennett, 1990). In the 1990s, the EGRET telescope aboard the CGRO marked a significant contribution to gamma-ray astronomy, detecting numerous sources (Hartman et al., 1999) and greatly enhancing our understanding of high-energy phenomena in the Universe.

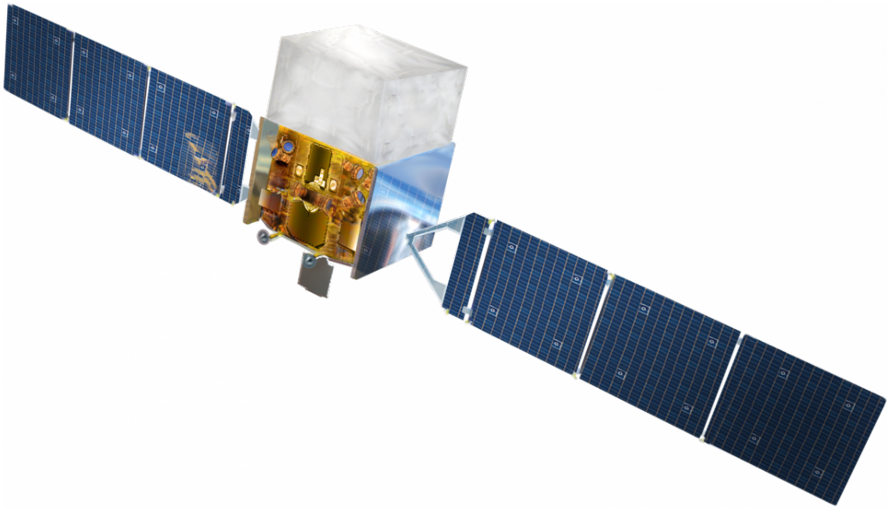

Figure 1.5: An image of the *Fermi* satellite. Credit: NASA, `https://science.nasa.gov/toolkits/spacecraft-icons`.

One of the most renowned pair-production telescopes is the *Fermi* Large Area Telescope (*Fermi*-LAT; Cameron and Fermi LAT Collaboration, 2009), aboard the NASA Fermi Gamma-ray Space Telescope (Fig. 1.5). Launched in 2008, it continues to operate today. Its primary function is as a monitoring system, benefiting from a large field of view. It produces a full gamma-ray sky image every 96 minutes across an energy range of 20 MeV to 300 GeV. It is also equipped with the Gamma-Ray Burst Monitor (GBM), which detects GRBs in the energy range of 8 keV to 30 MeV. Its launch marked a milestone in gamma-ray astronomy, significantly increasing sensitivity by over 30 times compared to its predecessor. Since *Fermi*-LAT began collecting data, the number of known gamma-ray sources has expanded considerably (Ballet et al., 2023). Notably, the study of gamma-ray pulsars has been one of the major achievements of *Fermi*-LAT, resulting in the discovery of nearly 300 new pulsars.

Ground-based telescopes

The limited effective area of space-based telescopes, coupled with the weak fluxes at VHE, restricts their ability to explore the VHE sky. To overcome this limitation, researchers in the 1960s proposed utilizing the Earth's atmosphere as a detector: when a gamma ray enters the atmosphere, it interacts with atmospheric nuclei and rapidly initiates a cascade of particles and electromagnetic radiation, known as an Extensive Air Shower (EAS; see Appendix C), which can be detected from the ground. By using the atmosphere as a calorimeter and deploying detectors over large areas, the effective area increases significantly, enabling the detection of higher energy gamma rays. To study the EAS and infer the properties of the primary particle, ground-based detectors must measure the energy and distribution of the particles forming the shower. This can be done using two main approaches: detecting secondary charged particles or detecting light from shower development.

Detecting secondary charged particles

Detectors placed at high altitudes can capture the secondary particles generated in the shower. This method has a high energy threshold (~ 1 TeV) since weaker showers do not reach the ground. The shower profile is generally obtained by multiple detectors spread over a large area. Two specific techniques used are:

- **Water Cherenkov technique**: uses water tanks where secondary particles generate Cherenkov light as they move through the water. The Milagro experiment (Abdo, B. Allen, et al., 2007), operational from 2000 to 2008, was the first to employ this technique. Following the success of Milagro, the High-Altitude Water Cherenkov Observatory (HAWC) was built (Abeysekara, Albert, Alfaro, Alvarez, Álvarez, Araya, et al., 2023) and has been operating since 2015. The next-generation Cherenkov detector, the Southern Wide-field Gamma-ray Observatory (SWGO), will feature double-layered water tanks to enhance the collection area and sensitivity compared to HAWC (Huentemeyer et al., 2019).

- **EAS Array Technique**: solid-state or scintillator detectors are used to directly detect charged particles. Notable examples include the Tibet ASγ experiment (Amenomori, Bai, et al., 1991) and the ARGO-YBJ experiment (Bernardini and ARGO-YBJ Collaboration, 2008).

The success of these techniques led to the idea of combining water tanks and scintillator detectors in large observatories. The Large High-Altitude Air Shower Observatory (LHAASO) utilizes both detector types to improve sensitivity. Since becoming fully operational in 2021, LHAASO has provided valuable results, detecting numerous gamma-ray sources above 100 TeV which are good PeVatron candidates (Cao, F. Aharonian, An, Axikegu, et al., 2024).

Detecting light from shower development

This approach involves detecting the Cherenkov light (see Appendix B) produced during the shower developed in the atmosphere. Imaging Atmospheric Cherenkov Telescopes (IACTs) follow this technique. These telescopes capture the distribution of Cherenkov light emitted during the development of an atmospheric shower, creating a spatial image that can be used to infer the properties of the primary particle. After accounting for the cosmic-ray background, IACTs can achieve an energy threshold as low as tens of GeV.

A detailed description of this method implemented by current facilities such as MAGIC, VERITAS, and H.E.S.S., including LST-1 of CTAO, will be provided in Chapter 3. This is particularly relevant in this work, given the use of LST-1 data.

1.5 Multiwavelength connections

Gamma-ray observations alone often provide limited insight into the physical conditions of the emitting region. Multiwavelength data, ranging from radio to X-rays, are important as well to constrain the particle population, magnetic fields, and radiation fields involved (Rybicki and Lightman, 1979). In particular, radio and X-ray synchrotron emission trace the lower-energy tail of the electron distribution, complementing gamma-ray IC signatures. Radio emissions, especially the molecular spectral line ^{12}CO, are also important to estimate the target gas density for hadronic interactions. Infrared and optical data help estimate the target photon fields for IC scattering and probe stellar environments in Galactic sources. Moreover, X-rays can also reveal thermal components or shock fronts in SNRs and PWNe, linking morphology with gamma-ray structures.

Combined spectral energy distributions (SEDs) and correlated light curves enable a more robust discrimination between leptonic and hadronic emission models, especially in sources like microquasars, star clusters, SNRs, and AGNs.

1.6 Multimessenger connections

Gravitational waves (GWs) and neutrinos provide complementary information to gamma-ray observations in the context of multimessenger astrophysics. Binary mergers involving neutron stars (NS-NS or NS-BH) can emit both GWs and gamma rays, often detected as short GRBs. The joint observation of events such as GW170817 (Abbott et al., 2017) has allowed constraints on the nature of the progenitors and offered new tests of fundamental physics, including the speed of gravity and the origin of heavy elements. High-energy neutrinos, on the other hand, are uniquely produced in hadronic interactions, making them probes of non-leptonic processes. The spatial and temporal correlation between neutrino detections and gamma-ray sources, most notably the case of TXS 0506+056 observed by IceCube and MAGIC (IceCube Collaboration et al., 2018, Ansoldi, Antonelli, Arcaro, et al., 2018), provides strong evidence for hadronic acceleration in AGNs and other powerful cosmic accelerators.

2. Gamma-ray pulsars

A pulsar is a neutron star, the compact remnant left after the gravitational collapse of a massive star with initial mass between about 8 $M_\odot$ and 25 $M_\odot$ (Carroll and Ostlie, 2017). These objects, typically around 1.4 $M_\odot$ in mass and with a radius not exceeding ~ 30 km, are among the densest in the Universe: matter is so compressed that electrons and protons combine to form neutrons, giving rise to extremely intense gravitational and magnetic fields.

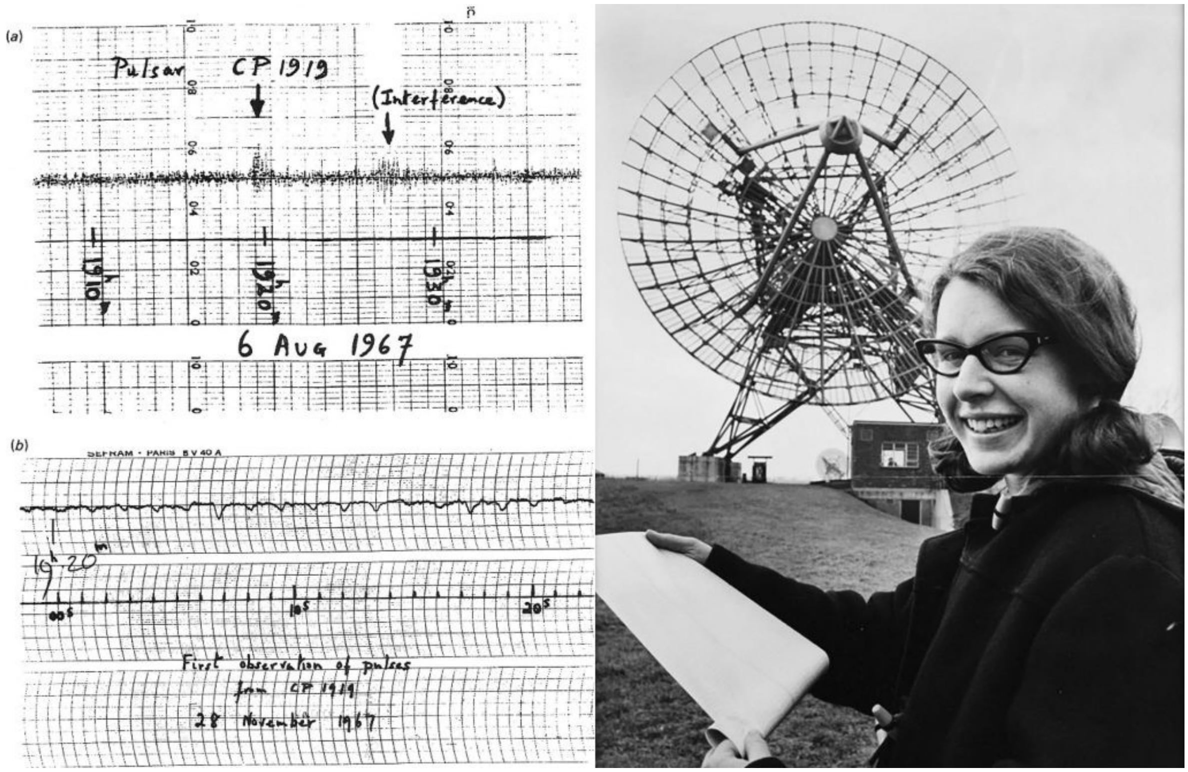

Figure 2.1: Jocelyn Bell at the Mullard Radio Astronomy Observatory and the notes in which she realized she had observed for the first time in history a signal from a pulsar.
Credit: `edu.inaf`.

The existence of neutron stars was first theoretically predicted by Baade and Zwicky (1934) and later modeled by Oppenheimer and Volkoff (1939), while their observational confirmation came with the discovery of pulsars by Bell and Hewish (1967) (see Fig. 2.1). Pulsars are among the most significant sources of gamma-ray astronomy, as discussed in Section 1.3. They are rotating neutron stars that emit beams of radiation across the electromagnetic spectrum. When these beams reach the Earth, they are detected as periodic signals. Their rapid rotation and enormous magnetic and electric fields allow them to accelerate particles to VHE, making them unique laboratories for the study of matter under extreme conditions, relativistic effects, and high-energy radiation processes.

Despite decades of research, the emission mechanisms of pulsars remain only partially understood. In recent years, the discovery of a large population of gamma-ray pulsars with the *Fermi*-LAT satellite has spurred the development of new theoretical models. Furthermore, the detection of pulsars at energies above 20 GeV with IACTs (see Chapter 3), including Crab and Vela, observed up to TeV, has further challenged existing scenarios and added complexity to the picture.

In this Chapter we will review the main physical properties of pulsars and neutron stars (see Carroll and Ostlie, 2017 and references therein for further details), with particular emphasis on the VHE gamma-ray domain. The different models proposed to explain their emission will also be presented.

2.1 Pulsars and neutron stars

The stellar evolution of a massive star ($M > 8\ \mathrm{M}_{\odot}$) occurs through a series of nuclear burning stages of different elements in the core. In the final steps of their life, the core is primarily composed of iron. Iron has the highest binding energy per nucleon, making it impossible to initiate subsequent nuclear reactions. At this point, the star begins to collapse upon itself, as there is no longer a nuclear reaction capable of balancing the force of gravity, and as a result, the temperature in the core rises. When the temperature reaches around $7 \times 10^9 K$, the process of photodisintegration of iron begins, leading to the rapid consumption of iron in the core. Because of the high pressure, not only electrons but also protons and neutrons start to be degenerate. In the very dense environment of a collapsing core, the Fermi energy of degenerate particles is large enough that the electron capture becomes possible:

$$p + e^- \to n + \nu_e \tag{2.1}$$

Thus, we are left with a neutron-rich core. In about 1 second, the star releases a large amount of energy, also due to the emission of neutrinos, which carry away energy and angular momentum, accelerating the collapse. The material collapsing onto the dense core bounces and triggers a shock explosion, known as a type II supernova explosion. The remaining core composed mostly of neutrons is called neutron stars. It usually has a mass of 1.4 $M_\odot$ within a radius of ~10 km (Carroll and Ostlie, 2017), and it is stable because the degeneracy pressure force balances the force of gravity. If the mass of the remaining core exceeds ~3 $M_\odot$, known as the Tolman–Oppenheimer–Volkoff (TOV) limit, the collapse forces would overcome the pressure forces, resulting in a black hole. It is also believed that during the collapse, most of the angular momentum is conserved, giving the neutron star an extremely high rotation rate.

Neutron stars emit beams of radiation across the entire electromagnetic spectrum, from radio to gamma rays. If one of these beams intersects our line of sight, we observe a pulsed emission in our data. This is why these types of neutron stars are called pulsars. Their rotation period is very short and stable, so stable that they are also called the cosmic beacons or cosmic clocks of the Universe.

2.1.1 General properties

The formation process of neutron stars and their physical characteristics account for their properties. These objects reveal the extremities of physics through several features:

1. They are highly magnetized: neutron stars exhibit magnetic fields in the range of $(10^{11} - 10^{15} G)$. Such strong fields are a direct outcome of magnetic flux conservation during the stellar collapse. The resulting electromagnetic fields are powerful enough to extract particles from the stellar surface, giving rise to a magnetosphere. Within this magnetosphere, particles can be accelerated to very high energies, making neutron stars ideal environments to investigate matter under extreme electromagnetic conditions.

2. They possess very high densities: their mass is typically equal to 1.4 $M_\odot$, compressed into a sphere with a radius of about 10 km. These values make the neutron star to achieve densities comparable to nuclear matter ($\bar{\rho}_{NS} \approx 5 \times 10^{14} g/cm^3$). Due to this, neutron stars rank among the most compact astrophysical objects, second only to black holes.

3. They rotate very fast: the collapse of the progenitor star preserves its angular momentum after the supernova explosion, resulting in neutron stars with very short angular velocities. Their rotation periods usually range between a few seconds and a few milliseconds.

4. They have an intense surface gravity: the acceleration of gravity on neutron stars can be up to 10^{11} that of Earth.

5. They are sources of gravitational waves: asymmetries in the mass distribution or more likely binary mergers involving neutron stars can produce gravitational wave signals, as confirmed by LIGO and Virgo detections (Abbott et al., 2017).

Inner structure

The inner structure of a neutron star is difficult to study due to the uncertainty in determining its equation of state. Their extreme densities, close to nuclear density, and the properties of the particle plasma make the interior particularly challenging to model. The internal structure of a neutron star is believed to consist of several layers, as shown in Fig. 2.2:

- Atmosphere: this is the outermost layer, where thermal radiation is emitted. It is composed of common elements such as hydrogen, helium, and carbon. Some models also propose the existence of a thin liquid stratum at the base of the atmosphere, resulting from the increased density in the deepest part of it (Potekhin, 2014).

- Outer crust: located just beneath the atmosphere, it is a solid layer consisting of a Coulomb lattice made up of neutron-rich, iron-like nuclei, and a degenerate gas of relativistic electrons.

- Inner crust: this region lies below the outer crust and spans about 1 km in depth. At densities around $\rho \sim 4 \times 10^{17} g/cm^3$, neutrons begin to leave the bound states and evolve free. They act as a superfluid, together with a small number of electrons. In this environment, nuclei experience strong nuclear and electromagnetic interactions that lead to deformations, forming exotic structures known as nuclear pasta.

- Outer core: extending for several kilometres, this layer includes not only neutrons, but also superconducting protons and electrons, which decouple due to the extreme densities. Additionally, a fraction of muons also appear in this region.

- Inner core: this is the deepest part of a neutron star. Its properties are inferred only from theoretical models based on Quantum Chromodynamics under extreme density conditions. It is hypothesized that this exotic core is made of quark matter, although other unknown phase transitions may also exist.

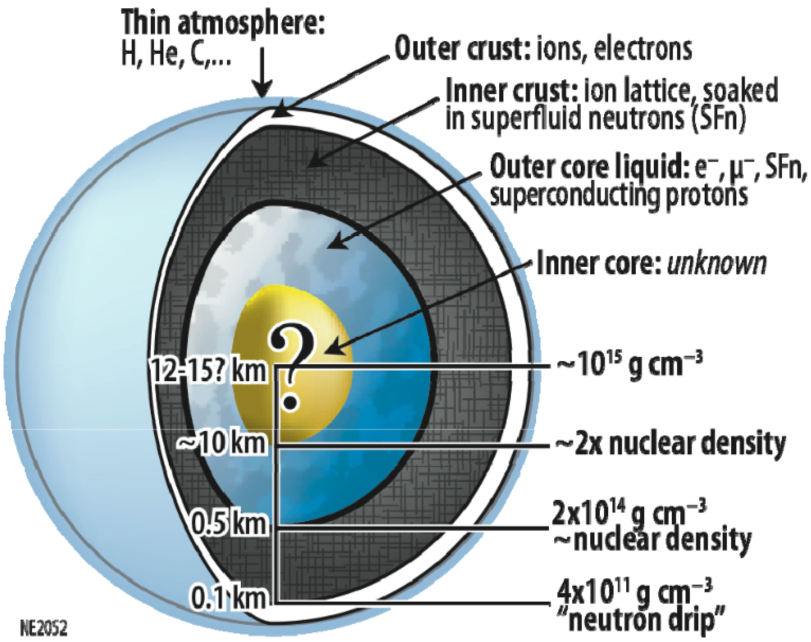

Figure 2.2: Internal structure of a neutron star and its main characteristics.
Credit: Gendreau, Arzoumanian, and Okajima, 2012.

Rotational power and magnetic field

Pulsars slow down in time because they lose rotational energy, a process known as spin-down. According to Pacini (1967), pulsar emission is powered by rotational energy losses through magnetic dipole radiation. Additional mechanisms, such as particle winds or gravitational wave emission, can also contribute to extracting energy and angular momentum from the system.

The total spin-down power of a pulsar can be expressed in terms of its moment of inertia I and angular frequency Ω as:

$$-\left(\frac{dE}{dt}\right)_{rot} = -\frac{d}{dt}\left(\frac{1}{2}I\Omega^2\right) = -I\Omega\dot{\Omega} = 4\pi^2 I\frac{\dot{P}}{P^3} \tag{2.2}$$

where $P = 2\pi/\Omega$ and $\dot{P}$ are the period and its first derivative, respectively. Typical rotational power losses calculated from this expression range from $10^{30} erg/s$ to $10^{38} erg/s$. Assuming that this energy loss is due to magnetic dipole radiation $P = 2|\ddot{\vec{m}}|^2/3c^3$ (Larmor's formula), the power emitted can also be written as:

$$-\left(\frac{dE}{dt}\right)_{rot} = -\left(\frac{dE}{dt}\right)_{dip} \rightarrow -I\Omega\dot{\Omega} = \frac{2m^2\Omega^4\sin^2(\alpha)}{3c^3} \tag{2.3}$$

where α is the angle between the rotation and magnetic axes, and m is the modulus of the magnetic moment, directly related to the magnetic field at the surface B: $m = BR^2$. Under the dipole model assumption, one obtains that:

$$\frac{d\Omega}{dt} \sim \Omega^3 \tag{2.4}$$

Observationally, a more general relation is found:

$$\frac{d\Omega}{dt} \sim \Omega^n \tag{2.5}$$

where n is the braking index. Measured values of n typically lie between 1.4 and 2.9, indicating that mechanisms beyond dipole radiation may contribute to the spin-down. If the second derivative of the rotation frequency can be measured, the braking index can be calculated from:

$$n = \frac{\Omega\ddot{\Omega}}{\dot{\Omega}} = 2 - \frac{P\ddot{P}}{\dot{P}} \tag{2.6}$$

Rearranging the spin-down power equation (Eq. 2.2), the magnetic moment can be expressed as:

$$m^2 = -\frac{3I\dot{\Omega}c^3}{2\Omega^3\sin^2(\alpha)} \tag{2.7}$$

This relation can be rewritten in terms of the magnetic field and the pulsar radius R:

$$B = \sqrt{\frac{3Ic^3}{2R^6\sin^2(\alpha)}}\sqrt{\frac{\dot{\Omega}}{\Omega^3}} = \sqrt{\frac{3Ic^3}{8\pi^2R^6\sin^2(\alpha)}}\sqrt{P\dot{P}} \tag{2.8}$$

Using the observed values of P and $\dot{P}$, surface magnetic fields can be estimated, typically ranging from $10^9 - 10^{13} G$.

Characteristic age

For a neutron star with a general braking index n, the characteristic age τ can be determined by integrating over its rotational frequency:

$$\frac{d\Omega}{dt} = C\Omega^n \rightarrow \tau = \frac{1}{C}\int_{\Omega_0}^{\Omega}\frac{d\Omega}{\Omega^n} = \frac{1}{C}\frac{1}{1-n}\Omega^{1-n} \tag{2.9}$$

Here, Ω_0 denotes the initial spin frequency. If this initial frequency is sufficiently large, terms involving $1/\Omega_0$ become negligible, allowing a simplified expression for the characteristic age:

$$\tau = \frac{1}{1-n}\frac{\Omega}{\dot{\Omega}} = \frac{1}{1-n}\frac{P}{\dot{P}} \tag{2.10}$$

Using this approximation, typical pulsar ages derived from this fall within the range of $10^3 - 10^6$ years, providing a good estimation of the true age (J. H. Taylor and Manchester, 1977).

Density

The minimum spin frequency of a neutron star is set by the condition that gravitational and centrifugal forces are in equilibrium:

$$F_{grav} = F_{cent} \rightarrow \Omega^2 R = \frac{GM}{R^2} \tag{2.11}$$

This relation allows one to derive a lower bound on the stellar density based on the rotational frequency of the pulsar:

$$\rho > \frac{3\Omega^2}{4\pi G} = \frac{3\pi}{P^2 G} \tag{2.12}$$

For pulsars with spin periods in the millisecond range, the resulting densities exceed $10^{10} g \cdot cm^{-3}$. These huge densities are responsible for the peculiar internal structure of the star.

2.1.2 Pulsar population and classification

According to Smith et al. (2023), a total of 3436 pulsars have been discovered. Their distribution shows a strong concentration along the Galactic plane and toward the Galactic center, as illustrated in Fig. 2.3. The map refers to pulsars detected in the radio band, which represent the majority of the known population.

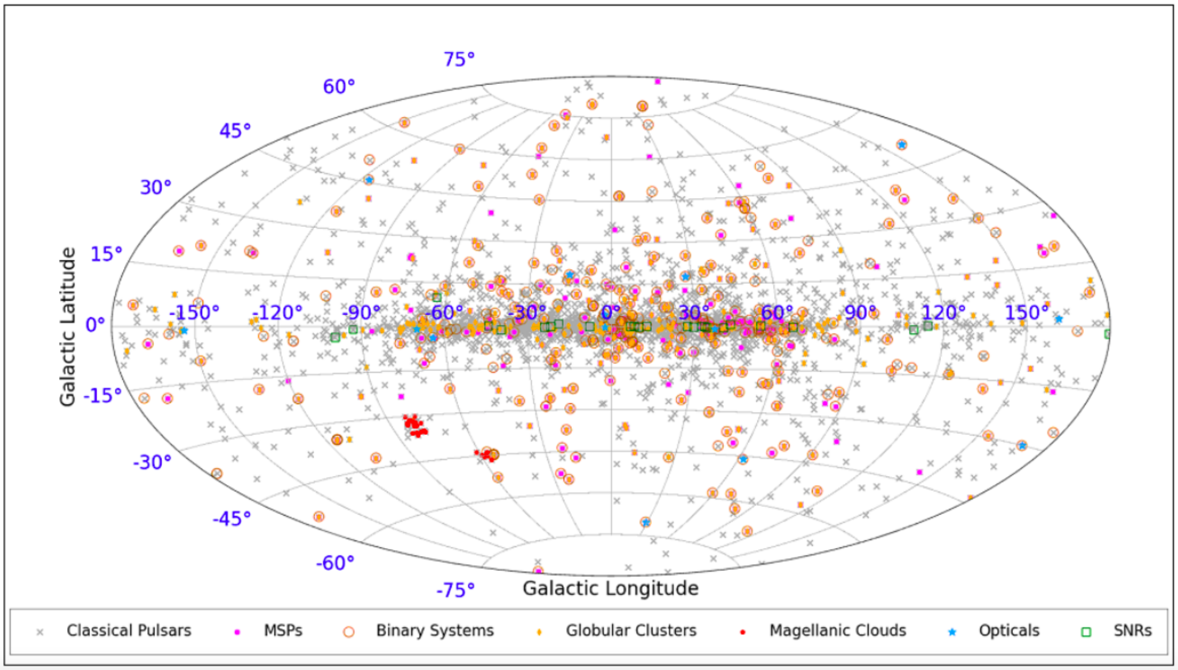

Figure 2.3: A map showing radio and optical pulsars. They are primarily distributed along the Galactic plane, though several are found at higher Galactic latitudes. The map distinguishes between different sub-populations of pulsars and includes those located in the Magellanic Clouds.
Credit: Rami Mandow,
`https://www.spaceaustralia.com/feature/milky-ways-cosmic-clocks-pulsars`.

The physical characteristics of these pulsars (see Section 2.1.1), such as magnetic field strength, rotation period, and age, vary widely. Nonetheless, the overall population can be grouped based on specific measurable quantities. A tool for classification is the $P-\dot{P}$ diagram, which shows the rotation period as a function of the first derivative of the rotation period with respect to time. It indicates how fast the rotation is slowing down. The most up-to-date diagram, which includes gamma-ray pulsars listed in the Third *Fermi*-LAT Catalog (Smith et al., 2023), is presented in Fig. 2.4. Lines of constant magnetic field, age, and spin-down power are shown as dashed lines, reflecting the relationships among these properties.

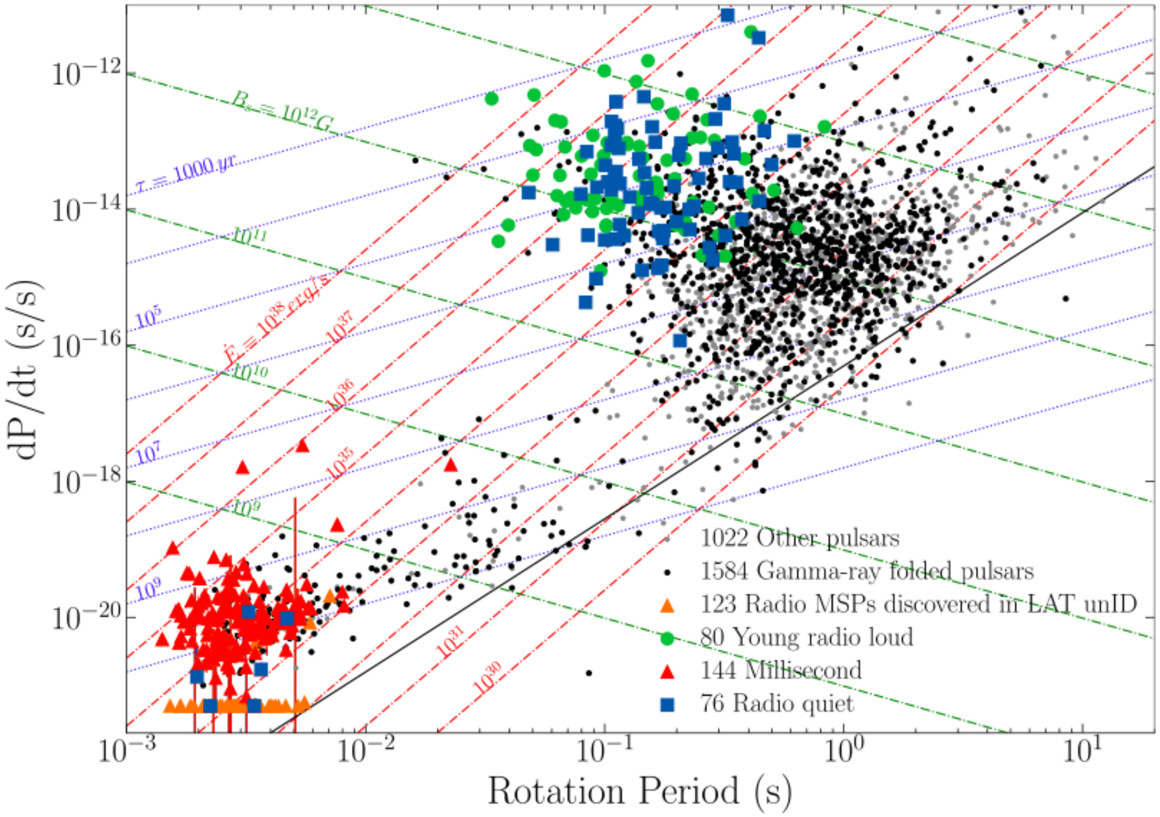

Figure 2.4: $P - \dot{P}$ diagram showing the current population of pulsars, including those detected by *Fermi*-LAT. Different pulsar classes are color-coded according to the legend. Dashed lines indicate constant magnetic field strength, characteristic age, and spin-down power, highlighting the physical relationships between these parameters.
Credit: Smith et al., 2023.

Canonical pulsars and millisecond pulsars (MSPs)

From Fig. 2.4, two distinct clusters can be observed. Pulsars with relatively short periods (∼ms) are typically younger and characterized by high spin-down power and strong magnetic fields. These objects, known as canonical or non-recycled pulsars, occupy the upper-right region of the $P - \dot{P}$ diagram. Among them, those emitting gamma rays are located toward the left edge of the cluster, indicating that they possess high magnetic fields and high spin-down power.

In contrast, the lower-left region of the $P - \dot{P}$ diagram hosts a separate group of gamma-ray pulsars: the millisecond pulsars (MSPs), or recycled pulsars. MSPs are older and rotate much faster, having been spun up during accretion phases from a companion star. These systems often appear as low-mass X-ray binaries (LMXBs) due to their strong X-ray emission. The increase in spin rate occurs through angular momentum transfer, facilitated by their weak magnetic fields. Compared to canonical pulsars, MSPs are aged neutron stars with significantly weaker magnetic fields.

Initially, it was thought that MSPs could not efficiently produce gamma rays due to the lack of pair production in their magnetospheres (see later). However, *Fermi*-LAT revealed a large population of such emitters (about 120 sources; Smith et al., 2023), demonstrating that MSPs are common sources of gamma rays. Their energy efficiency often appears higher than that of young pulsars, likely because of differences in magnetospheric geometry and particle acceleration processes (Grenier and A. K. Harding, 2015).

Radio-loud and radio-quiet pulsars

Gamma-ray pulsars are also classified by their radio properties:

- Radio-loud pulsars: they emit detectable radio waves. Their gamma-ray signal is usually identified by folding the data with known radio ephemeris (see Section 4.2.3).
- Radio-quiet (or radio-faint) pulsars: they show no radio pulsations and are discovered through blind gamma-ray searches. Before *Fermi*-LAT, only one such object, Geminga, was known. After Fermi's launch in 2008, many radio-quiet pulsars were detected.

Radio-loud pulsars generally have shorter periods than radio-quiet ones, though both groups exhibit similar magnetic fields. The absence of radio emission in some cases might be due to a narrow radio beam in slow pulsars combined with an unfavorable viewing geometry (Marelli et al., 2015).

2.1.3 Phaseograms

The physical characteristics of pulsars are determined by their spin period and its time derivatives (P, $\dot{P}$ and $\ddot{P}$). The phaseogram, or pulse profile, or light curve, represents the variation in emission intensity over a rotation phase and depends on the magnetospheric geometry and the observer's line of sight. In most pulsars, two distinct gamma-ray peaks are observed per rotation. This double-peaked structure can be explained by a conical emission beam intersecting the observer's view twice per rotation. In other cases, a single broad peak is detected, resulting from a particular viewing geometry. Peak intensities within a phaseogram may differ, likely due to relativistic effects. An example is shown in Fig. 2.5, which illustrates the dependence of the pulse profile on viewing angle and emission geometry.

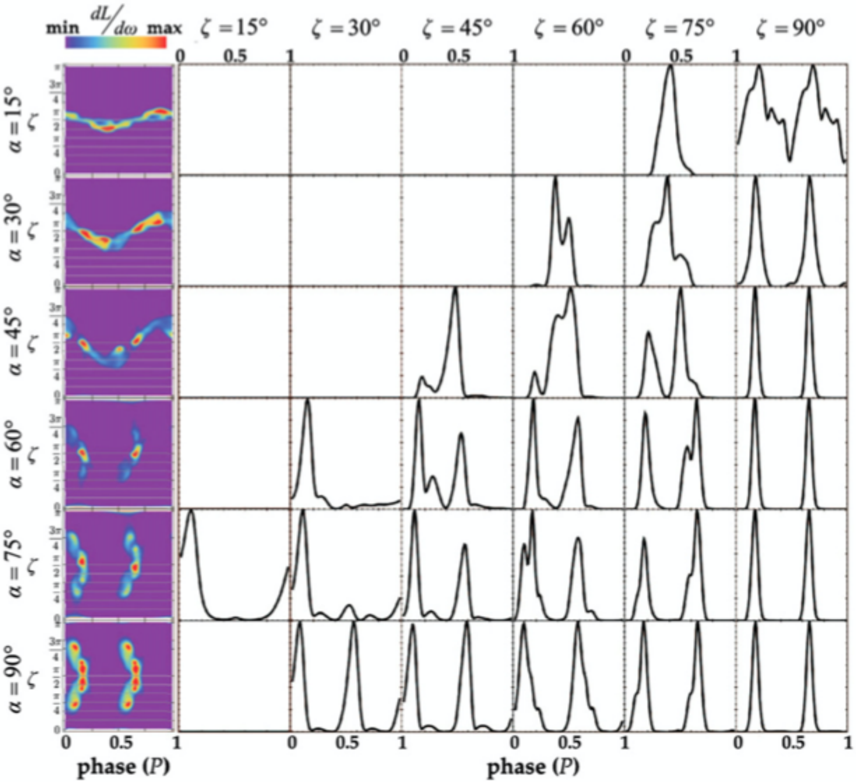

Figure 2.5: Simulated gamma-ray phaseograms (emission intensity vs rotational phase) of the same pulsar for different magnetic inclination angles and observer viewing angles.
Credit: Grenier and A. K. Harding, 2015.

Pulsars typically exhibit stable rotation, characterized by a gradual spin-down rate. However, some of them experience sudden rotational irregularities, known as glitches, which cause a temporary spin-up. These events are thought to originate from internal processes such as neutron star crustal fractures ("starquakes"), consistent with the observed prevalence of glitches in young neutron stars and their absence in millisecond pulsars. Additional sources of timing noise include free precession, orbital companions, and small temporal variations induced by external effects such as gravitational waves, timing reference errors, or inaccuracies in Solar System ephemeris. Disentangling these contributions is non-trivial, yet essential for accurate pulsar timing models.

In this context, precise pulsar ephemeris are essential for gamma-ray analysis: they provide the phase connection needed to fold gamma-ray photons coherently over long time spans (see Section 4.2.3).

2.1.4 Magnetospheres

According to the Goldreich–Julian (GJ) model, the magnetosphere of a pulsar can be divided into distinct regions. Fig. 2.6 provides a schematic representation of them.

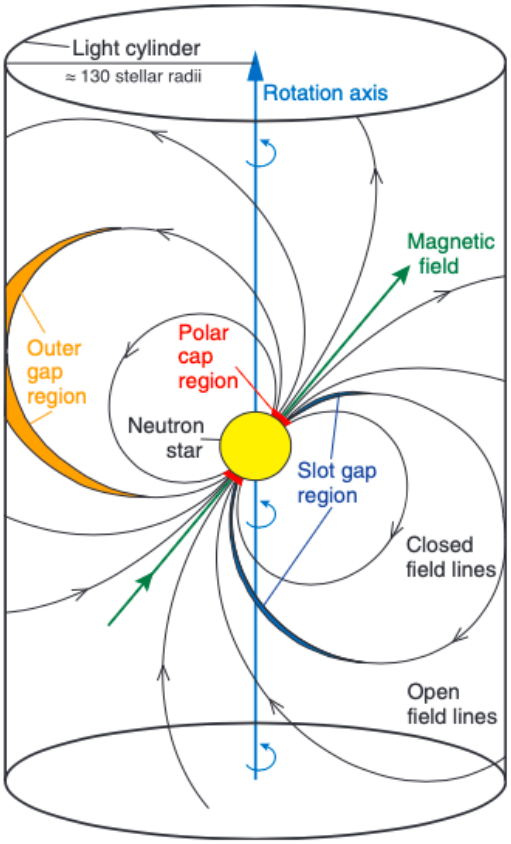

Figure 2.6: Schematic view of a pulsar magnetosphere. The light cylinder separates the closed-field region, co-rotating with the star, from the open-field region where particles escape. The figure also illustrates the main gamma-ray emission regions: polar cap, slot gap, and outer gap.
Credit: Aliu et al., 2008.

- Light cylinder (LC): it is the cylindrical surface where the co-rotation velocity would reach the speed of light:

$$R_{LC} = \frac{c}{\Omega} \tag{2.13}$$

  The light cylinder separates the magnetosphere into two main areas: a closed region and an open one. Inside the LC, magnetic field lines are closed and rotate along with the star. Beyond the LC, field lines are open and particles can escape the system.

- Closed magnetosphere or near zone: it is located within the LC and contains closed magnetic lines that rotate with the pulsar. In this area, the magnetic field lacks a toroidal component and can be described with the dipole approximation. However, as one approaches the LC, this approximation becomes less accurate.

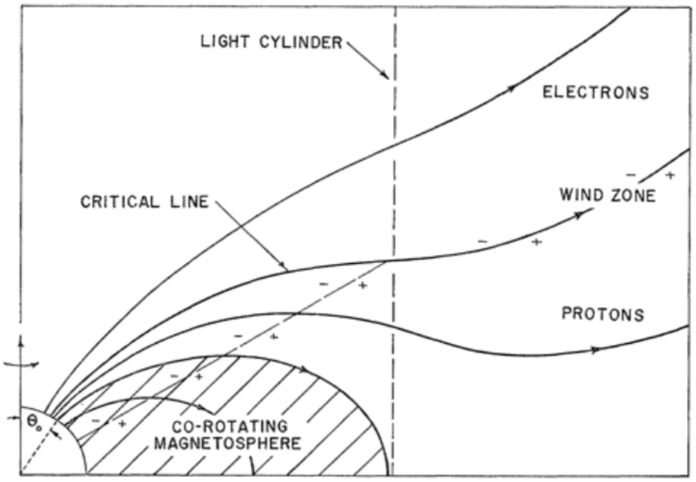

Figure 2.7: Schematic representation of the critical field line in pulsar magnetosphere. The critical line separates regions dominated by opposite charges.
Credit: Goldreich and Julian, 1969.

- Open magnetosphere or wind zone (see Fig. 2.7 and 2.8): beyond the light cylinder lies the region of open magnetic field lines, allowing charged particles to escape. Near the LC, the magnetic field develops a toroidal component, causing the field lines to bend and twist through space.

- Critical field line: it is a line which separates areas dominated by opposite charges and is at the same electric potential as the interstellar medium (ISM). It corresponds to the critical angle θ_c, where for $\theta < \theta_c$ electrons stream outward, while for $\theta > \theta_c$ positrons do (see Fig. 2.7).
- Current sheet: at the equatorial plane, the magnetic field components show a discontinuity, leading to the formation of a current sheet. The toroidal component of the magnetic field also shows a break near the last closed field lines, creating a separatrix. This structure supports a Y-shaped current configuration, as shown in Fig. 2.8, which channels a significant portion of the current back to the neutron star avoiding a continuous accumulation of charge.

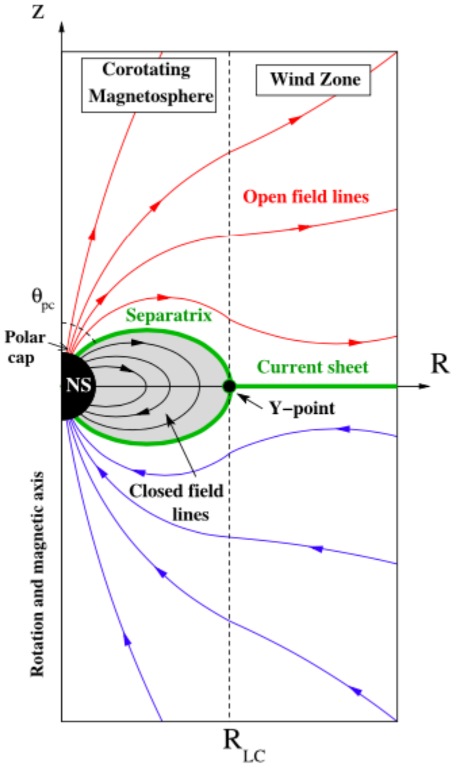

Figure 2.8: Structure of the equatorial current sheet in pulsar magnetosphere. The discontinuity in the magnetic field and the toroidal component near the last closed field lines form a Y-shaped separatrix, channeling part of the current back to the neutron star.
Credit: Cerutti and Beloborodov, 2017.

2.1.5 Emission across the electromagnetic spectrum

Pulsars can emit across the entire electromagnetic spectrum. While nearly all are detected in the radio band, only a fraction have been observed in gamma rays, which are the focus of this thesis. At different wavelengths, their pulse profiles and spectra show energy-dependent variations, as the dominant emission processes and regions vary with energy.

A brief overview of pulsar characteristics in each spectral band is provided below:

- Radio band: radio emission coming from pulsars is not of thermal origin but is believed to result from coherent plasma processes. Although the precise emission mechanism remains uncertain, several models have been proposed. These include instabilities within the magnetosphere leading to radiation, coherence from particle bunches, and mechanisms resembling maser emission (Alexander Philippov, Timokhin, and Spitkovsky, 2020).

- Optical range: optical radiation may arise from a combination of thermal surface emission and non-thermal magnetospheric processes. Only a limited number of pulsars have been observed in the optical band, primarily because of the faintness of their emission and the limited sensitivity of current detectors (Mignani, Rea, et al., 2016). Recent findings suggest a possible common origin for X-ray and optical emission (Illiano et al., 2023). Targeted efforts have been made to identify optical counterparts to gamma-ray pulsars (Mignani, Testa, Marelli, De Luca, Pierbattista, et al., 2016, Mignani, Testa, Marelli, De Luca, Salvetti, et al., 2016).

- X-ray band: the high surface temperatures of young pulsars (on the order of $10^6 K$) can produce thermal X-ray emission, particularly for ages under 10^4 yr. Additionally, particle acceleration near the magnetic poles may heat the surface further, enhancing thermal emission. Non-thermal X-rays from synchrotron radiation are frequently present and may dominate, especially in young or accreting systems. Polarization measurements in X-rays can offer valuable insights into magnetospheric structures (Doroshenko et al., 2022).

- Gamma-ray band: gamma-ray emission from pulsars arises from non-thermal processes in their surroundings. Theoretical models generally invoke synchro-curvature radiation (SCR) or inverse Compton (IC) scattering of low-energy photons (see Appendix A) to account for the observed fluxes. Section 2.3 presents a more detailed discussion about traditional and more advanced theoretical models.

2.2 Pulsars in the gamma-ray regime

Pulsars have long been considered likely sources of gamma-ray emission due to their intense energetic nature. Nevertheless, prior to 2008, detections in this energy band remained limited, with only a handful of confirmed cases, primarily from EGRET (D. J. Thompson, 2008). This scenario changed radically with the launch of the *Fermi* Large Area Telescope (*Fermi*-LAT), which brought a significant leap in sensitivity. Within just a few years, the number of known gamma-ray pulsars expanded dramatically, growing from seven to nearly 300.

2.2.1 High-energy regime

Fermi-LAT has proven to be the most effective instrument for studying gamma-ray pulsars. According to the Third *Fermi*-LAT Catalog of Gamma-ray Pulsars (Smith et al., 2023)), the mission has identified approximately 340 confirmed or candidate gamma-ray pulsars (see Fig. 2.4), whose projected position onto the Milky Way is reported in Fig. 2.9.

Several observational characteristics have been established in the energy range between 30 MeV and 70 GeV:

- A total of 294 pulsars have been officially confirmed. Roughly half belong to the class of young pulsars, while the other half are MSPs. Among the young pulsars, about 50% are also detected in the radio band.

- The phaseograms (see Section 2.1.3) obtained from *Fermi*-LAT data typically exhibit two emission peaks per rotational cycle, with one usually being more prominent. In fewer cases, only a single, broader peak is observed.

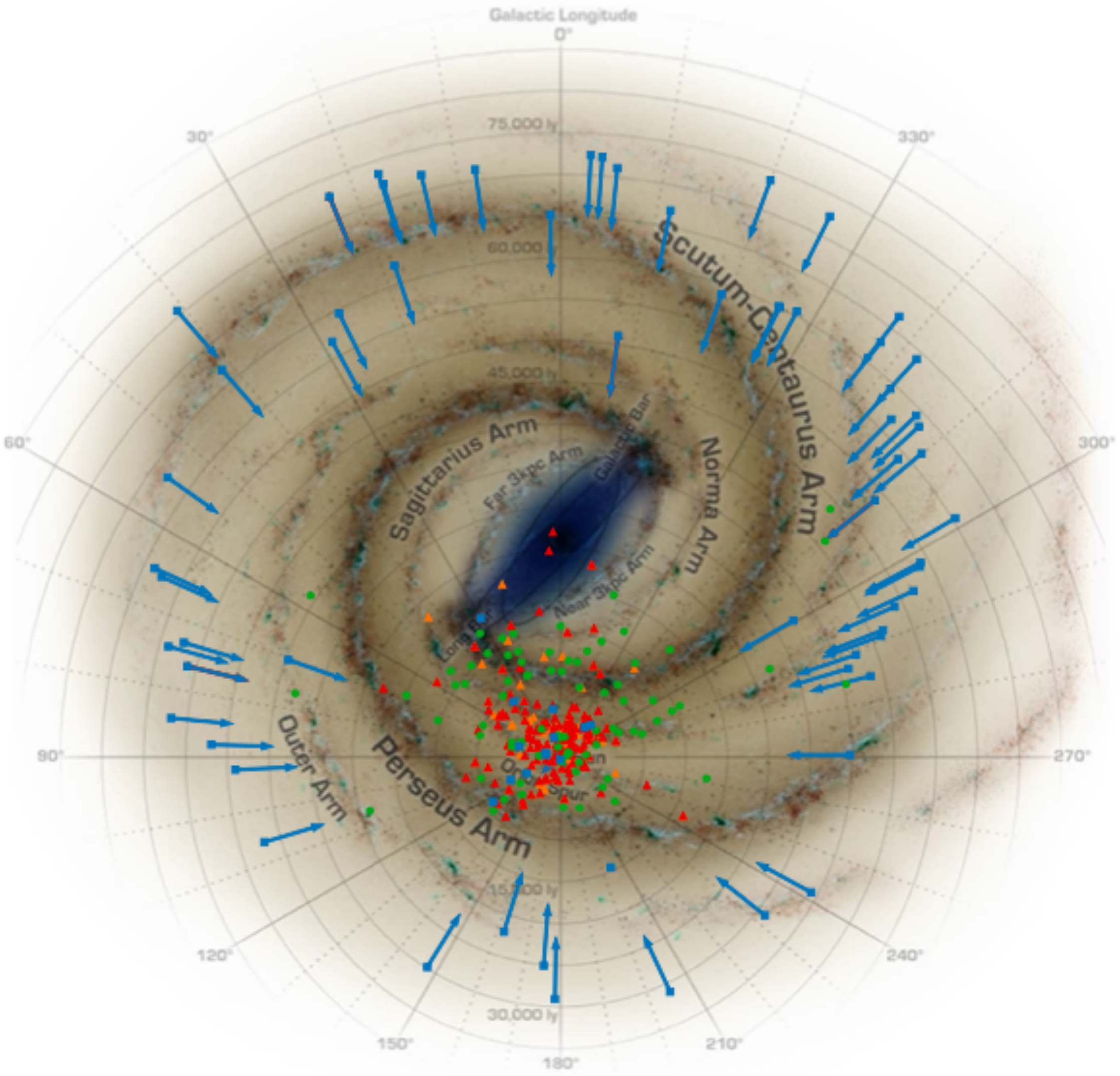

Figure 2.9: Gamma-ray pulsar positions projected onto a Milky Way model.
Credit: Smith et al., 2023.

- Spectral emission follow a power-law distribution with an exponential cutoff. The model used in *Fermi*-LAT analyses is expressed as:

$$\frac{dN}{dE} = N_0 \left(\frac{E}{E_0}\right)^{-\Gamma+d/b} exp\left[\frac{d}{b^2}\left(1-\left(\frac{E}{E_0}\right)^b\right)\right] \tag{2.14}$$

Here, Γ represents the spectral index, and E_0 is the reference energy. The parameters N_0 and d describe the flux and curvature at E_0, respectively. The cutoff parameter b

indicates the nature of the spectral roll-off: super-exponential if $b > 1$, exponential for $b \sim 1$, and sub-exponential when $b < 1$.

- The cutoff energy itself is calculated through the following expression:

$$E_c = E_0 \left(\frac{b^2}{d}\right)^{1/b} \tag{2.15}$$

  Fig. 2.10 shows the distribution of these cutoff energies for the pulsars detected by *Fermi*-LAT. The typical cutoff falls near 1 GeV, with most values between 500 MeV and 5 GeV.

- At energies above 30 GeV, pulsar signals become faint. In cases where detection occurs above this threshold, generally only one of the pulse peaks remains visible; the second peak usually vanishes above 10 GeV. Beyond 50 GeV, the gamma-ray flux of most pulsars drops below the sensitivity limit of current-generation instruments (McCann, 2015).

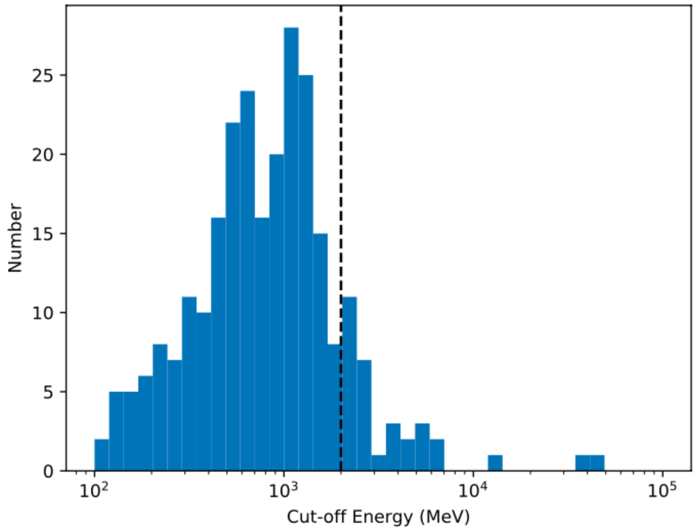

Figure 2.10: Distribution of cutoff energies of gamma-ray pulsars detected by *Fermi*-LAT. Most pulsars show E_c values between 0.5 and 5 GeV, with a typical cutoff near 1 GeV. The dashed vertical line indicates $E_c = 2$ GeV just for reference.
Credit: Pathania, Singh, and Yadav, 2023.

2.2.2 Very-high energy regime

Prior to the launch of *Fermi*-LAT, it was widely assumed that pulsars would not be detected above 10 GeV, based on earlier observations (F. Aharonian, A. G. Akhperjanian, et al., 2007). For this reason, the discovery of pulsars at energies exceeding 50 GeV using IACTs came as a surprise. Nonetheless, observations from MAGIC, VERITAS, and H.E.S.S. demonstrated that some pulsars emit radiation well into the VHE domain (E > 100 GeV). To date, four pulsars have been detected with IACTs (see their galactic position in Fig. 2.11), all of which show strong GeV luminosities in *Fermi*-LAT data. Among these, only two have been observed beyond 1 TeV: Crab and Vela. The pulsars detected so far are:

1. Crab pulsar: this was the first pulsar detected by MAGIC in the 25–100 GeV range (Aliu et al., 2008, Aleksić et al., 2011) and later by VERITAS above 100 GeV (VERITAS Collaboration, 2011). MAGIC subsequently confirmed the emission above 100 GeV (Aleksić et al., 2012). Pulsed TeV emission was later reported for the second peak of the pulsar (Ansoldi et al., 2016), suggesting a single power-law component extending from 50 GeV up to 1.5 TeV. This pulsar is the source studied in this work; further details are provided in Section 2.4.

2. Vela pulsar: H.E.S.S. reported sub-100 GeV emission from this source (H. E. S. S. Collaboration et al., 2018), identifying a spectrum with possible curvature component below 100 GeV, consistent with *Fermi*-LAT results. Although the emission above 100 GeV was weak, subsequent studies claimed pulsed TeV emission, indicating an additional spectral component that extends up to 20 TeV (H. E. S. S. Collaboration, F. Aharonian, et al., 2023). This represents the highest-energy signal observed from any pulsar so far.

3. Geminga pulsar: detected by MAGIC up to 75 GeV (MAGIC Collaboration et al., 2020a), Geminga exhibits a very soft spectrum, making detections at higher energies particularly difficult. Its spectrum hints at a power-law extension similar to that of the Crab pulsar, though no definitive conclusion can be drawn.

4. PSR B1706-44: a possible signal below 100 GeV was reported for this pulsar (Spir-Jacob et al., 2019). Although a conclusive detection remains pending, the reported 4.7σ significance allowed for the extraction of a spectrum below 60 GeV. Due to limited

statistics, it is not possible to confirm the existence of a power-law tail similar to that seen in the Crab pulsar.

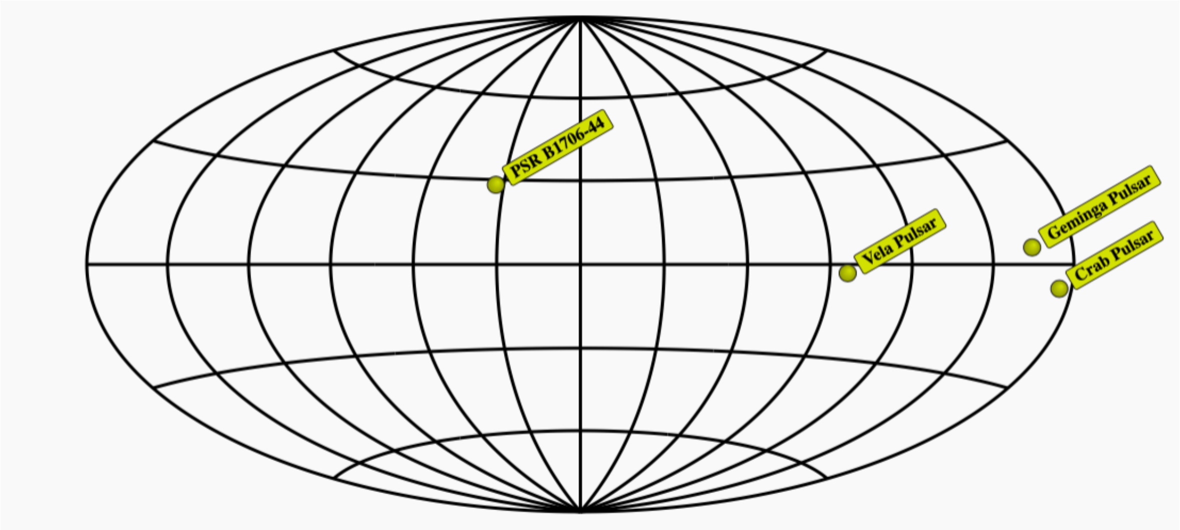

Figure 2.11: Position in galactic coordinate of the four know pulsars detected in the VHE regime. Credit: TeVCat (Wakely and Horan, 2008), `https://tevcat2.tevcat.org`.

These observations are particularly noteworthy because they contradict standard pulsar models (see Section 2.3.1), which predict a sharp spectral cutoff at GeV energies, as observed by *Fermi*-LAT. Current IACT sensitivity, combined with the steep pulsar spectra, limits the number of detections above 100 GeV. In this context, the upcoming Cherenkov Telescope Array Observatory (CTAO), detailed in Chapter 3, will be crucial for exploring pulsars in the VHE regime. This objective underpins the use of LST-1 of CTAO for pulsar studies and serves as the central motivation of this thesis.

2.3 Emission models for gamma-ray pulsars

The structure of a pulsar magnetosphere (see Section 2.1.4) is complex due to the extreme and partly unknown physical conditions in its surroundings. Detailed reviews can be found in (Grenier and A. K. Harding, 2015, Pétri, 2016, A. Philippov and Kramer, 2022). This section provides a summary of the fundamental principles behind pulsar magnetospheres and emission models based on these references, while the radiative processes mentioned are described in more detail in Appendix A.

In the simplest theoretical framework, a pulsar behaves like a magnetic dipole in vacuo with extremely high conductivity. Under this assumption, the magnetic field remains frozen into the star and co-rotates with it. Because of the high conductivity, the induced electric field in the co-rotating frame must vanish, which can only occur under a specific condition:

$$\vec{E} + (\Omega \times \vec{r}) \times \vec{B} = 0 \tag{2.16}$$

If the magnetic axis is inclined with respect to the rotation axis by an angle χ, the dipole magnetic field in spherical coordinates (r, θ, ϕ) can be expressed as:

$$\begin{aligned} E_r^{int} &= \frac{\Omega B R^3}{r^2}\left(\cos\chi \sin^2\theta - \sin\chi \cos\theta \sin\theta \cos\psi\right) \\ E_\theta^{int} &= \frac{\Omega B r^3}{r^2}\left(\cos\chi \sin(2\theta) + 2\sin\chi \sin^2\theta \cos\psi\right) \end{aligned} \tag{2.17}$$

In vacuo, the external electric field must satisfy Laplace's equation, with the corresponding potential given by:

$$\Phi = -\frac{B\Omega R^5}{6r^3}\left(3\cos^2\theta - 1\right) \tag{2.18}$$

When comparing the radial components of the electric field for the case where $\chi = 0$ ($E_r^{ext} - E_r^{int} = -2BR\Omega\cos^2\theta$) one finds that a surface charge must exist to supply the additional field. Close to the stellar surface, the electric field reaches values on the order of $E \sim \Omega RB = 10^{12} - 10^{13} Vm^{-1}$, revealing the extraordinary field strength in this region. These intense electric fields can extract electrons from the stellar surface, which makes a pure vacuum solution impossible. Consequently, a magnetosphere composed of plasma must form around the star.

The Goldreich-Julian model

The first model to depart from a vacuum scenario was proposed by Goldreich and Julian (1969). It assumes that the magnetosphere contains a dense plasma with very high conductivity. To sustain such a plasma, a copious supply of electrons and positrons is needed, generated by pair creation through gamma-ray photons in the polar caps. In this picture, the electric field component parallel to the magnetic field must vanish in the plasma frame:

$$\vec{E} + (\vec{v} \times \vec{B}) = 0 \tag{2.19}$$

This condition is commonly referred to as force-free ($\vec{E} \cdot \vec{B} = 0$). Under force-free conditions, the plasma co-rotates with the neutron star while allowing particle motion along magnetic field lines. The corresponding charge density, known as the Goldreich-Julian density ρ_{GJ}, is given by:

$$\rho_{GJ} = \frac{-2\varepsilon_0 \vec{\Omega} \vec{B}}{1 - (\Omega r \sin\theta)^2} \tag{2.20}$$

From this relation, it becomes evident that the sign of the charge density depends on the product $\vec{\Omega}\vec{B}$. The location where this product is zero defines the so-called null surface. This approximation is only valid inside the co-rotating region, limited by the light cylinder (LC). For a dipolar magnetic field close to the surface, one obtains:

$$\rho_{GJ} = \varepsilon_0 B \frac{R^3}{r^3} (1 - 3\cos^2\theta) \tag{2.21}$$

This leads to the conclusion that, within the GJ framework, the null surface lies at a critical angle $\theta_c = \sqrt{\arccos(1/3)} \approx 54.7$ deg.

Beyond the simplified model

In real pulsars, two main factors break the assumptions mentioned above: the magnetic and rotation axes are generally misaligned, thus solving the equations for an arbitrary inclination is numerically challenging[1]; the ideal magnetohydrodynamic (MHD) assumptions do not fully apply, as infinite conductivity and the absence of non-ideal effects cannot be maintained. Pair creation is necessary where magnetic and electric fields differ, while reconnection events in the current sheet and particle acceleration are also beyond force-free treatments.

---

[1] The time-dependent force-free case for an oblique rotator was numerically solved by Spitkovsky (2006).

To address these limitations, advanced models include both plasma dynamics and radiation processes responsible for the observed radio and gamma-ray emission. Two main approaches dominate current research:

1. Dissipative MHD models: they relax the force-free condition by introducing finite conductivity, enabling effective particle acceleration. While they can reproduce some gamma-ray light curves, they lack self-consistency since the plasma needed for the predicted currents is introduced artificially.
2. Particle-in-cell (PIC) simulations: they attempt a fully self-consistent treatment of plasma and electromagnetic fields by tracking particle motion in a collisionless plasma using N-body techniques. Because simulating each particle is computationally prohibitive, groups of particles with similar dynamics are treated as "macroparticles". These are distributed over a grid where both dynamics and electrodynamics are computed iteratively. Although computationally demanding, PIC simulations, feasible only in recent decades, provide detailed insights, including pair production and acceleration processes (see Philippov, Spitkovsky, and Cerutti, 2015 for more details).

2.3.1 Classical models

Particle acceleration naturally occurs when the force-free condition breaks down. In regions known as gaps, a mismatch between the local charge density and ρ_{GJ} generates a parallel electric field that accelerates particles along magnetic field lines. These particles emit gamma rays through processes such as CR and photon-photon or magnetic pair production. The resulting gamma rays can produce additional electron-positron pairs, triggering electromagnetic cascades within these regions.

Only specific zones enable efficient acceleration to ultra-relativistic energies, yielding a detectable gamma-ray flux. Three classical models have historically described gamma-ray emission from pulsars, differing in the location of the acceleration region: polar cap (PC) model, outer gap (OG) model, and slot gap (SG) model.

Polar cap model

Initially proposed in 1975 by M. A. Ruderman and Sutherland (1975) (review in A. K. Harding, 2013), this model places the gap near the pulsar surface, above the magnetic poles. Here, the electric field is strong enough to extract electrons and accelerate them to Lorentz factors of $10^5 - 10^7$, producing gamma rays via CR (see Appendix A for more details). The intense transverse magnetic field enables magnetic pair production (Erber, 1966) for photons exceeding the threshold $h\nu B_\perp > 4 \cdot 10^{14} eV \cdot T$. Secondary pairs emit further CR photons, driving a cascade, as shown in Fig. 2.12, until the parallel electric field is screened at the pair formation front (PFF). Primary photons are mostly absorbed, leaving only surviving secondary radiation. The resulting spectrum exhibits a sharp cutoff at a few GeV due to the pair-production attenuation coefficient:

$$\frac{dN}{dE} \propto \left(\frac{E}{E_0}\right)^{-\Gamma} \exp\left[-\left(\frac{E}{E_c}\right)\right]^b \qquad \text{with } \; b > 1 \tag{2.22}$$

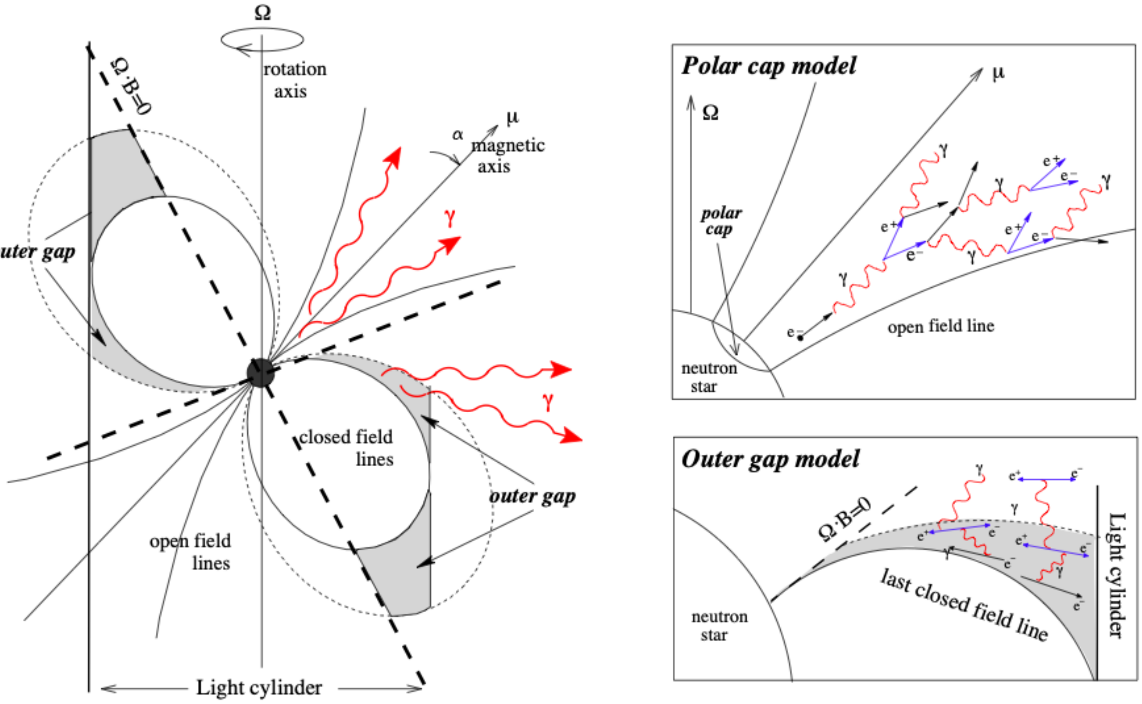

Figure 2.12: Schematic representation of the polar cap (PC) and outer gap (OG) models for gamma-ray pulsar emission. In the PC model, pulsed gamma rays originate from curvature radiation near the neutron star surface, whereas the OG model places the emission in the outer magnetosphere, between the null-charge surface and the light cylinder.
Credit: Lopez et al., 2009.

Although this predicts an abrupt flux drop, *Fermi*-LAT data indicate a softer cutoff ($b < 1$), and the narrow beam predicted by PC models cannot account for the observed pulse widths.

Outer gap model

Here, acceleration occurs in vacuum gaps between the null-charge surface ($\vec{\Omega} \cdot \vec{B}$) and the last closed field lines inside the light cylinder (see Fig. 2.12; Holloway and Pryce, 1981, K. S. Cheng, Ho, and M. Ruderman, 1986, Romani, 1996). Particles accelerate in the outer magnetosphere and radiate via SCR (see Appendix A for details). Magnetic fields are too weak for significant pair creation, though gamma-ray interactions with background photons can yield pairs at a lower rate. This predicts spectra with sub-exponential cutoffs and softer suppression (b<1; Chai, K.-S. Cheng, and Takata, 2016). Three-dimensional OG models reproduce the two-peak profiles seen in gamma-ray pulsars (K. Cheng, M. Ruderman, and L. Zhang, 2000).

Slot gap model

Assuming the parallel electric field vanishes at the last open field lines create a narrow acceleration region along these boundaries (Arons, 1981; A. Harding and Muslimov, 2005). Here, lower electric fields place the PFF at higher altitudes than in PC models. Gamma-ray emission arises from CR and IC (see Appendix A), producing wider pulse profiles than PC predictions. Although SG emission could explain some unidentified EGRET sources, its performance for objects such as the Crab pulsar is less successful compared to OG models (Hirotani, 2008).

Early *Fermi*-LAT results favored models locating acceleration in the outer magnetosphere (OG and SG), yet these fail to reproduce both lightcurve morphology and spectra above 100 GeV. This limitation motivated alternative scenarios involving particle acceleration in the pulsar wind zone.

2.3.2 Current very-high energy models

Recent IACT measurements have revealed gamma-ray emission from the Vela and Crab pulsars extending beyond 100 GeV, deviating from the sharp exponential cutoffs predicted by classical models. If TeV photons originated from CR, unrealistically large curvature radii would be required. Over the last decade, significant efforts, supported by advances in computational modelling, have focused on reproducing these VHE observations. Current approaches explore the modified OG model, the wind zone model, and the current sheet model.

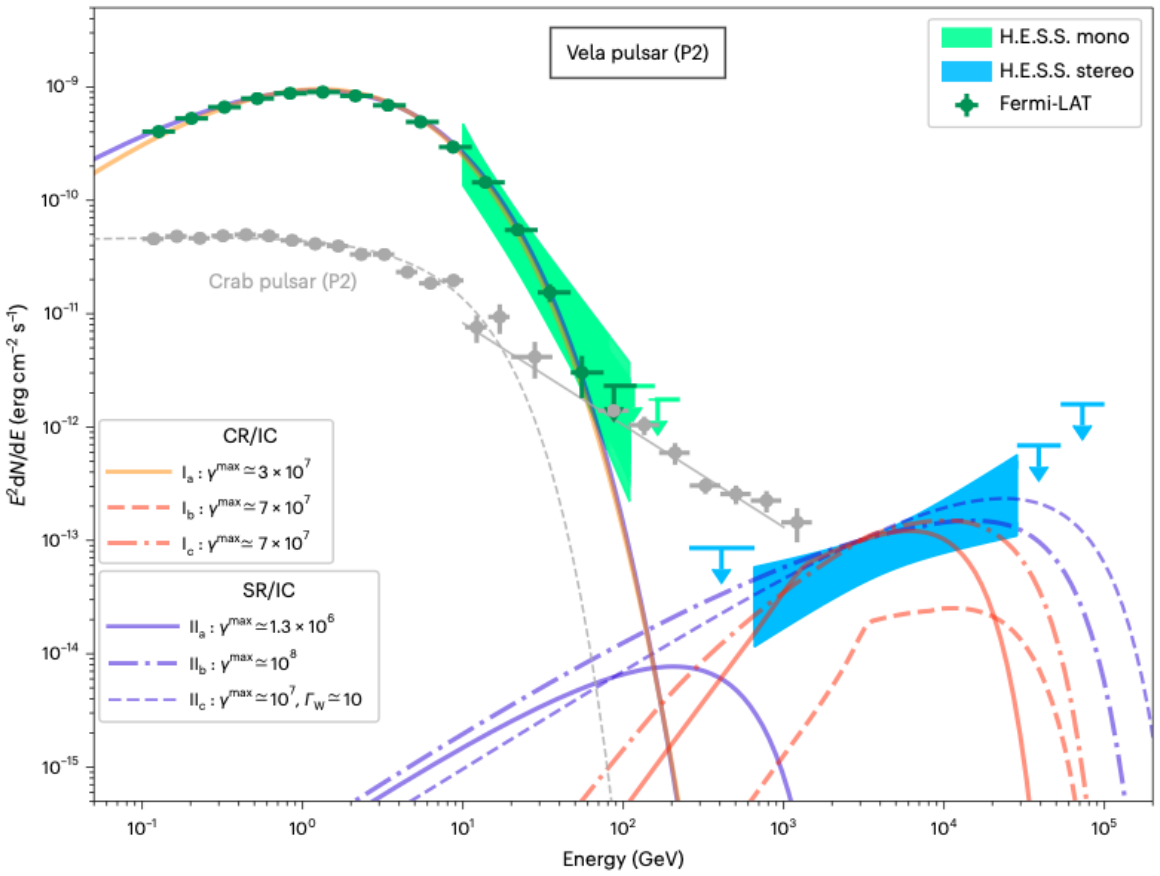

Figure 2.13: Phase-resolved spectral energy distribution (SED) of the Vela pulsar (P2 peak) combining *Fermi*-LAT and H.E.S.S. data (both stereo and mono). The GeV component is consistent with curvature or synchrotron radiation, while the hard extension up to 20 TeV requires inverse-Compton scattering in the Klein-Nishina regime. Model curves illustrate CR/IC and SR/IC scenarios.
Credit: H. E. S. S. Collaboration, F. Aharonian, et al., 2023.

Recent H.E.S.S. observations of Vela have provided the pulsed gamma-ray emission up to 20 TeV (H. E. S. S. Collaboration, F. Aharonian, et al., 2023), well beyond the predictions of conventional theoretical models. Fig. 2.13 shows the phase-resolved spectral energy distribution (SED; see Section 4.1.7) in the second peak, highlighting the presence of two distinct components: a GeV spectrum consistent with CR or SR, and a harder TeV component requiring IC processes in the Klein-Nishina regime. Both CR/IC and SR/IC scenarios are considered, but the measured fluxes challenge standard assumptions on particle energies and acceleration sites, pointing to dissipation regions beyond the light cylinder.

To illustrate the broader theoretical framework, Fig. 2.14 summarizes the main models currently discussed for the VHE pulsed emission, detailed later. The detection of a multi-TeV component in Vela demonstrates that multiple mechanisms may coexist, and that the current sheet plays a central role in explaining the highest-energy photons.

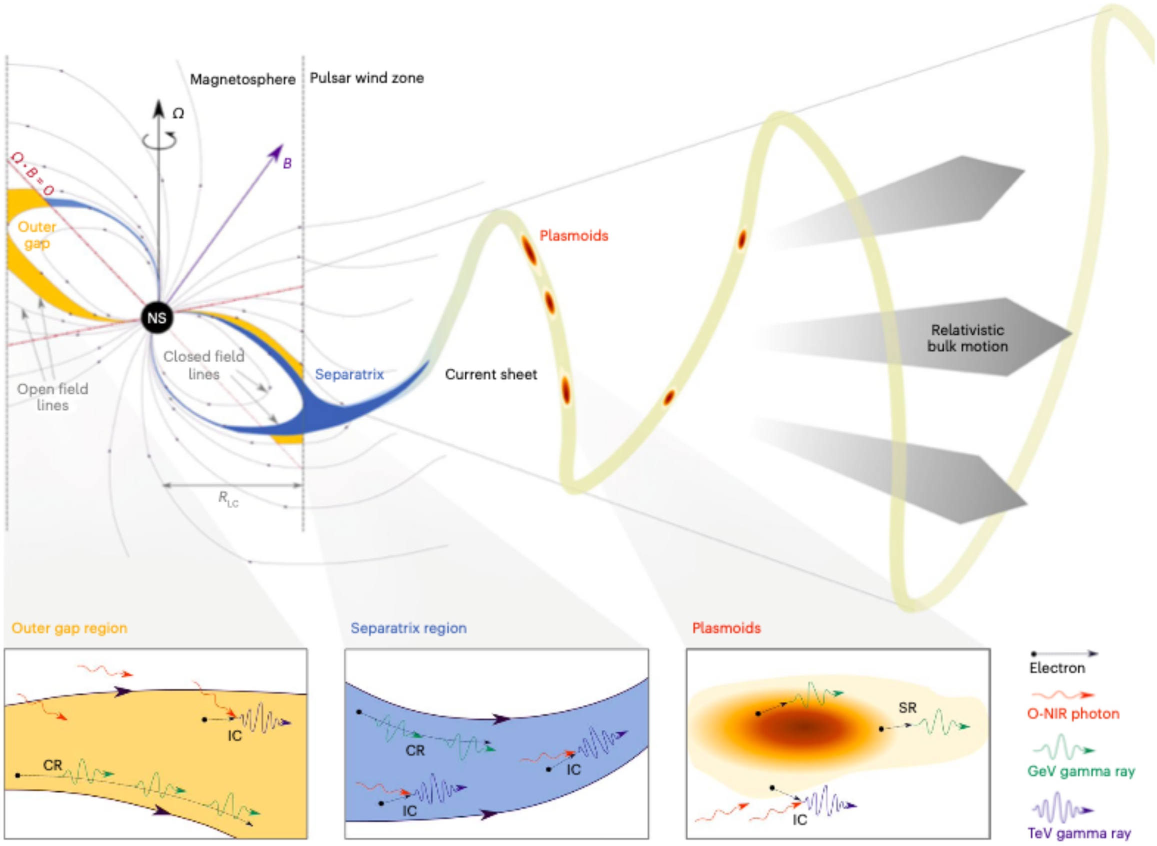

Figure 2.14: Schematic view of the main pulsar VHE emission models. Electrons can be accelerated (1) along magnetic field lines inside the light cylinder (LC), in outer-gap regions or just beyond it (separatrix/current sheet), or (2) through magnetic reconnection in the equatorial current sheet of the stripped wind beyond the LC. GeV photons are mainly produced via curvature or synchrotron radiation, while TeV emission arises from inverse-Compton scattering of optical-IR photons. Spatial scales are not respected: the pulsar radius is ~ 10 km, while the LC radius is ~ 4300 km.
Credit: H. E. S. S. Collaboration, F. Aharonian, et al., 2023.

Modified outer gap model

Revised OG model can produce softer spectral cutoffs, particularly when IC within the outer magnetosphere are included (Hirotani, 2013, Hirotani, 2015). High-energy photons interacting with low-energy photon fields (e.g. infrared radiation) can generate secondary and tertiary pairs at larger distances, potentially emitting TeV photons via IC and synchrotron self-Compton (SSC; see Appendix A; Aleksić et al., 2011). This mechanism was proposed to account for the Crab TeV emission (Ansoldi et al., 2016), although the observed phase-dependent spectral variations between the HE and the VHE bands remain unexplained.

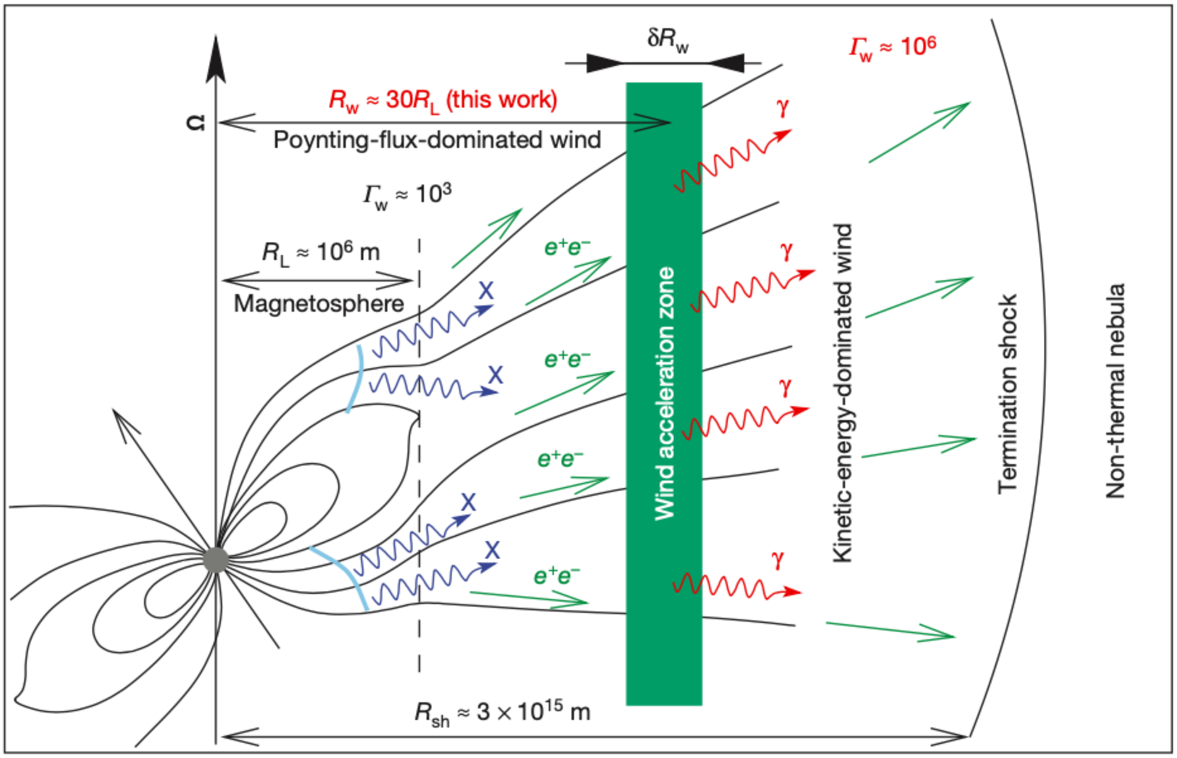

Figure 2.15: Schematic of the pulsar wind model: particle acceleration occurs in a narrow region beyond the light cylinder, where the Poynting-dominated outflow converts into particle kinetic energy. Credit: Aharonian, Bogovalov, and Khangulyan, 2012a.

Wind zone model

This model locates particle acceleration and gamma-ray production in the outer magnetosphere or wind zone (Aharonian, Bogovalov, and Khangulyan, 2012b). Near the LC the outflow is Poynting-dominated. Acceleration occurs within a narrow region at 20–50 · LC radii, where the flow becomes kinetic energy-dominated (see Fig. 2.15). The dominant channel is IC of the cold wind on IR, UV and X-ray photon fields from the stellar surface and magnetosphere. This framework reproduces the Crab pulsar spectrum up to a few hundred GeV (the phase-resolved Crab pulsar spectrum up to 1.5 TeV is reported in Fig. 2.16). TeV emission, however, would require wind acceleration at radii much larger than model expectations (Ansoldi et al., 2016).

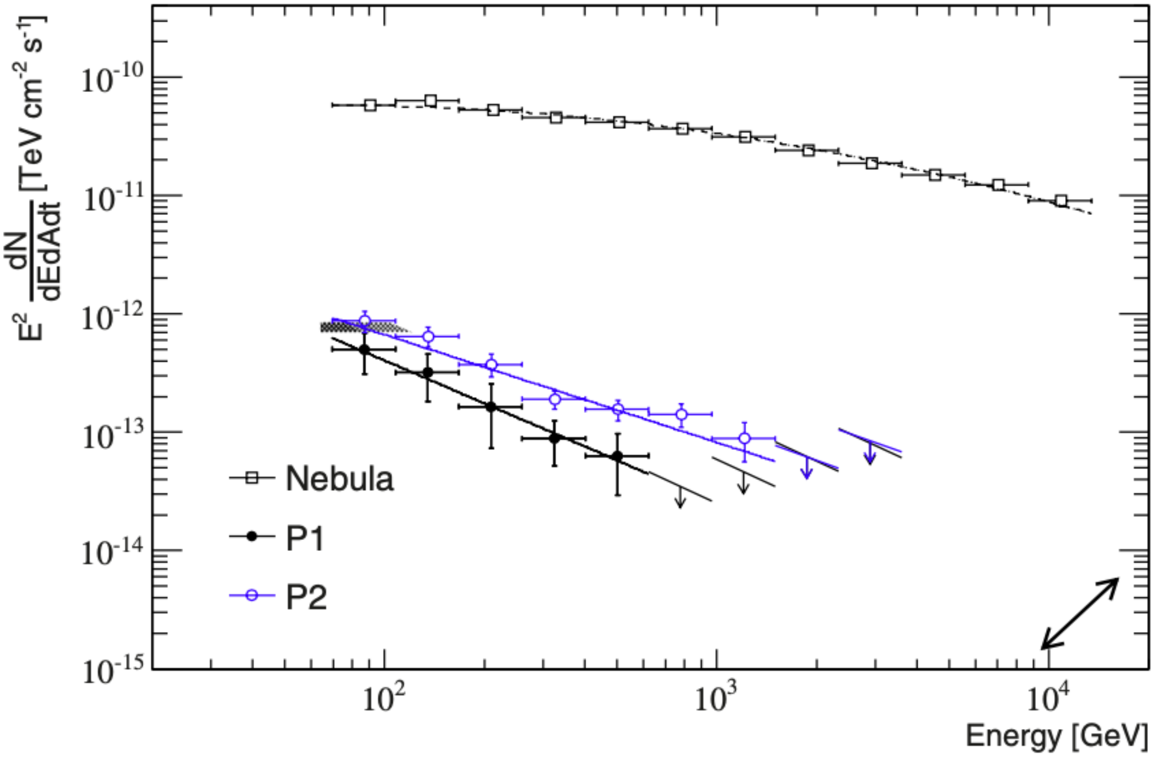

Figure 2.16: Phase-resolved SED of P1 (black circles) and P2 (blue circles) of the Crab pulsar obtained from the MAGIC telescopes dataset. The Crab Nebula spectrum (open black squares) is also shown for comparison.
Credit: Ansoldi et al., 2016.

Current sheet model

Current sheet model identifies the sheet and the separatrix as promising sites of efficient particle acceleration in pulsars. Numerical simulations indicate that these regions host the strongest electric fields under nearly force-free conditions, enabling particle acceleration (A. K. Harding, Venter, and Kalapotharakos, 2021). Models based on IC scattering in the sheet have been proposed to account for multi-TeV emission, and were already applied to Vela before the recent H.E.S.S. detection (A. K. Harding, Kalapotharakos, et al., 2018). However, the extension of the spectrum up to $\sim 20\,\mathrm{TeV}$ poses significant challenges to these predictions.

An alternative explanation attributes the gamma-ray emission to SCR occurring in the current sheet of the stripped wind (Coroniti, 1990, Pétri, 2012, Mochol, 2017). Beyond the LC, if the magnetic and rotational axes are misaligned, the sheet oscillates with the pulsar rotation, producing a striped structure that separates opposite polarities. The observed pulse profile arises when the line of sight intersects this geometry (see Fig. 2.17). In this framework, acceleration results from magnetic reconnection in the sheet, with GeV photons generated by rapid synchrotron cooling of the accelerated plasma. Additional IC interactions can in principle produce TeV photons, a scenario applied for explaining the emission recently detected from Vela up to 20 TeV (H. E. S. S. Collaboration, F. Aharonian, et al., 2023).

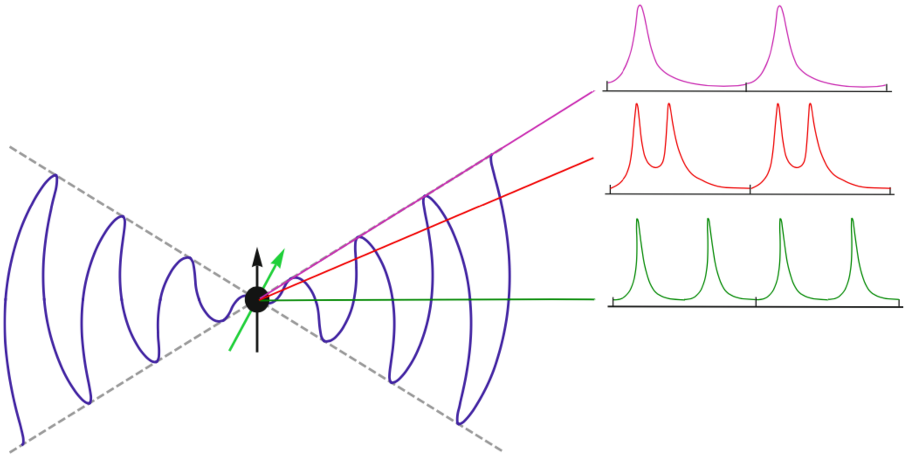

Figure 2.17: Schematic view of the stripped pulsar wind and the associated current sheet. If the magnetic and rotational axes are misaligned, the current sheet oscillates with the pulsar spin, producing a striped pattern that separates regions of opposite polarity. The observed pulse profile arises when the line of sight intersects this geometry, with particle acceleration and emission occurring in the reconnection layers of the sheet.
Credit: Mochol, 2017.

The contrasting behaviors of Crab and Vela highlight the complexity of pulsar gamma-ray emission across the HE and the VHE bands. GeV radiation is likely dominated by CR, while emission above hundreds of GeV, probably due to IC scattering, remains poorly understood. Notably, Crab appears to exhibit a single spectral component from GeV to TeV energies, whereas Vela displays two distinct components. This uncertainty motivates searches for additional VHE pulsars, a goal that depends on improved sensitivity from future facilities such as CTAO. This work presents an initial step toward this objective, based on observations of Crab pulsar performed with LST-1, the first CTAO telescope.

2.4 Crab pulsar

Crab pulsar is one of the three pulsars detected by IACTs so far. In particular, together with Vela pulsar, it is the only one emitting above 1 TeV, as discussed in Section 2.2.2.

Figure 2.18: The Crab Nebula as seen by Hubble Space Telescope (left) and James Webb Space Telescope (right).
Credit: NASA, ESA, J. Hester and A. Loll (Arizona State University), `https://science.nasa.gov/asset/hubble/a-giant-hubble-mosaic-of-the-crab-nebula/`;
NASA, ESA, CSA, STScI, T. Temim (Princeton University), `https://www.nasa.gov/missions/webb/the-crab-nebula-seen-in-new-light-by-nasas-webb/`.

Located at the center of the Crab Nebula (described in Section 2.4.1), Crab pulsar (RA: 05h 34m 31.9s, Dec: +22° 00’ 52.2”) is a young, energetic neutron star with a spin-down power of $\dot{E} \approx 4.6 \times 10^{38}$ erg s^{-1} (Lyne, Jordan, et al., 2015). Its rotation period is $P \approx 33$ ms (Staelin and Reifenstein, 1968). Discovered in the radio band (Comella et al., 1969), it emits all over the electromagnetic spectrum. A multi-band image of the nebula, with the pulsar visible as a central white spot, is shown in Fig. 2.19.

2.4.1 Crab nebula

The Crab Nebula (Fig. 2.18 and 2.19) is the remnant of SN 1054 observed by Chinese and Arab astronomers. Situated at around 2 kpc from Earth, it is a prototypical Pulsar Wind Nebula (PWN; see Section 1.3), powered by the relativistic outflow from the Crab pulsar. In this system, the pulsed emission from the neutron star is distinct from the nebular radiation, which originates from particles accelerated in the termination shock of the pulsar wind. These particles, mostly leptons, emit SR and SSC (Mas Aguilar, 2025).

Figure 2.19: Composited image of the Crab Nebula (left image) with X-ray observations by Chandra (upper right), optical by the Hubble Space Telescope (middle right), and infrared by Spitzer Space Telescope (lower right). The Crab pulsar is located at the center of the Nebula and is intense in X-rays. Credit: NASA/CXC/SAO/STScI/JPL-Caltech, `https://chandra.harvard.edu/photo/2018/crab/`.

The Crab Nebula serves as a stable reference source for VHE calibration. Ground-based instruments such as MAGIC (Nepomuk Otte, 2007), VERITAS (Meagher and VERITAS Collaboration, 2015), and H.E.S.S. (Holler et al., 2015) have measured its spectrum beyond 10 TeV, with MAGIC extending observations to 100 TeV (MAGIC Collaboration et al., 2020b).

Milagro (Abdo, B. T. Allen, et al., 2012), TIBET ASγ (Kawata and Tibet ASgamma Collaboration, 2019), and HAWC (Abeysekara et al., 2019) have confirmed emission above 100 TeV, while LHAASO reported photons in the PeV range (Lhaaso Collaboration et al., 2021).

The SED in Fig. 2.20 shows the double-peaked structure expected from SSC models, with the synchrotron peak at lower energies and the IC peak extending to the highest measured gamma-ray energies.

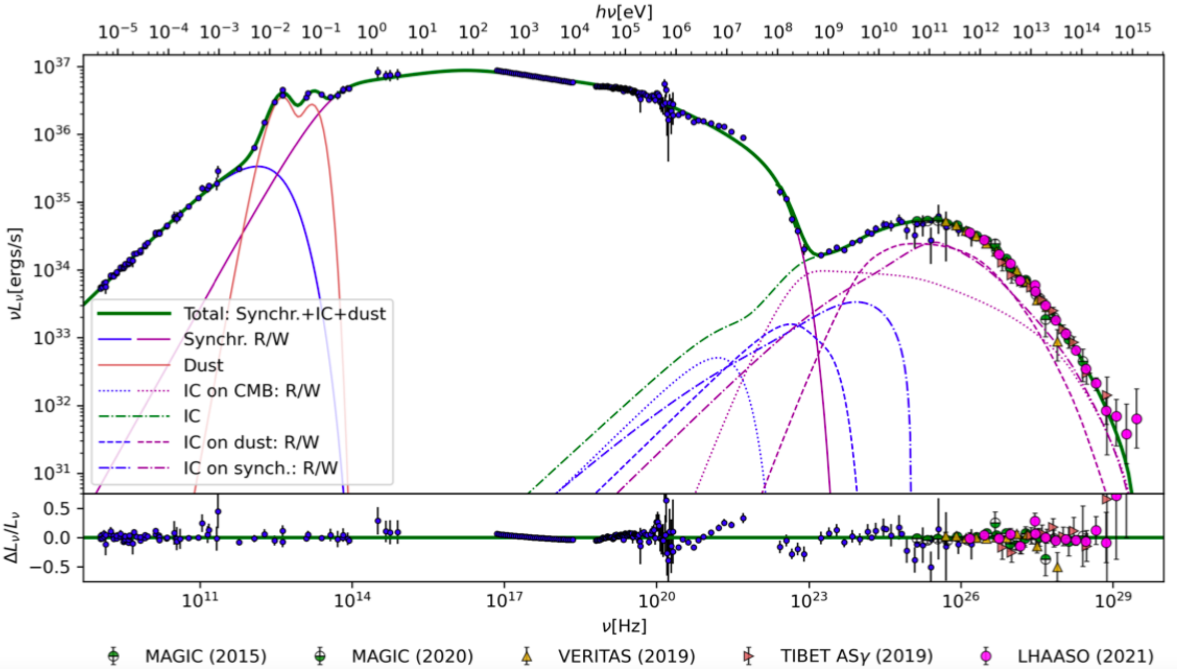

Figure 2.20: Broadband emission of the Crab Nebula, spanning from radio to PeV gamma rays. VHE gamma-ray data from multiple instruments, including MAGIC, VERITAS, TIBET ASγ, and LHAASO, are displayed. The observed spectrum is reproduced by combining different emission processes across the electromagnetic spectrum. Two prominent components are evident: synchrotron radiation and inverse Compton, the latter described by the SSC process.
Credit: Dirson and Horns, 2023.

2.4.2 Pulsed emission

The spatial coincidence of the Crab pulsar with a supernova remnant triggered decades of multiwavelength studies. Phase-resolved analyses revealed a stable phaseogram, or folded light curve, featuring two sharp peaks aligned across the electromagnetic spectrum (see Fig. 2.21). Below, observations spanning different energy domains are summarized.

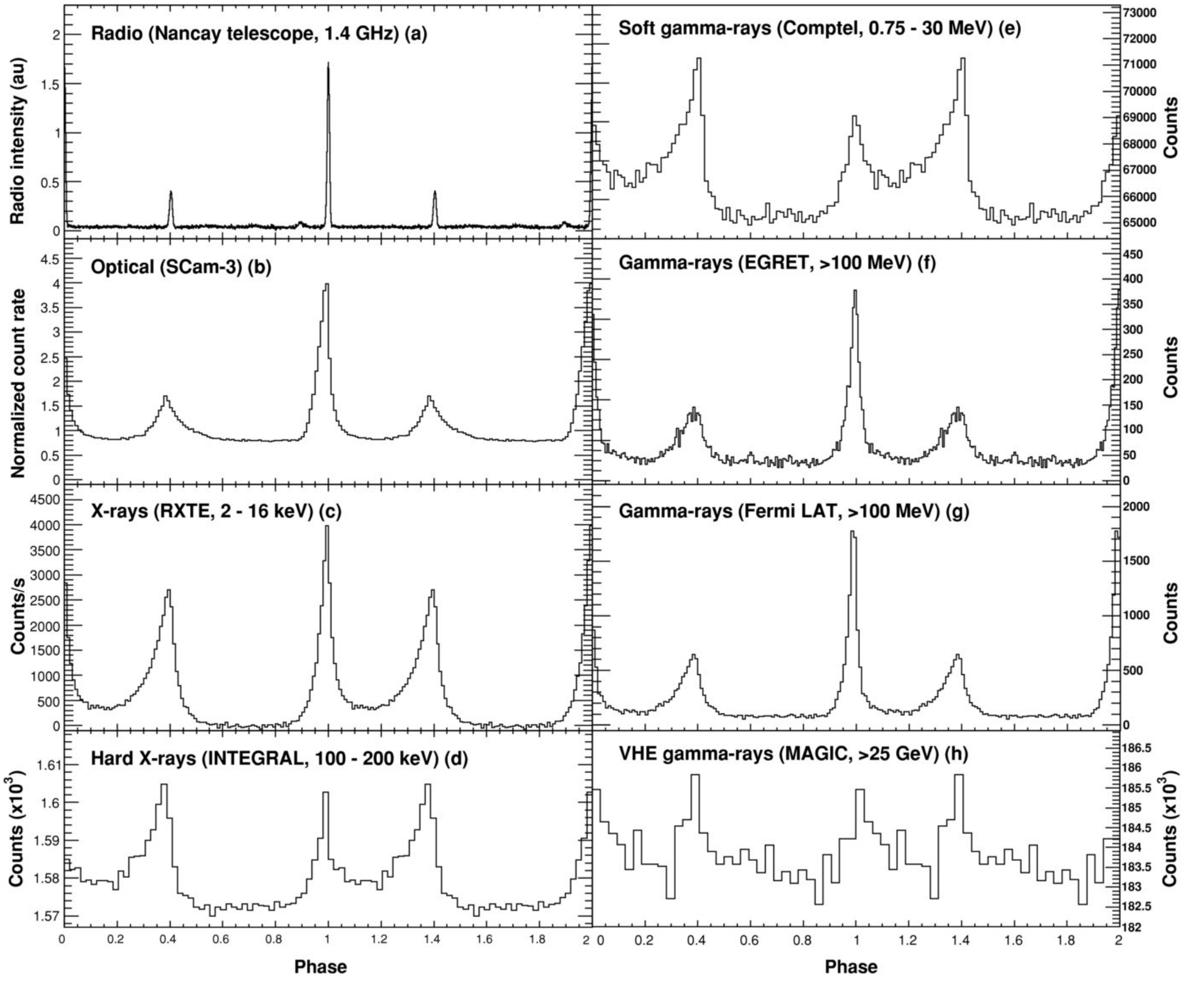

Figure 2.21: Crab pulsar phaseograms across the electromagnetic spectrum, from radio to very high energy gamma rays. The phaseogram shows emission intensity versus rotational phase, typically plotted over two cycles for clarity. A property of the Crab is the phase stability of its two peaks across all bands, while their relative amplitudes and morphology change.
Credit: Abdo, Ackermann, et al., 2010.

Radio observations

The Crab pulsar was discovered as a radio source in 1968 (Lovelace, Sutton, and Craft, 1968; Staelin and Reifenstein, 1968), showing the characteristic pulsed emission with two peaks. Fig. 2.22 shows the average pulse shapes obtained at that time, determined by summing data corresponding to a large number of pulse periods. The radio phaseogram has remained stable over decades, establishing the reference against which multiwavelength comparisons are made.

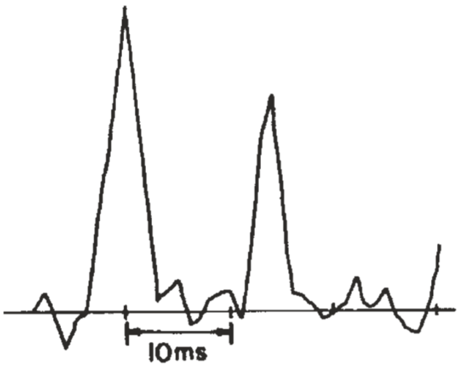

Figure 2.22: Early radio pulse profiles of the Crab pulsar, obtained in 1968 by integrating a large number of periods to enhance the signal-to-noise ratio. It shows the characteristic double-peaked structure that has remained stable over decades.
Credit: Comella et al., 1969.

Optical and X-ray observations

Following the radio discovery, the Crab was quickly detected optically (Nather, Warner, and Macfarlane, 1969), one of fewer than ten pulsars with observed optical pulsations. The optical phaseogram closely matches the radio one.

X-ray pulses were first reported by G. Fritz et al. (1969), constituting $\sim 5\%$ of the total emission and showing two peaks similar to those in radio. Early spectra suggested a power-law shape with a photon index of 0.2-0.6 and a possible break at tens of keV (Gilbert Fritz et al., 1971, Toor and Seward, 1977). Later observations above 5 keV with BeppoSAX, INTEGRAL, and NICER revealed peak intensity variations with energy (Mineo, Cusumano, et al., 1997), and phase and energy-dependent spectral changes (Pravdo, Angelini, and A. K. Harding, 1997, Mineo, Ferrigno, et al., 2006, Yan et al., 2022).

Gamma-ray observations

The first evidence of pulsed emission in the MeV range was reported by SAS-II (Kniffen et al., 1974) and later confirmed with higher statistics by COS-B (Clear et al., 1987). Observations with EGRET/CGRO extended the studies above 100 MeV (Nolan et al., 1993, Fierro et al., 1998), revealing two narrow peaks separated by ~ 0.4 in phase. Their relative intensities were found to vary with energy (Kuiper et al., 2001), although the peaks remain phase-aligned with those detected at lower energies (see Fig. 2.21). In this regime, the Crab spectrum followed a power law with a spectral index of ≈ 2.

Fermi-LAT observations (Abdo, Ackermann, et al., 2010) in the HE domain identified a spectral cutoff at ~ 6 GeV, in agreement with SCR models, which predict negligible emission above 100 GeV.

Early attempts to detect pulsations in the VHE range were unsuccessful, with HEGRA measuring only the emission from the Nebula (F. Aharonian, A. Akhperjanian, et al., 2004). Later, as discussed in Section 2.2.2, MAGIC detected pulsed emission between 25 and 100 GeV (Aliu et al., 2008), followed by VERITAS detections above 100 GeV (VERITAS Collaboration, 2011), establishing the Crab as the first pulsar emitting in the VHE regime. Subsequent MAGIC and VERITAS studies (Aleksić et al., 2011, Aleksić et al., 2012, Nguyen and VERITAS Collaboration, 2015) extended the detected emission up to 400 GeV, excluding polar cap models that limit pulsar emission to a few tens of GeV. More recently, MAGIC reported pulsed photons up to 1.5 TeV (Ansoldi et al., 2016), strongly suggesting an IC origin for the VHE component.

This thesis focuses on the VHE observations of the Crab pulsar. The results of the analysis are provided in Chapter 5, and are consistent with the framework outlined above, where pulsed emission extends up to the TeV range and challenges standard models. Given the small number of pulsars detected at these energies and the limited sensitivity of current instruments, the use of LST-1 data demonstrates the important role that CTAO will play in establishing a larger pulsar population and in testing new theoretical models.

3. Imaging Atmospheric Cherenkov Telescopes (IACTs)

Imaging Atmospheric Cherenkov Telescopes (IACTs) are designed to detect the Cherenkov light emitted by relativistic particles in extensive air showers initiated by gamma rays in the atmosphere (see Appendix B and C for details). Large parabolic mirrors focus the brief flashes of Cherenkov radiation onto fast-response, high-gain photomultiplier tubes (PMTs) arranged in pixelated cameras. The recorded images trace the longitudinal development of the shower, typically appearing elliptical in the case of gamma-ray-induced events. From the image parameters, such as shape, orientation, and total intensity, it is possible to reconstruct the energy, arrival direction, and nature (gamma or hadron) of the primary particle. Fig. 3.1 shows a general scheme of the IACT technique.

Two major sources of background challenge IACT observations: the Night Sky Background (NSB) and hadronic showers produced by cosmic rays. Observations are therefore performed under dark-sky conditions[1] to reduce NSB contamination, while advanced Monte Carlo simulations and machine-learning classifiers are employed to distinguish gamma-ray events from the overwhelming hadronic background.

Modern IACTs generally operate in stereoscopic mode, combining simultaneous observations from multiple telescopes. This configuration significantly improves event reconstruction, yielding angular resolutions of ~ 0.1 deg and energy resolutions of about 15%. The achievable energy threshold is primarily determined by the telescope size, reaching values as low as ~ 20 GeV with the largest mirrors.

The development of IACTs began with the Whipple telescope (Lewis, 1990), which pioneered the technique and achieved landmark detections of sources such as the Crab Nebula (Weekes et al., 1989), Mrk 421 (Punch et al., 1992), and Mrk 501 (Quinn et al., 1996). This was followed by experiments like CAT (Cherenkov Array at Thémis; Barrau et al., 1998) and HEGRA (High-Energy Gamma-Ray Astronomy; F. A. Aharonian and Heinzelmann, 1998), active between 1998 and 2002. HEGRA represented a milestone in the field, enabling discoveries such as Cassiopeia A (F. Aharonian et al., 2001) and M87 (F. Aharonian et al., 2003).

---

[1] IACTs can also operate under moonlight. However, this degrades the performance, especially at low energies, due to the higher NSB.

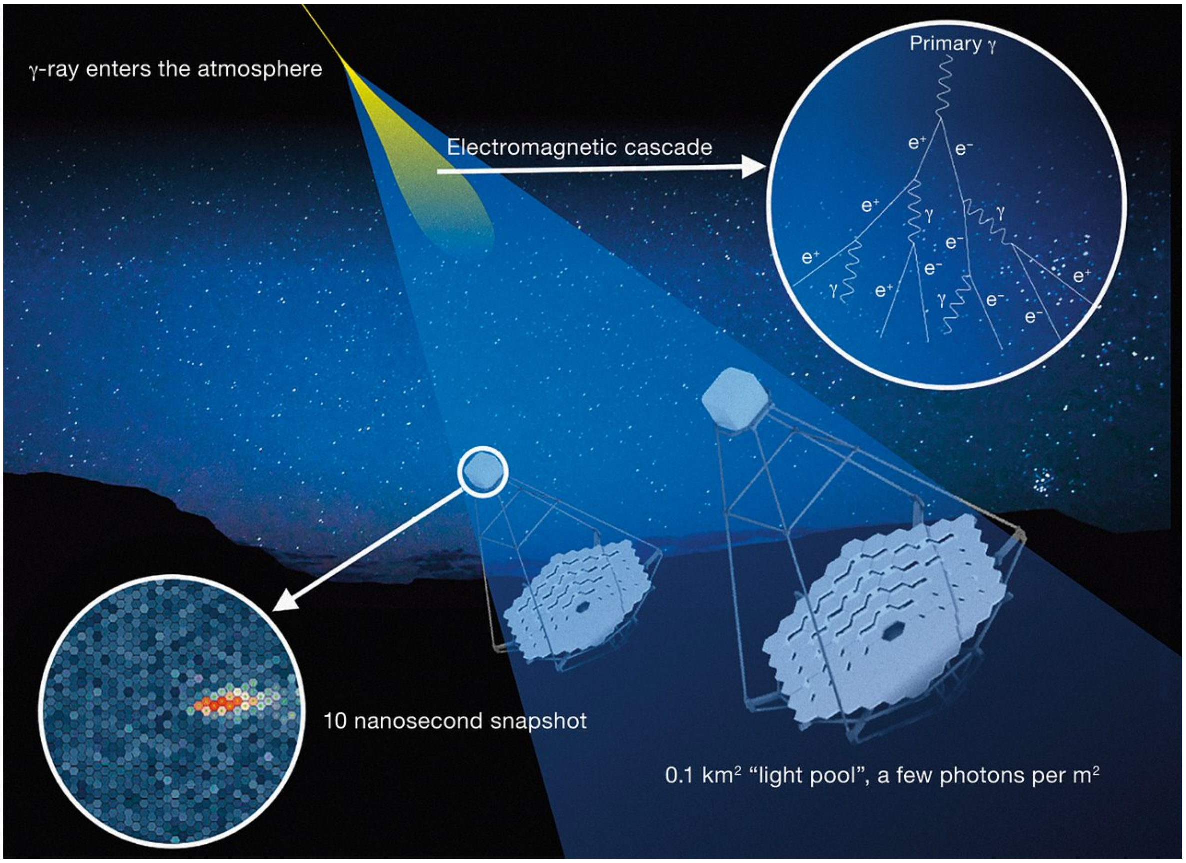

Figure 3.1: Artistic representation of the Imaging Atmospheric Cherenkov Telescopes (IACTs) technique. Cherenkov light produced in an atmospheric shower is reflected by a large mirror and focused onto a camera, where the shower image is recorded.
Credit: CTAO/ESO, `https://www.eso.org/public/images/eso1841x/`.

Subsequent arrays have established the current state of the art in gamma-ray astronomy:

- H.E.S.S. (High Energy Stereoscopic System; Benbow, 2005): located in Namibia, this array consists of four 12m telescopes and a central 28m unit (operational since 2012). It covers the energy range from 100 GeV to 100 TeV with a sensitivity of 0.7% of the Crab flux. Its wide ~ 5 deg FoV has enabled large-scale surveys such as the H.E.S.S. Galactic Plane Survey (HGPS) (H. E. S. S. Collaboration, Abdalla, et al., 2018), as well as notable results including detections from the Vela pulsar in both sub-100 GeV and TeV bands (H. E. S. S. Collaboration et al., 2018, H. E. S. S. Collaboration, F. Aharonian, et al., 2023).

- MAGIC (Major Atmospheric Gamma Imaging Cherenkov) telescopes (De Lotto and

Magic Collaboration, 2012): two 17 m telescopes located on La Palma (Spain), operating in stereo mode since 2008. With a threshold of $\sim$ 50 GeV and a sensitivity of 0.8% of the Crab flux, MAGIC features rapid repointing capabilities ($\sim$ 20 s). It has produced relevant results such as the detection of pulsed emission from the Crab pulsar (Aliu et al., 2008, (Ansoldi et al., 2016)), as well as the first TeV detections of GRBs (MAGIC Collaboration et al., 2019) and novae (Acciari et al., 2022).

- VERITAS (Very Energetic Radiation Imaging Telescope Array System): an array of four 12m telescopes located in Arizona (United States), operational since 2007. It achieves an energy threshold of about 100 GeV and offers a FoV of $\sim$ 3.7 deg. VERITAS has delivered important results such as detailed studies of the Cygnus region (Abeysekara, Archer, et al., 2018) and the detection of Crab pulsar emission above 100 GeV (VERITAS Collaboration, 2011).

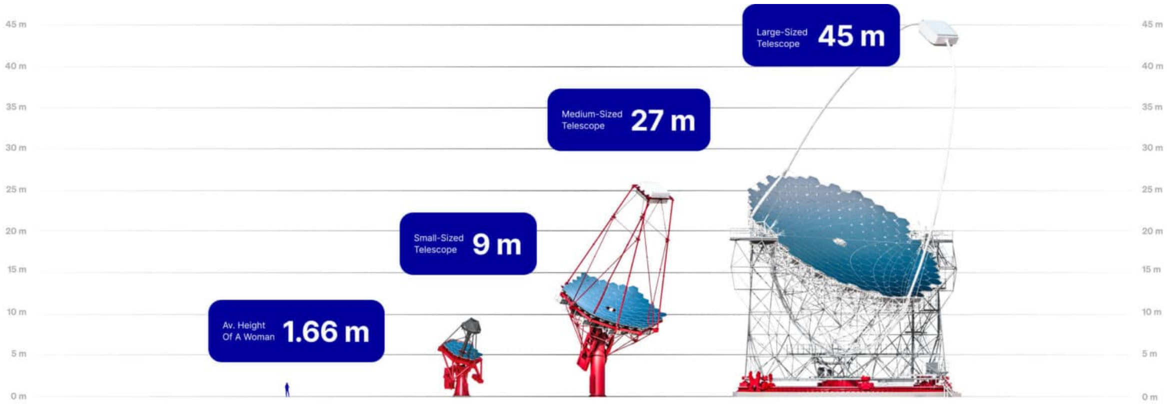

Figure 3.2: The three telescope classes foreseen in the CTAO design, compared to the average human height. Small-Sized Telescopes (SSTs) will probe the highest energies, Medium-Sized Telescopes (MSTs) the intermediate range, and Large-Sized Telescopes (LSTs) the lowest energies.
Credit: `https://www.ctao.org/emission-to-discovery/telescopes/`.

3.1 Cherenkov Telescopes Array Observatory (CTAO)

After more than two decades of IACT operation, current instruments are reaching their sensitivity limits. The Cherenkov Telescope Array Observatory (CTAO) represents the next-generation facility. Compared to current IACTs, CTAO is designed to improve sensitivity by a factor of 5-10, angular resolution by a factor of 2-3, and energy coverage in the VHE domain, which is expected to be between 20 GeV and 300 TeV (Gueta, 2022). To achieve this, CTAO will operate as a global observatory composed of several IACTs of different sizes, working together as a single, coherent system.

With the participation of over 1500 scientists from 25 countries and more than 150 institutes, CTAO will be the largest and most advanced gamma-ray observatory ever built. Its infrastructure, which includes telescopes of different sizes, will be deployed on two sites to ensure full-sky coverage: one array in the Northern Hemisphere, in La Palma, Spain, and another in the Southern Hemisphere, in Paranal, Chile. The headquarters of the observatory is located in Bologna (Italy), while data management is coordinated from Zeuthen (Germany).

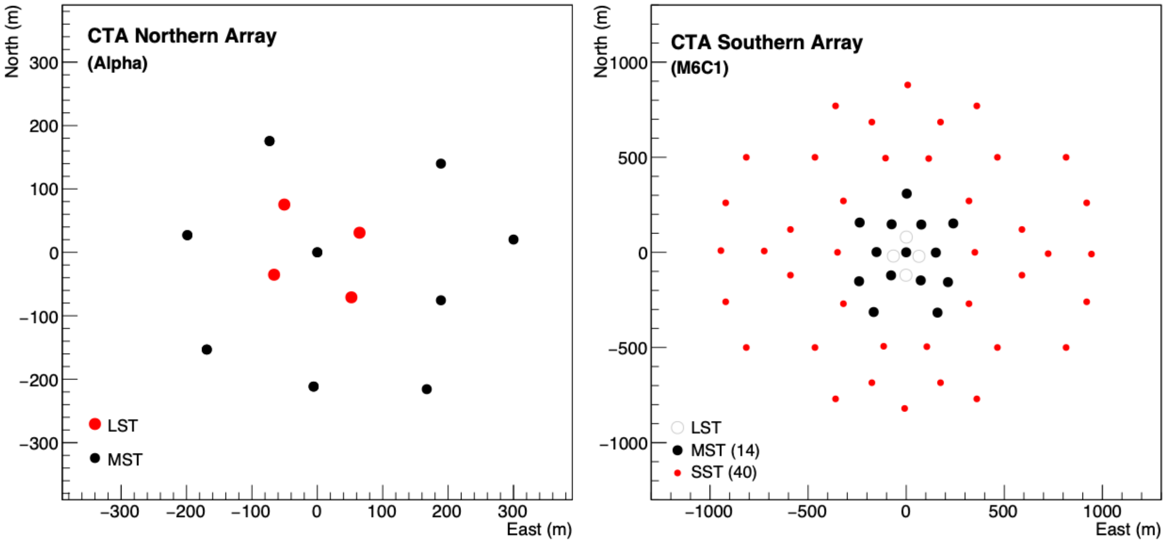

Figure 3.3: Layout of the CTAO Northern and Southern array. Credit: Gueta, 2022.

3.1.1 Design and configuration of CTAO

The CTAO concept relies on three telescope classes, shown in Fig. 3.2, each optimized for a distinct energy band:

1) Large-Sized Telescopes (LSTs): 23m parabolic reflectors optimized for the 20–150 GeV domain, providing sensitivity to the lowest energies. Despite their large structure, they can repoint to any sky position within 20 s. The first prototype, LST-1, is currently in the commissioning phase and will be described in Section 3.2.

2) Medium-Sized Telescopes (MSTs): 12m reflectors designed for the core range between

150 GeV and 5 TeV. Their cameras, based on PMTs, feature a wide FoV. The design follows previous implementations in HEGRA, H.E.S.S., and VERITAS. A prototype operated in Berlin between 2012 and 2020 to validate components, test system interfaces, and define the assembly procedures.

3) Small-Sized Telescopes (SSTs): 4.3m dual-mirror reflectors equipped with silicon photomultiplier (SiPM) cameras and a wide FoV. These telescopes target the highest energies, from 5 to 300 TeV. The concept was validated with the ASTRI-Horn Cherenkov prototype and subsequently advanced through the ASTRI mini-array project (Vercellone et al., 2022), currently under construction in Tenerife, Spain.

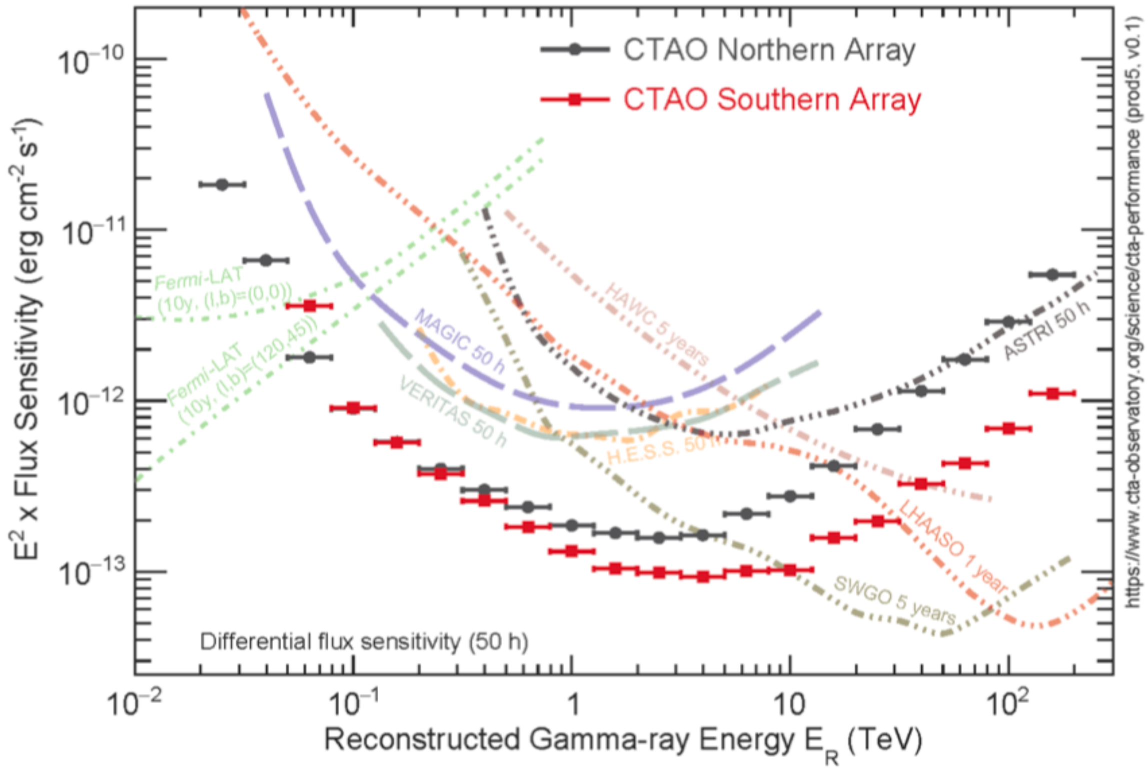

Figure 3.4: Differential flux sensitivity of CTAO (for 50 hours of observation) compared with current instruments.
Credit: `https://www.ctao.org/for-scientists/performance/`.

The planned layout is illustrated in Fig. 3.3. The Northern Array (Alpha configuration) will comprise 4 LSTs and 9 MSTs over an area of ~ 0.25 km^2, optimized for low-energy phenomena such as pulsars, GRBs, and distant AGNs. The Southern Array will host 14 MSTs and 37 SSTs across ~ 3 km^2, focusing on Galactic sources and candidate PeVatrons.

3.1.2 Performance and sensitivity

Fig. 3.4 compares the CTAO sensitivity in 50 hours of observation with that of other instruments. CTAO will outperform current IACTs over the entire energy range. The Southern array achieves superior sensitivity above 1 TeV, while both sites exhibit comparable angular resolution, as illustrated in Fig. 3.5. It is worth noting that CTAO will surpass the 1 year sensitivity of LHAASO below 10 TeV while offering enhanced angular precision, although not explicitly shown in the angular resolution plot.

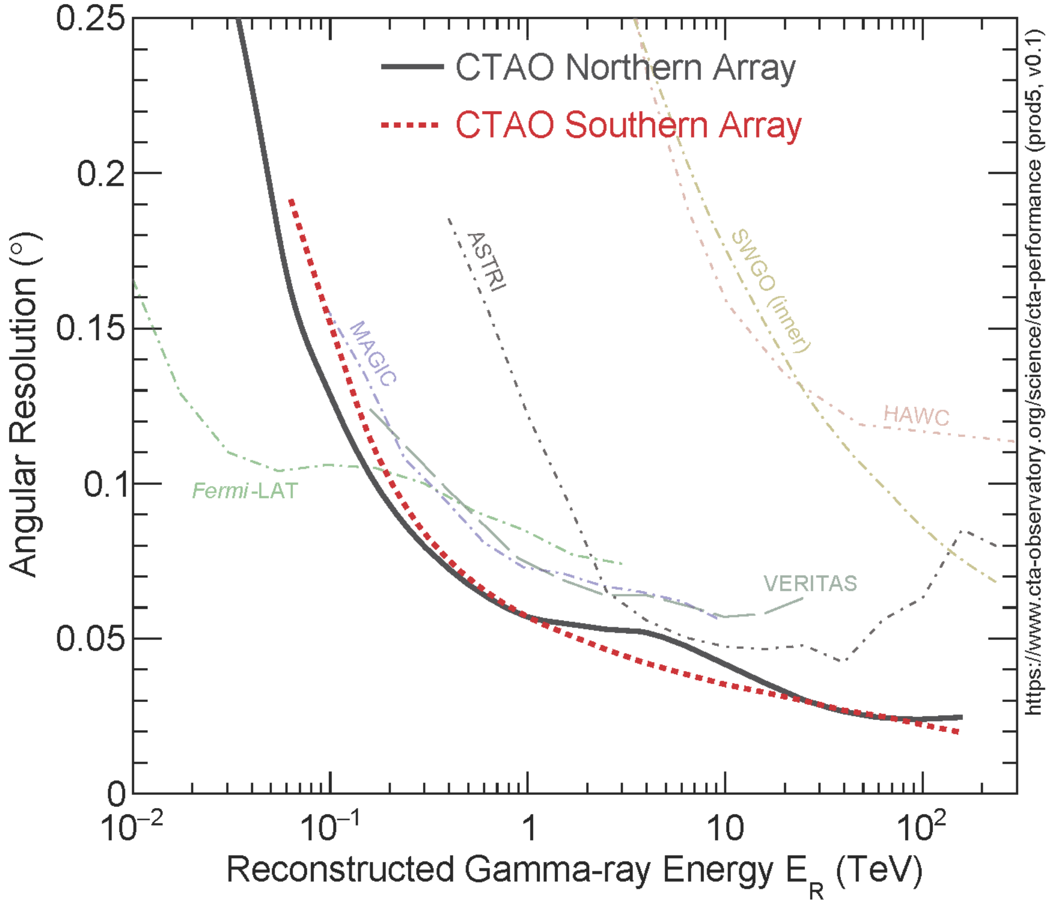

Figure 3.5: Angular resolution of CTAO compared with current instruments.
Credit: `https://www.ctao.org/for-scientists/performance/`.

3.2 First Large-Sized Telescope (LST-1)

The Large-Sized Telescopes are optimized for the detection of low-energy Cherenkov events, thus they are essential for pulsar studies, as well as for Galactic transients, AGNs, and GRBs.

The prototype LST-1 (see Fig. 3.6) was inaugurated in October 2018 at the Roque de los Muchachos Observatory, La Palma (Spain). As the first telescope of the CTAO-North array, it represents a cornerstone for the LST program and CTAO as a whole. Developed within the international LST Collaboration, the instrument has undergone a commissioning campaign, which is still ongoing, and is already producing its first scientific results. Its design is summarized below following Cortina and Project (2019), CTA-LST Project et al. (2024), and the official CTAO documentation.[2]

Figure 3.6: Picture of the prototype for the Large-Sized Telescopes, LST-1.

---

[2] `https://www.ctao.org`

3.2.1 Design and configuration of LST-1

LST-1 consists of a 23m parabolic reflector with a focal length of 28 m, composed of 198 hexagonal segments ($\sim$2 m^2 each), yielding a total reflective area of 370 m^2 (400 m^2 before shadowing). Each segment employs a sandwich design of glass plates and an aluminium honeycomb core. A dedicated Active Mirror Control (AMC) system compensates gravitational deformations, maintaining a point spread function (PSF) of $\sim$0.05 deg on-axis and $\sim$0.1 deg at 1 deg off-axis. Pointing accuracy better than 14" is achieved through a star guider and displacement monitor, which align the camera center with the stellar field every second. The $\sim$100-ton structure, built mainly from carbon fiber, enables fast repositioning (<20 s) in response to transient alerts. The drive system employs four azimuth and two elevation motors.

The LST-1 camera contains 1855 pixels organized in 265 modules, each hosting 7 fast-response PMTs ($\sim$3ns) optimized for Cherenkov detection. The camera provides a 4.5 deg FoV and a quantum efficiency of $\sim$40%. Each PMT output is digitized via a Domino Ring Sampler 4 (DRS4)-based system, including high- and low-gain channels. A 355 nm laser calibration unit mounted at the dish center ensures accurate photoelectron calibration.

A hierarchical trigger system reduces the data stream by selecting relevant events:

- L0: analog sum over the 7 pixels of each module
- L1: cluster trigger from neighbouring modules above threshold
- L2: planned hardware stereo trigger across multiple LSTs
- L3: software-level array trigger (SWAT) (Tejedor et al., 2022).

Trigger logic is managed by the Trigger Interface Board (TIB), which also synchronizes the internal clock. Triggered data are transferred to the Event Builder (EVB; Hoffmann and Houles, 2012) and stored on the computing cluster. Operations are supervised by the Telescope Control Unit (TCU), supported by environmental monitoring systems including LIDAR and weather stations.

Nanosecond-precision timestamping is provided by the Clock Distribution and Trigger TimeStamping (CDTS) system, based on the White Rabbit (WR) protocol. A GPS-disciplined oscillator feeds the WR network, which distributes 1 PPS and 10 MHz signals to the Unified Clock and Timestamp Systems (UCTS) at each telescope. The UCTS attaches precise timestamps to triggered events and forwards them to both TIB and EVB. Event timestamps are packed in 24-event blocks with shared headers, allowing efficient compression (Champion et al., 2017).

3.2.2 Commissioning and first results

Construction began in 2016 and culminated in the 2018 inauguration. Since then, LST-1 has been in extended commissioning. By June 2024, it had accumulated ∼2250 hours of data, including ∼780 hours in joint operation with MAGIC. Despite interruptions from the COVID-19 lockdown (2020), the Cumbre Vieja eruption (2021), and a structural issue (2022), the system maintained ∼75% uptime from 2019 onwards. After the eruption-induced optical degradation, performance returned to nominal levels.

The first scientific results confirmed that the telescope meets its design goals. In 2023, the LST Collaboration reported its initial publication on LHAASO J2108+5157 (S. Abe, Aguasca-Cabot, et al., 2023), followed by further results including Crab pulsar and Nebula observations (Abe et al., 2024). The latter is also used in this work for comparison (see Chapter 5). Construction of three additional LSTs at the CTAO-North site started in 2023, with full deployment expected by 2026, building on the experience gained with LST-1.

3.3 Impact on pulsar research

Pulsars represent one of the most relevant science cases for CTAO, especially because their rapid variability and hard spectra make them ideal targets for instruments with high temporal and spectral resolution. Observations in the VHE domain are particularly important, as they probe emission mechanisms that remain poorly understood and cannot be explained by classical models. The detection of pulsed emission well beyond the GeV cutoff predicted by the polar cap model, the outer gap model and the slot gap model (see Section 2.3.1) has demonstrated the need for new theoretical frameworks, where processes such as IC or magnetic reconnection play a central role in the wind zone of a pulsar.

LST-1 has already proven its capability in this domain through the detection of the Crab and Geminga pulsars (K. Abe et al., 2024, K. Abe et al., 2025), confirming that the instrument achieves the timing precision and sensitivity required for phase-resolved analyses. These results highlight the critical importance of the VHE observations in constraining theoretical models and in testing the presence of multiple emission components beyond the HE regime.

The construction of additional LSTs at the CTAO-North site will considerably enhance sensitivity and enable stereoscopic reconstruction, thereby improving background rejection and extending the accessible pulsar population. This step is significant for the detection of fainter pulsars which remain below the threshold of current-generation instruments. Thus, CTAO will potentially allow the first systematic survey of pulsars in the VHE regime through the proposed Galactic Plane Survey (S. Abe, Abhir, et al., 2024), providing unprecedented constraints on their emission geometry and acceleration processes.

Finally, the combination of CTAO with space-based facilities such as *Fermi*-LAT will make it possible to connect the GeV and TeV domains in a consistent multiwavelength framework. Higher sensitivity, broader energy coverage, and improved angular resolution position CTAO as a particularly suitable observatory for pulsar astrophysics, with the potential to reveal new populations of gamma-ray pulsars and to significantly advance our understanding of their emission in such extreme environments.

4. Crab pulsar analysis with LST-1

The Imaging Atmospheric Cherenkov Technique is intricate and demands a robust analysis pipeline due to challenges in rejecting the NSB and hadronic showers. In IACT (see Chapter 3), Cherenkov light generated in extensive atmospheric showers (EAS; see Appendix C) is collected by a camera equipped with PMTs. These signals are digitized by the readout electronics. The outputs from each pixel are combined to form an image of the shower. By comparing real events with Monte Carlo (MC) simulations, one can infer the particle type (gamma or hadron), its direction, and energy.

The LST-1 data analysis software is tailored to process the telescope data, from raw files to the filtered datasets used to derive scientific results. It follows the standard framework proposed by the Cherenkov Telescope Array Observatory (CTAO). This chapter outlines the LST-1 analysis pipeline used to analyze the Crab pulsar in this work.

4.1 LST analysis chain: an overview

The LST-1 analysis consists of several processing stages, called data levels (DL), summarized in Table 4.1 and schematized in Fig. 4.1. Each level involves specific tasks for the analysis:

1) Processing raw data (R0): the pipeline starts by processing the raw digital signals from the readout electronics, known as the R0 stage. These files serve as input for low-level analysis.

2) Pedestal correction and calibration (R0 to DL1a): electronic noise of each channel is corrected through pedestal correction, followed by calibration, transitioning from R0 to DL0. The calibrated signals are integrated to determine the charge and arrival time of the Cherenkov pulse for each pixel (DL1a). By combining all pixel signals, an image of the atmospheric shower is constructed.

3) Image cleaning and parametrization (DL1a to DL1b): shower images are cleaned by removing pixels with only NSB noise, leaving an image of the Cherenkov light. Gamma-ray-induced images typically have an elliptical shape in the camera. These images are parametrized, and the resulting parameters are added to the DL1 files, progressing to DL1b.

4) Event reconstruction (DL1b to DL2): image parameters are used to reconstruct the properties of primary particle that initiated the atmospheric shower. Using MC simulations, the energy, direction, and type (gamma or hadron) of the particle are reconstructed. The reconstructed parameters are stored in DL2 files.

5) Event selection (DL2 to DL3): after reconstruction, quality cuts are applied to remove the hadronic background. The Instrument Response Functions (IRFs) of the telescopes are added to the filtered files, producing DL3 files. These files adhere to a standardized format for sharing within the astrophysics community and contain all information required for high-level analysis. The software used up to the DL3 stage is called `cta-lstchain` (López-Coto et al., 2022), relying on `ctapipe` (Noethe et al., 2022), primarily via the `ctapipe-io-lst` plugin.

6) High-level analysis (DL3 to DL4/DL5): statistical measures, excess counts, and significance are calculated for each DL3 file, considering spatial and energy binning. The binned data are stored in DL4 files, which are later used to generate scientific products (DL5). The standardization of DL3 files allows the use of the open-source software `Gammapy` for analysis (Deil et al., 2017, Donath et al., 2023).

Data level (DL)	Description
R0	Raw data before calibration
DL0	Pixel-wise calibrated waveforms
DL1	Charge, time-integrated calibrated and cleaned, parametrized images
DL2	Events after their reconstruction and classification
DL3	Event list and IRF
DL4	Binned event data
DL5	Science products

Table 4.1: Data levels in the LST-1 analysis chain. The processing reduces raw data (R0) to final science products (DL5). The table lists, for each level, its designation, corresponding primary data file levels, and file contents.

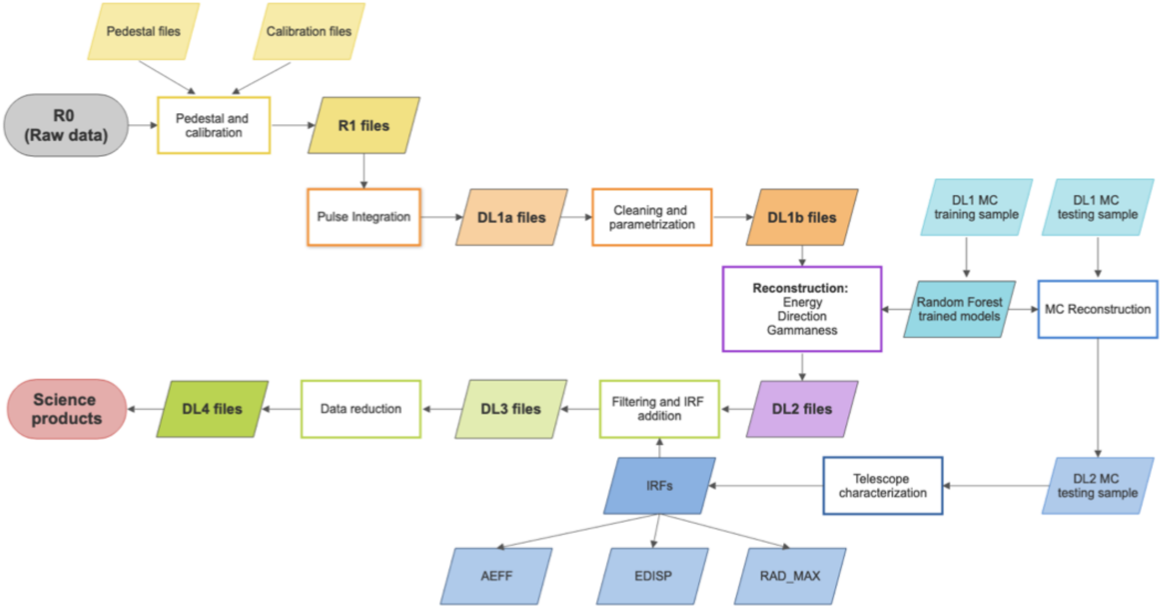

Figure 4.1: Flowchart of the LST-1 analysis chain. Raw data (R0) are sequentially processed to generate calibrated data (R1), calibrated images (DL1a), cleaned and parameterized images (DL1b), reconstructed datasets (DL2), and filtered DL3 files for scientific analysis. Supplementary Monte Carlo simulations and calibration datasets are required to model the telescope and electronics response. Credit: Mas Aguilar, 2025.

4.1.1 Observation modes

The choice of signal and background regions in the high-level analysis is determined by the observation mode of the telescope. IACTs typically employ two configurations, depending on the pointing relative to the target:

- ON/OFF mode: the source is placed at the center of the camera during ON runs, allowing an optimized measurement of the gamma-ray signal. Background estimation requires separate OFF runs, in which the telescope observes a region free of known gamma-ray sources.

- Wobble mode: the telescope tracks the source with an offset of about 0.4 deg. This provides simultaneous measurements of two regions: the ON region, containing both signal and background (0.4 deg offset), and the OFF region, a symmetric field with respect to the camera center (-0.4 deg offset), used to evaluate the background.

A schematic representation of these strategies is given in Fig. 4.2. While LST-1 initially employed the ON/OFF technique during early commissioning, it now adopts Wobble mode as its standard operational setup.

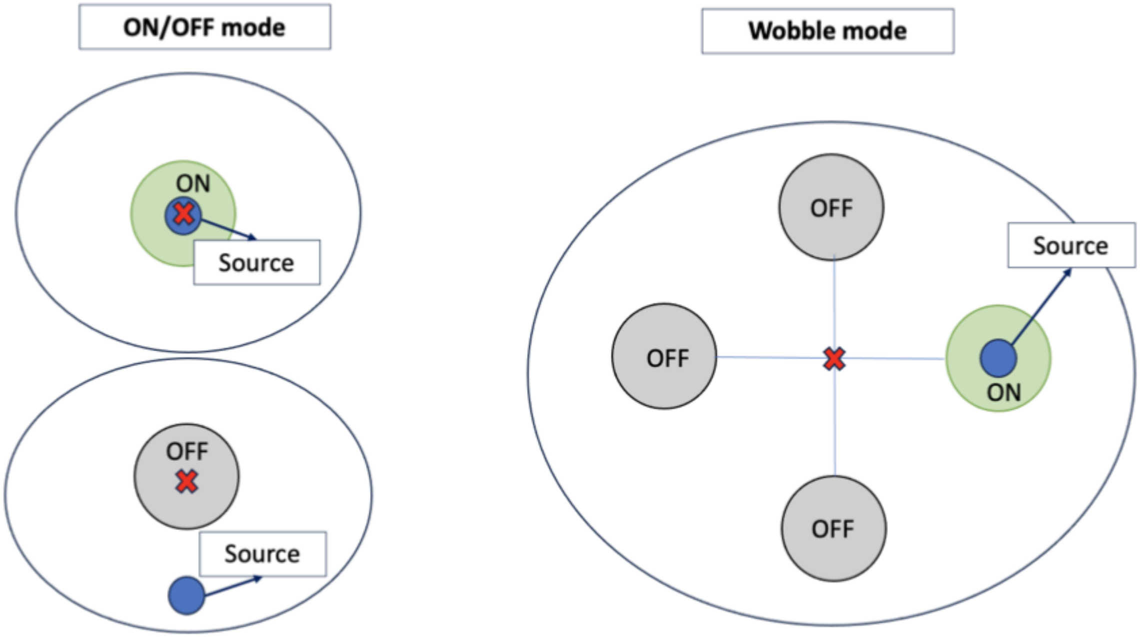

Figure 4.2: Schematic view of the ON/OFF and Wobble observation modes. In ON/OFF mode, the source is placed at the camera center during one run, while a separate run on a source-free field provides the background estimate. In Wobble mode, both ON and OFF regions are derived from the same run, with the source observed at an offset of ±0.4 deg from the camera center.
Credit: Mas Aguilar, 2025.

4.1.2 Data quality selection

Before producing DL2, all DL1 undergo a quality selection to exclude runs affected by poor atmospheric conditions, unstable telescope pointing, excessive NSB, or hardware issues. These checks ensure that only data meeting the required quality are retained for next steps analysis. The thresholds adopted may vary depending on the dataset and are specified in the source-specific analysis sections.

The procedure relies on parameters such as the Cherenkov transparency coefficient (dR/dI), pointing stability, zenith distance (Zd) limits, and pedestal noise levels. These indicators are evaluated on a run-by-run basis. Below are the criteria for some of the main cuts[1].

Pointing stability

Small drifts in telescope pointing during an observation can broaden the PSF, distort camera coordinates, and introduce spurious trends in parameters used for data selection. Pointing stability is evaluated from the equatorial coordinates of the telescope on subrun timescales, ensuring that the mean pointing direction remains constant. This guarantees uniform acceptance across the field of view and allows any variations in event rates or image parameters to be attributed to atmospheric or instrumental conditions rather than pointing shifts. Standard threshold value is $\sigma_\delta < 0.01$ deg.

Zenith distance

In IACT observations, the zenith distance determines the atmospheric path length of the shower and therefore the Cherenkov light yield recorded by the camera. Larger zenith distance increase airmass, reduce image brightness, and raise the low-energy threshold, while at high energies they can enlarge the effective area. The selection strategy balances the need for statistical coverage with low-energy performance and stability. There is no strict standard value for this cut, but observations with zenith distance below 35 deg are generally preferred. In some cases, runs up to 50 deg can still be considered acceptable, while at very high zenith distance data may be retained only to increase statistics, keeping in mind the trade-off with higher threshold and reduced sensitivity.

Cherenkov transparency dR/dI

This selection step uses the parameter dR/dI, which measures the differential in cosmic-ray rate as a function of image intensity. It is sensitive to atmospheric transmission: under optimal atmospheric conditions, the detected rate follows a predictable decrease with intensity, while poor conditions produce steeper slopes and lower rates.

For each subrun, dR/dI was obtained from DL1 datacheck histograms and fitted with a power law over 316-562 p.e. (photoelectrons), a range chosen to avoid low-intensity trigger effects and high-intensity statistical fluctuations. The power-law form provides two fit

---

[1] More details can be found here: `https://github.com/cta-observatory/cta-lstchain/blob/main/notebooks/data_quality.ipynb`.

parameters: the spectral index and the normalization (rate at the reference intensity of 422 p.e.[2]). Both quantities are corrected to their zenith distance equivalent at Zd = 0 to remove geometric airmass effects.

Standard selection criteria retained runs with a power-law index between -2.35 and -2.10 and a normalization above 1.5 events s^{-1} p.e., corresponding to clear-sky observations.

Additional stability and consistency checks can also be applied:

- Average fit p-value significance > -3 (normalized to the number of subruns), ensuring reliable fits across subruns.
- Maximum Lomb-Scargle periodogram amplitude $< 1 \times 10^{-2}$, rejecting runs with periodic dR/dI variations (e.g. LIDAR shots).
- At least 80% of subruns within ± 0.075 of the modal dR/dI at 422 p.e., indicating stable transparency throughout the run.

A further cut, called "intensity threshold", required the intensity at half the peak cosmic-ray rate to be ≤ 70 p.e., rejecting runs with abnormally high trigger thresholds and thus reduced low-energy sensitivity.

Moonlight brightness

Observations under strong moonlight conditions suffer from increased NSB, which lowers the instrument sensitivity, raises the trigger threshold, and limits the detection of faint showers.

Runs affected by moonlight were rejected based on the standard deviation of the pedestal charge, computed from pixels without nearby bright stars to avoid contamination from stellar light. This parameter correlates with the diffuse NSB level, and thus with moonlight contamination. A higher standard deviation indicates stronger pixel charge fluctuations, corresponding to a brighter background.

Standard data quality procedures retain only runs with a pedestal charge standard deviation below 2.3 p.e., effectively selecting moon-less data. Higher values typically correspond to observations taken with the Moon above the horizon or in bright sky regions.

---

[2] The choice of 422 p.e. comes from LST-1 performance and commissioning studies, where it was identified as an optimal reference point in the intensity range for stable fits and comparison across runs.

4.1.3 Low-level analysis

The low-level analysis comprises the required steps to transform raw data (R0) into reconstructed event data (DL2). It starts with pedestal corrections and calibration of pixel-wise waveforms, followed by charge extraction and image cleaning. The resulting shower images are then parameterized using geometrical and intensity-related descriptors. Finally, event reconstruction algorithms, trained on Monte Carlo simulations, provide estimates of the energy of the primary particle, arrival direction, and classification as gamma or hadron. These reconstructed parameters define the DL2, which serves as the basis for the subsequent event selection and high-level analysis.

Pedestal corrections

Pedestal corrections: the pedestal represents the baseline level of the electronic signals, defined as the mean ADC value in the absence of signals. Electronic noise per pixel is evaluated through a dedicated pedestal run, recorded with the camera closed, typically at the beginning of the night. This run provides the reference for pedestal corrections in all subsequent observations. Pedestal corrections comprise all adjustments applied to the raw signal to suppress any electronic artifacts due to intrinsic properties of the readout system.

For LST-1, three main corrections are performed (Sitarek et al., 2013, Kobayashi et al., 2022): subtraction of the constant offset in the signal produced by the residual voltage retained by the capacitors, timing correction due to fluctuations introduced by the dependence of the stored charge on the time elapsed since the previous readout, and spurious spikes removal, especially because of their possible similarities with the Cherenkov signal.

Charge integration and calibration

After pedestal subtraction, pulses from Cherenkov light become visible in pixels with significant signal. These pulses are then integrated within a defined time window to extract the charge and photon arrival time at the camera by employing algorithms for charge extraction.

The integration yields the total charge per pixel in ADC units. To convert these values into physical units (p.e.), a calibration procedure is required. The ADC-p.e. conversion factor is determined through FlatField (FF) runs, where the camera is uniformly illuminated by a laser at the start of each night. By analyzing calibration pulses, it is possible to estimate the average ADC counts per pixel. Assuming photoelectron statistics follow a Poisson distribution, the ADC-p.e. factor is obtained using the F-factor method, which connects the charge distributions of calibration and pedestal events to the number of photoelectrons in a pixel (see Mirzoyan, 1997 for details).

Image cleaning and image parametrization

Following calibration, an image of the atmospheric shower becomes visible. To obtain a reliable reconstruction, each image must undergo a cleaning procedure, known as image cleaning, that removes spurious contributions from pixels associated with the NSB rather than with the shower itself. The algorithm used in the LST-1 analysis chain relies on three main parameters: picture threshold, which defines the brightest pixels in the camera forming the core of the shower image, boundary threshold, which recovers the outer regions of the image and excludes pixels below this limit, and the minimum number of neighboring pixels, which rejects isolated fluctuations that may survive after applying picture and boundary thresholds. Further improvements are achieved by retaining pixels with consistent signal arrival times or by applying a minimum intensity cut relative to the brightest pixels.

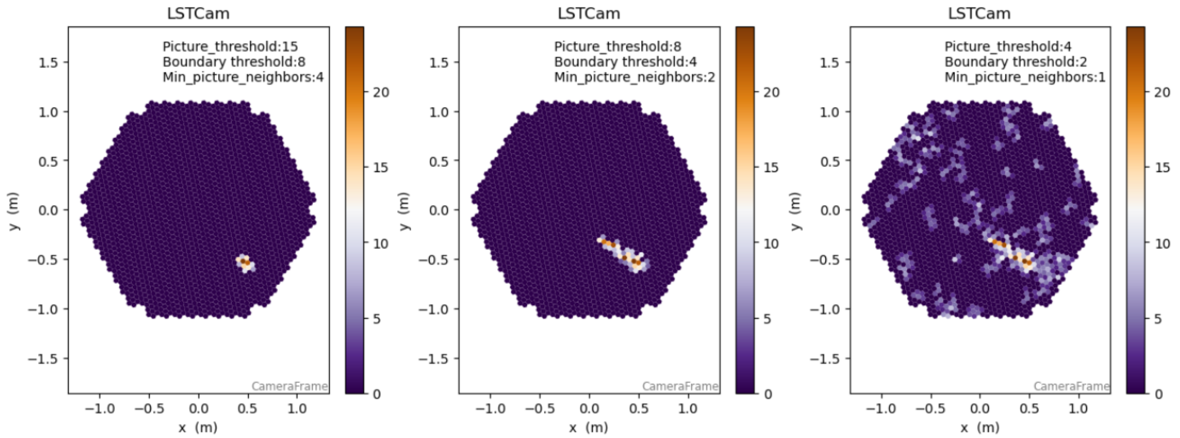

Figure 4.3: Simulated gamma-ray shower image in the camera with NSB noise, shown after applying three different sets of cleaning parameters (reported in each graph). In the first image, high thresholds remove part of the shower image, while in the last panel residual NSB noise remains visible after cleaning.
Credit: Mas Aguilar, 2025.

Fig. 4.3 illustrates examples of images produced by Cherenkov light after different cleaning levels. Using relaxed thresholds can leave residual NSB contamination, while strict thresholds risk truncating the shower edges. The standard LST-1 analysis adopts the following values for the parameters: 8 p.e. for the picture threshold, 4 p.e. for the boundary threshold, and 2 for the minimum neighbors.

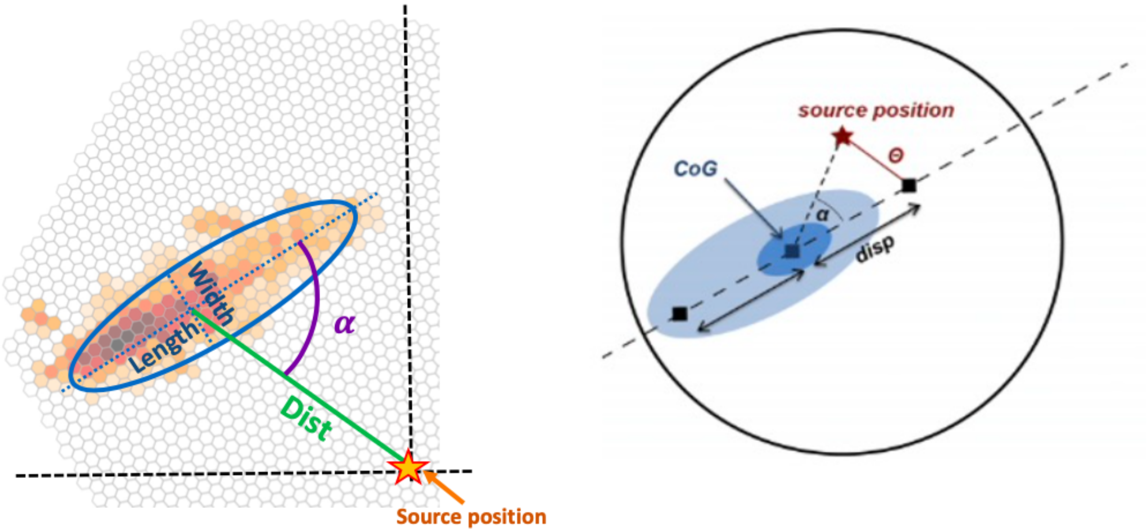

Figure 4.4: Main Hillas parameters defined by the shower geometry and the source location. Credit: Carreto Fidalgo, 2019.

After cleaning, the image of a gamma-ray induced shower in the camera generally exhibits an elliptical shape. The characterization of this geometry is performed through the Hillas parameters (Hillas, 1985), defined as the second-order moments of the charge distribution recorded by the camera. The most relevant parameters include:

- Length: extension of the ellipse along its major axis.
- Width: extension along the minor axis.
- Intensity: total charge within the ellipse in photoelectrons. It correlates with the energy of the primary particle and is the most important parameter for energy reconstruction.
- Leakage: fraction of the shower image that lies outside the camera field of view.
- Skewness: asymmetry of the charge distribution within the ellipse.
- Kurtosis: sharpness of the charge distribution, providing information on the spread of its tails.

- Dist: angular separation between the true source position and the image centroid.
- Alpha (α): angle between the major axis of the ellipse and the line connecting its centroid to the source position in the camera plane.
- Theta (θ): angular distance between the true and the reconstructed positions.

Dist, alpha, and theta are additional parameters that can be computed if the source position is known (see Fig. 4.4).

All extracted image parameters are stored in the DL1 files, formatted in HDF5 and containing the full description of the shower image.

4.1.4 Event reconstruction

Information extracted from the signal arrival times and the spatial charge distribution (i.e. the shower image) is employed to infer the properties of the initiating particle. Since hadronic showers can mimic those induced by gamma rays, discriminating the particle type is essential. In the LST-1 standard analysis chain, this task is performed using Machine Learning methods, specifically Random Forests (RF; Breiman, 2001).

RF models require training on pre-labeled datasets. For LST-1, this is achieved with MC simulations. Primary gamma rays are propagated through the atmosphere with CORSIKA (Domingo-Santamaria et al., 2005), while the telescope response is modeled with `sim_telarray` (Bernlöhr, 2008). These simulations are processed with `lstmcpipe` (Garcia, Vuillaume, and Nickel, 2022) under conditions similar to real observations.

RFs are trained to estimate three primary properties of the incoming particle:

- Reconstructed energy: a regression model provides the particle energy. High-energy showers develop deeper in the atmosphere, leading to larger, brighter images. At lower energies, images are fainter and smaller, making direction reconstruction more uncertain, particularly in mono observations. Additionally, muon-induced images resemble those from low-energy gamma rays, introducing a background that even well-trained RFs struggle to suppress.
- Reconstructed direction: the arrival direction is reconstructed using the DISP method, which requires computing the parameter disp, namely the angular separation between

the source position and the image centroid (see right panel of Fig. 4.4; Domingo-Santamaria et al., 2005). A RF regression estimates disp under the assumption that the source lies on the image major axis.

- Particle classification: the final step is to determine the nature of the primary particle to suppress the hadronic background. Hadron-induced showers are typically broader and more irregular than gamma-ray showers (see Fig. C.2). A classification RF assigns each event a *Gammaness* score from 0 to 1, with high values indicating a gamma-like origin.

The reconstructed parameters, energy, direction, and *Gammaness*, are stored in DL2 files, while pixel-level information is discarded to reduce data volume.

Stereo IACT arrays outperform single-telescope observations in direction reconstruction. For mono observations, such as with LST-1 only, angular accuracy decreases, especially for faint showers. To mitigate this, a source-dependent analysis is used. Unlike the standard source-independent approach, the RFs include parameters depending explicitly on the known source position (e.g. the time gradient measured relative to the source, the dist parameter). This method enhances performance at low energies, making it particularly effective for pulsar studies.

4.1.5 Gamma/hadron separation and cut optimization

After producing the DL2 files, which contain the reconstructed parameters (energy, direction, and gamma/hadron classification), the next task is to suppress the cosmic-ray background. This is achieved through the *event selection* step, where cuts are applied on two parameters: *Gammaness* and the angular direction.

Since the reconstruction performance depends on energy, the dataset is divided into reconstructed energy bins, with independent cuts determined for each. Optimization is carried out with MC test samples.

Gammaness distribution

Gammaness distribution provides discrimination between hadrons and gamma rays. Hadrons are assigned low *Gammaness* values, while gamma rays cluster at higher ones. At high energies, the discrimination is clear, while at low energies it is less effective.

Gammaness cuts are chosen in each energy bin to retain a fixed fraction of MC gamma rays, known as the *Gammaness MC efficiency*.

Angular distribution

The angular parameter used in the event selection depends on whether the analysis is source-independent or source-dependent.

In a source-independent analysis, the relevant parameter is the θ parameter defined in the previous Section 4.1.3. Since gamma rays are supposed to originate from the source position, they usually have small values of θ^2. Hadrons, instead, are distributed isotropically in the sky, so they have a flat θ^2 distribution. The left panel of Fig. 4.5 shows both gamma rays and hadrons angular distributions, where the excess at low θ^2 corresponds to gamma rays from the source. By comparing this excess to the background level, one can assess the significance of a detection.

In a source-dependent analysis, it is assumed that all gamma rays originate from the nominal source position, called the ON region. The discriminating variable is the *alpha* parameter defined in the previous Section 4.1.3, which plays a role similar to θ^2 (see Fig. 4.5). Events with small alpha values are more likely to come from the source. The background is estimated from the so-called OFF regions, typically chosen symmetrically with respect to the camera center.

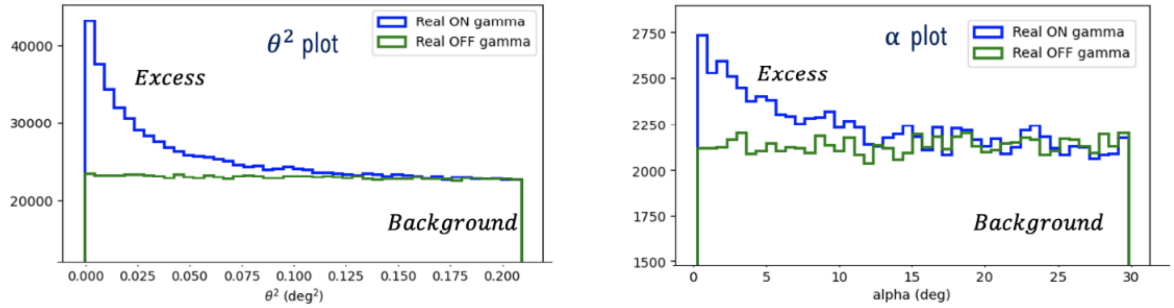

Figure 4.5: Examples of θ^2 and α distributions from data taken with LST-1. The low-value excess corresponds to gamma rays originating from the source.
Credit: Mas Aguilar, 2025.

Angular cuts are optimized in a similar way as for *Gammaness* by selecting the θ^2 (source-independent) or α (source-dependent) threshold that preserves a given fraction of MC gamma rays, referred to as *containment* or α *containment*, respectively.

The choice of gamma-ray efficiency and containment values involves a compromise. Loose cuts preserve most gamma rays but allow more background, whereas strict cuts suppress background at the cost of discarding genuine events. The optimal configuration depends on the target source. For example, pulsar emission peaks at low energies where the classification is less effective, requiring softer cuts to maximize gamma-ray retention despite higher background. Standard values of MC efficiency and containment are set to 0.7.

Further constraints on the Hillas parameters are often necessary. A common requirement is a minimum cut on image *intensity* (i.e. the integrated charge of the shower image), which suppresses events close to the telescope trigger threshold. Such events are strongly affected by muon and cosmic-ray contamination, and their images are too small for a reliable Hillas parametrization.

4.1.6 Instrument Response Functions (IRFs) and DL3 production

Before performing high-level analysis, raw event counts from the telescope must be converted into physical flux. The reconstructed flux is, however, highly dependent on observational conditions. For example, the gamma-ray detection rate for a given source varies with zenith distance because of the changing atmospheric depth. Likewise, camera inefficiencies may introduce systematic errors in the reconstructed energy.

To correct for these effects, the telescope response must be characterized under varying conditions. For LST-1, this response is derived from MC simulations. The simulated data are processed through the same pipeline as real observations to generate Instrument Response Functions (IRFs), which quantify the telescope performance (more details are provided in Mas Aguilar, 2025). Three main IRFs are:

- Effective area (A_{eff}): it defines the sensitivity of the telescope to gamma rays of a given energy and direction. It depends on factors such as the physical area of the telescope, mirrors reflectivity, and camera detection efficiency.

- Energy dispersion (E_{disp}): it describes the energy resolution and bias of the telescope. It is provided by the probability of assigning a reconstructed energy E_{reco} to a simulated gamma ray with true energy E_{true}.

- PSF: it quantifies the angular resolution of the telescope, namely the probability of reconstructing an arrival direction $\vec{d}_{reco}$ of a gamma ray given its true direction $\vec{d}_{true}$.

The overall telescope response results from the combination of these three IRFs. Then, the observed flux can be connected to its corresponding absolute value by convolving the overall telescope response with the IRFs.

Within the LST-1 analysis, IRFs are computed using `cta-lstchain`, which relies on `pyirf` (Linhoff et al., 2023)). The resulting IRFs are stored in FITS format, with separate tables for each component.

After the response characterization, DL3 files are produced as final input for the next high-level analysis (Section 4.1.7). These files are released upon publication to guarantee reproducibility. Their creation from DL2 data involves two steps:

1. Cuts on *Gammaness*, angular separation, and additional Hillas parameters: only events passing these criteria are stored in the DL3 FITS file, in a dedicated Event List table accessible to Gammapy, the standard tool for high-level analysis.
2. IRFs are added to the DL3 files to reflect the actual observational conditions. Since IRFs are simulated for different sky positions, two strategies exist (Dominik et al., 2024): assign the IRF corresponding to the closest simulated sky position, or interpolate between available IRFs to derive the optimal one for the specific source position. Standard LST-1 analysis uses the first one.

As a result, DL3 files include both: the events information in a table called *Event List* and the appropriate IRFs for the observation. The parameters stored in the Event List are summarized in Table 4.2. These files provide all the necessary inputs to produce scientific results, while the pulsar-specific analysis products are discussed in Chapter 5.

NAME	DESCRIPTION	MANDATORY
`EVENT_ID`	Identifier of each event in the file	Yes
`TIME`	Elapsed time since epoch time [s]	Yes
`RA/DEC`	Equatorial coordinates of the source [deg]	Yes
`ENERGY`	Reconstructed energy obtained from Random Forests	Yes
`GAMMANESS`	Gammaness obtained from Random Forests	No
`MULTIP`	Multiplicity parameter, set to 1 since only one telescope operates	No
`GLON/GLAT`	Galactic coordinates of the source [deg]	No
`ALT/AZ`	Pointing of the telescope [deg]	No

Table 4.2: Parameters stored in the Event List table of the DL3 files generated with `lstchain`. The first column specifies the parameter name, the second provides its description, and the third indicates whether it is mandatory or not.

4.1.7 High-level analysis

High-level analyses can be performed using the DL3 files to produce the science products required for studying the physical properties of the observed source. In gamma-ray astronomy, the main outputs generally include detection significance, energy spectra, sky maps (usually useful for studying extended sources), and light curves.

Detection significance

The significance of a signal is related to the number of excess events, normalized to the expected background level. The excess is defined as:

$$N_{EX} = N_{ON} - \alpha N_{OFF} \tag{4.1}$$

where N_{ON} is the number of ON events, N_{OFF} the number of OFF events, and α a normalization factor. Their values depend on the observation modes (see Section 4.1.1):

- ON/OFF mode: N_{ON} corresponds to the number event measured in ON runs, while N_{OFF} refers to those from OFF runs. Here, α depends only on the ratio between the exposure times of the two observations.

- Wobble mode: N_{ON} and N_{OFF} are the number events in the ON region and the OFF regions, respectively. In this case, α is determined by the number of OFF regions defined. Multiple OFF regions can be defined to mitigate possible camera inhomogeneities which eventually produce fluctuations (see Fig. 4.2).

The significance can be estimated assuming that the detected events follow a Poisson distribution:

$$S = \frac{N_{EX}}{\sqrt{\alpha N_{OFF}}} \tag{4.2}$$

though this expression systematically overestimates the true value. A more robust formulation was introduced by Li and Ma (1983):

$$S = \sqrt{2}\left(N_{ON}\ln\left[\frac{1+\alpha}{\alpha}\left(\frac{N_{ON}}{N_{ON}+N_{OFF}}\right)\right]\right) + \left(N_{OFF}\ln\left[(1+\alpha)\left(\frac{N_{OFF}}{N_{ON}+N_{OFF}}\right)\right]\right) \tag{4.3}$$

This formula is applied to evaluate any excess above background, including Crab pulsar excesses in phaseograms (see Section 4.2.4).

Gammapy computes the statistics and the IRFs (N_{ON}, N_{OFF}, N_{EX}, α, etc.) across different energy and spatial bins, producing geometrical maps (Donath et al., 2023) stored in the so-called *Datasets*. For each observation (namely each DL3 file) one dataset is created, and these datasets are then stored as DL4 files. This avoids recomputation once the DL3 analysis is completed. From DL4 files, the three main science products can be derived (DL5 files): spectral energy distribution (SED), and light curves.

Spectral energy distributions (SEDs)

The gamma-ray flux can be written in terms of excess counts N, effective area A, time t, and energy E, usually called *differential energy spectrum* of a source:

$$\frac{d\phi}{dE} = \frac{dN}{dE dA_{eff} dt} \tag{4.4}$$

Multiplication by E^2 yields the *spectral energy distribution* (SED):

$$E^2 \frac{d\phi}{dE} = E^2 \frac{dN}{dE dA_{eff} dt} \tag{4.5}$$

Because excess counts are evaluated in bins of reconstructed-energy, they do not directly provide the true-energy spectrum. To infer the source spectral model (such as a power law of the form $d\phi/dE = \phi_0(E/E_0)^{-\alpha}$) from the events and the IRFs, two approaches exist:

- Unfolding, which unfolds the IRFs with the observed counts in each reconstructed energy bin to obtain the flux in true-energy bins. The result is a set of flux points correlated through a correlation matrix. A spectral model in true energy can then be fit to these points. This method avoids assuming a spectral model for the flux points computation, but is computationally complex.
- Forward folding, which is the approach adopted in LST-1 analysis. In this case, a spectral model is assumed a priori, and is convolved with the IRFs to obtain the model in reconstructed energy. Then, the model parameters are fit to the observed data through a likelihood function computed for the observed counts in each energy bin, and the best-fit parameters of the model maximize this likelihood. Finally, flux points are derived by fitting again in each energy bin setting the normalization factor free.

Light curves

Another science product is the light curve, which potentially constrains the source variability. It is computed by splitting the data sample into time bins and integrating the differential flux per each time bin. The bin width can be selected based on the variability timescale of the source and its brightness. The flux is obtained via a forward-folding fit after a spectral model is assumed.

The variability in a light curve is quantified with several methods. The most direct one is the χ^2 test (J. R. Taylor, 1982): for N time bins with measured fluxes $f_{obs,i}$ and a null hypothesis of a constant flux (no variability), the χ^2 statistic is:

$$\chi^2 = \sum_{i=0}^{N} \frac{\left(f_{obs,i} - f_{model}\right)^2}{f_{model}} = \sum_{i=0}^{N} \frac{\left(f_{obs,i} - f_{model}\right)^2}{\sigma^2} \tag{4.6}$$

where f_{model} is the constant expected flux. If the null hypothesis holds, the statistic follows a χ^2 distribution with a number of degrees of freedom (dof) equal to N-1.

A convenient value to use is the *reduced* χ^2:

$$\chi^2_{red} = \chi^2/\text{dof} \tag{4.7}$$

As a rule of thumb, values of χ^2_{red} near 1 indicate that the fit represents the data properly, while values below 1 suggest overfitting, and values above 1 indicate underfitting.

4.2 Crab pulsar analysis

The pulsar investigation demands high statistics and, therefore, an extended dataset. For this work, all available observations of LST-1 have been included. They span from the start of LST-1 operations in October 2018 to July 2025. Throughout this period, the telescope has been in the commissioning phase and remains so at present.

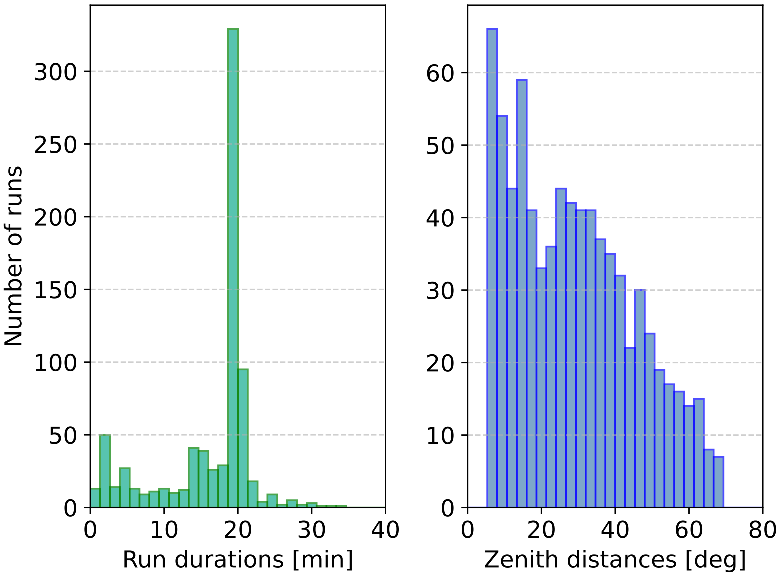

Figure 4.6: Distribution of run durations (left) and zenith distances (right) for the Crab pulsar observations with LST-1 from October 2018 until July 2025.

The Crab pulsar was observed using the standard Wobble configuration (see Section 4.1.1), with the camera center offset by 0.4 deg from the target. ON-OFF observations acquired in the same period were excluded from the analysis.

Data were collected in runs of roughly 20 minutes each. Low zenith distance observations were prioritized to better characterize the telescope response at the lowest energies (see Fig. 4.6).

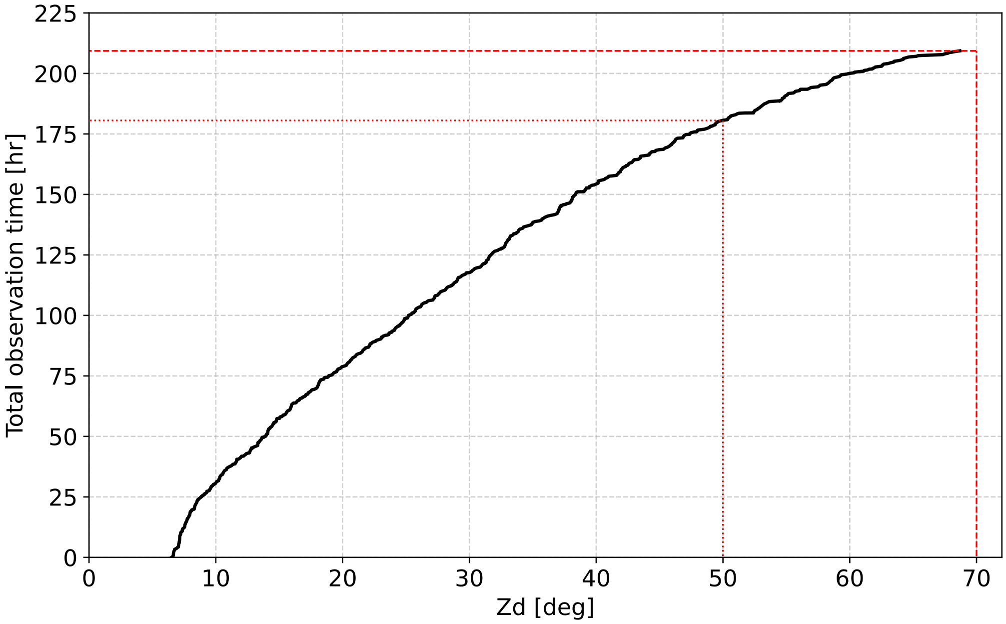

Figure 4.7: Total observation time as a function of zenith distance for all accepted runs after run-quality selection. The vertical dashed and dotted red lines indicate the limits at Zd = 70 deg and Zd = 50 deg, respectively. Horizontal lines mark the corresponding total exposures: ∼ 209 hr and ∼ 180 hr.

4.2.1 Data quality selection of the Crab pulsar

The Crab pulsar dataset was filtered following the standard LST-1 data quality procedure described in Section 4.1.2. All standard criteria were applied: zenith distance, moonlight brightness, pointing stability, and Cherenkov transparency (dR/dI). The moonlight brightness cut was set to a maximum pedestal charge standard deviation of 2.3 p.e., retaining only moonless conditions. Pointing stability was ensured by requiring $\sigma_\delta < 0.01$ deg, and the Cherenkov transparency cut adopted the standard index and rate thresholds. The zenith distance selection was initially set to Zd $\leq$ 70 deg to maximize statistics. As shown in Fig. 4.7, relaxing the cut from 50 deg to 70 deg increases the total observation time from about 180 hr to 209 hr. However, for the spectral analysis (see Chapter 5), the cut was later tightened to Zd $\leq$ 50 to limit low-energy threshold systematics.

Table 4.3 summarizes the number of runs remaining after each quality cut, together with the standard threshold values adopted for the LST-1 data quality selection. Percentages are given with respect to the number of runs after the zenith selection (1366 runs).

	Selection criteria	N. of runs	% w.r.t. zenith-select.
Sky region and date range	-	1370	-
Zenith	≤ 70	1366	-
NSB	≤ 2.3 p.e.	1167	85.4%
FF and pedestal presence*	-	1153	84.4%
Stable pointing	$\sigma_\delta < 0.01$ deg	1140	83.5%
dR/dI fit P-value	> -3	1126	82.4%
dR/dI max LS periodogram amplitude	$< 1 \times 10^{-2}$	1083	79.3%
dR/dI spectral index	[-2.35 and -2.10]	1026	75.1%
dR/dI rate at 422 p.e.	$> 1.5\ \frac{\text{events}}{s\ \text{p.e.}}$	797	58.3%
Intensity threshold	≥ 70 p.e.	**779**	57.0%

Table 4.3: Number of runs remaining after each quality cut. Percentages are relative to the number of runs after the zenith selection (1366 runs). After applying quality selection criteria, 779 runs are retained.

*Presence requirement for each run to contain interleaved flat-field (FF) and pedestal events.

After applying all the quality selection criteria, 779 runs were retained out of a total of 10651 LST-1 runs. This corresponds to an effective observation time of 209.72 hours for the selected dataset, covering observations taken between October 2018 and July 2025.

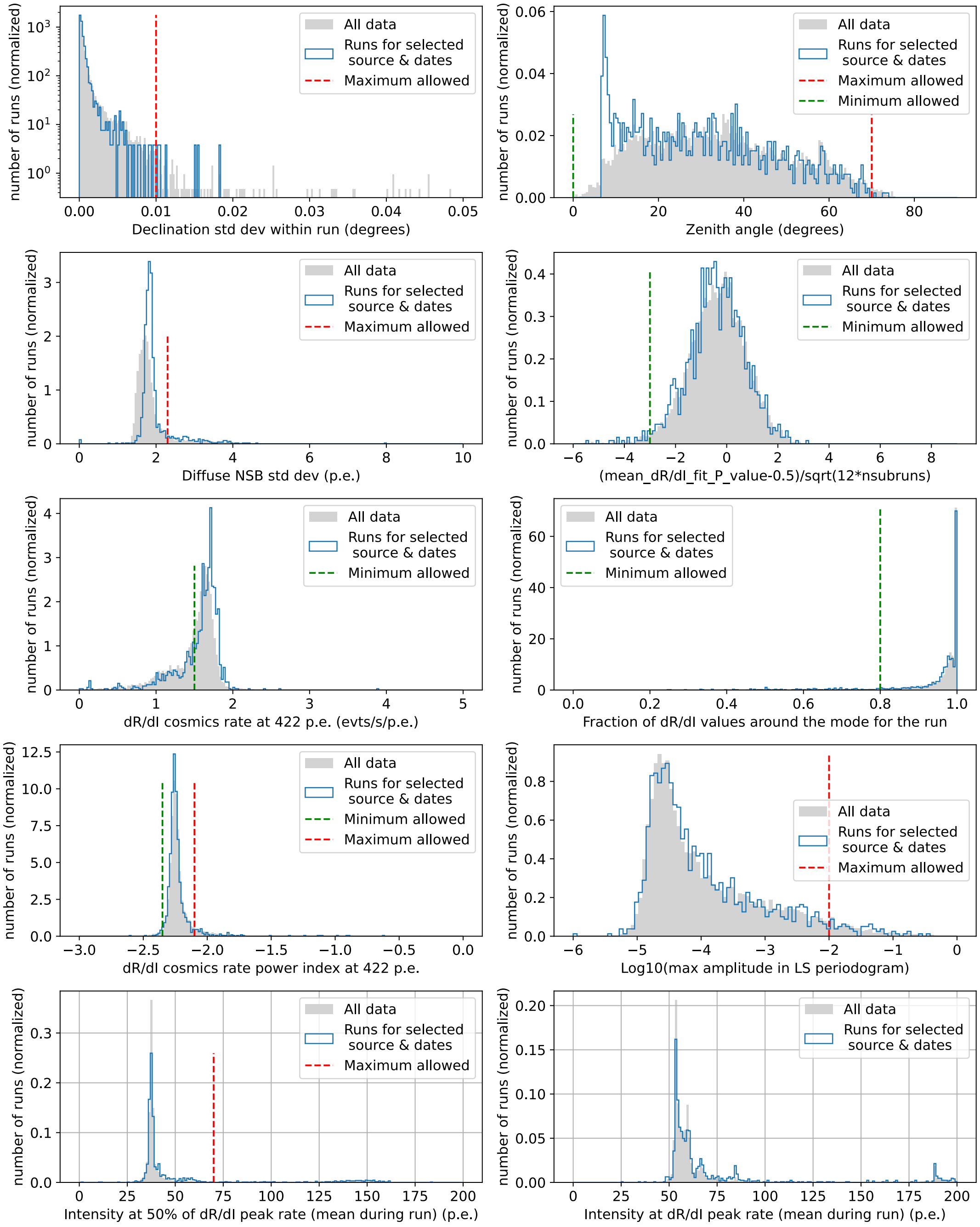

Figure 4.8: Quality selection summary. Gray histograms represent all runs available in LST-1 dataset, outlined histograms are runs after the source selection + date range preselection, and vertical lines show thresholds adopted in the data quality selection. Panels from top-left to bottom-right display: σ_δ, Zd, diffuse NSB std, mean fit -value, dR/dI at 422 p.e., fraction around dR/dI mode, spectral index, max Lomb–Scargle amplitude of dR/dI at 422 p.e., Zd-corrected intensity threshold (50% of the peak), and (uncorrected) intensity at peak rate.

To visualize how each quality criterion acts on the full sample, Fig. 4.8 summarizes the run-level distributions of all selection variables. Gray histograms show all runs of LST-1, normalized as probability densities (counts divided by total counts and by bin width), using the same bin edges for the preselected subset (sky region + date range) indicated by outlined histograms. Vertical lines mark the adopted thresholds. From top-left to bottom-right, the panels display: (i) intra-run pointing stability (σ_δ), (ii) zenith angle, (iii) diffuse NSB standard deviation, (iv) mean p-value of the power-law fit to the cosmic-ray intensity spectrum, (v) dR/dI at 422 p.e., (vi) fraction of subruns around the dR/dI mode, (vii) dR/dI spectral index, (viii) maximum Lomb-Scargle amplitude of dR/dI at 422 p.e. vs time, (ix) Zd-corrected intensity threshold (intensity at 50% of the peak rate), and (x) the intensity at peak rate (not Zd-corrected, shown only to guide later event-wise intensity cuts).

4.2.2 DL2 to DL3

For this work, DL2 files were already available within CTAO/LST Collaboration. These DL2 datasets have been generated using the standard RF models trained on MC simulations and were distributed as part of the LST-1 data processing chain (see Sections 4.1.3 and 4.1.4). Therefore, the analysis in this work does not involve the DL1 $\rightarrow$ DL2 stage, but focused instead on the subsequent conversion of DL2 into DL3 format, and the next high-level analysis steps.

The DL2 $\rightarrow$ DL3 step was performed using `lstchain-v0.10.18` (Moralejo et al., 2025), specifically through the script `lstchain_create_dl3_file.py`[3]. This script combines the reconstructed event parameters from the DL2 files with the IRFs of the telescope derived from MC simulations, producing DL3 files (see Section 4.1.6).

During this stage, standard event-selection criteria, summarized in Table 4.4 and described in Sections 4.1.4 and 4.1.5, were applied. These are the baseline cuts adopted in LST-1 performance studies and ensure a compromise between gamma-ray efficiency and background rejection. The main cuts are:

- *Gammaness* cuts: events with *Gammaness* ≥ 0.7 are kept, while those with lower values are rejected.

---

[3] `https://github.com/cta-observatory/cta-lstchain/blob/main/lstchain/tools/lstchain_create_dl3_file.py`

- Angular cuts (θ cuts): only events with $\theta \leq 0.7$ deg from the source position are kept.
- Intensity cuts: only events with image intensity ≥ 70 p.e. are kept; events with lower intensity are rejected because they are too noisy or poorly reconstructed.

Selection	Criterion
Gammaness	≥ 0.7
θ	≤ 0.7
Intensity	≥ 70 p.e.

Table 4.4: Standard event-selection cuts applied during the DL2 → DL3 conversion with `lstchain`.

The resulting DL3 files contain both the event lists and the corresponding IRFs, formatted in FITS, and serve as the standardized input for the high-level analysis with `Gammapy`. For pulsar studies, however, an additional step is required: DL3 files used in the subsequent analysis must also include the rotational phase information, as detailed in the next Section 4.2.3.

4.2.3 DL3 to DL3_pulsar

Pulsars produce radiation beams modulated at their rotation frequency. Since pulsars rotate extremely fast, with periods ranging from seconds to milliseconds, accurate and high-precision timing systems are required to resolve the emission phase of each event. Since individual pulses can last less than 5% of the rotation cycle, timestamp accuracy at the microsecond level is necessary, and LST-1 provides adequate timing resolution (see Section 3.2.1).

However, LST-1, as well as IACTs, are subject to several effects: Earth's rotation and orbital acceleration, clock instabilities at the telescope, and atmospheric propagation delays. These factors distort the measured arrival times and would smear the pulsar signal unless corrected. For this reason, all times must be referred to an inertial system, conventionally the Solar System Barycenter (SSB). Additional relativistic corrections due to photon trajectories (Roeamer delay, Shapiro delay, Einstein delay; see Maggiore, 2007) must also be applied.

At VHE, pulsar emission is faint compared to the background. Consequently, within a single rotational period, only a few events are detected, preventing direct identification of pulsations. To build a significant excess above background, observations spanning many hours, often distributed over weeks, months, or years, must be combined. Preserving the periodic signal in this process requires assigning each detected photon to the proper rotational phase. Since the pulsar spin frequency evolves with time, this phase assignment relies on *ephemeris*, a rotational model of the specific pulsar, derived from long-term monitoring of the source with external facilities, most commonly radio telescopes.

Once sufficient exposure is accumulated, the rotational phases are used to construct a *phaseogram* (see Section 2.1.3 and Section 4.2.4), which displays the periodic modulation of the signal. A pulsar detection appears as recurrent peaks in this distribution.

A dedicated analysis pipeline for pulsars has been used for the data analysis, called `PulsarTimingAnalysis` (Mas and Morcuende, 2024).[4] At this stage, the workflow includes correcting event arrival times to recover the pulsar signal, and assigning rotational phases using the pulsar ephemeris. These tasks are performed by the `cphase` module, which internally relies on the `PINT` (Luo et al., 2019) library for barycentric corrections and phase computation. The resulting output, referred to as `DL3_pulsar`, is achieved by appending new columns to the event information, yielding modified DL3 files, and serves as the input for the high-level analysis.

Once the photon arrival times recorded in UTC are converted to SSB times and corrected for delays, each event must be assigned a rotational phase of the pulsar. In other words, we need to determine the exact point of the period of rotation of the star when the photon was emitted. This procedure, known as phase-folding, is one of the most delicate steps in pulsar analysis. If f is the pulsar frequency and $\dot{f}$, $\ddot{f}$ its derivatives, the phase of an event at SSB time t can be expressed as:

$$\phi = \phi_0 + f(t-t_0) + \frac{1}{2}\dot{f}(t-t_0)^2 + \frac{1}{6}\ddot{f}(t-t_0)^3 \tag{4.8}$$

where ϕ_0 is a reference phase, and t_0 is the epoch corresponding to this reference.

---

[4] More details can be found here: `https://github.com/cta-observatory/PulsarTimingAnalysis`.

Pulsar ephemeris

To compute phases with Eq. 4.8, the rotation parameters $(f, \dot{f}, \ddot{f})$ must be known. These are provided by a rotational model, or ephemeris, obtained from multiwavelength observations. Ephemeris include the source coordinates, spin frequency, frequency derivatives, and, in the case of binaries, orbital parameters. They also account for irregularities such as glitches. Since pulsars gradually spin down (see Section 2.1.1), the derivatives are essential.

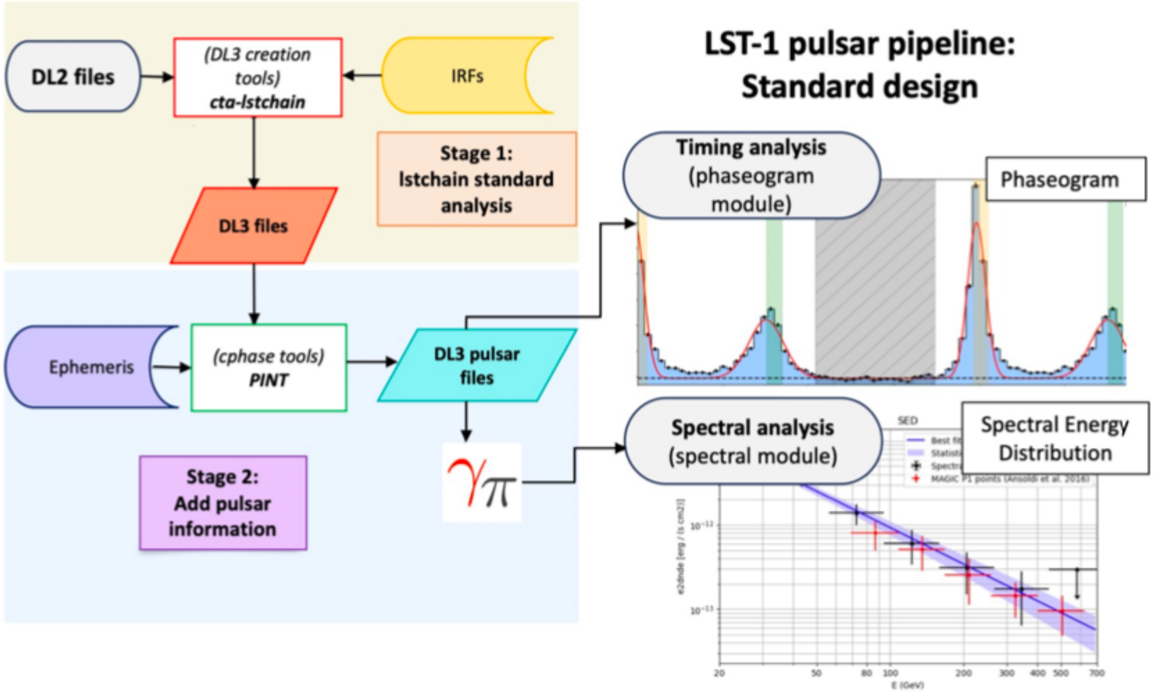

Figure 4.9: Scheme of the LST-1 pulsar analysis chain. The brown-shaded block represents the procedure to produce DL3 files through `lstchain`, which serve as the input for the pulsar analysis. The blue-shaded block represents the timing analysis performed with `PulsarTimingAnalysis`, which is carried out from the DL3 level and produces files in which each event is assigned a rotational phase of the pulsar. Then, the dataset is ready for high-level analysis which uses `PulsarTimingAnalysis` through `Gammapy` to produce phaseograms and SEDs.
Credit: Mas Aguilar, 2025.

In gamma-ray astronomy, ephemeris for many pulsars are available from the *Fermi*-LAT Third Pulsar Catalog (Smith et al., 2023). The ephemeris used in this work for the Crab pulsar were taken from the Jodrell Bank Observatory database,[5] which provides updated ephemeris

---

[5] `http://www.jb.man.ac.uk/~pulsar/crab.html`

since 1982 (Lyne, Pritchard, and Graham Smith, 1993). Because the pulsar rotation evolves, ephemeris are valid only within limited time intervals and must be updated periodically. In the case of the Crab pulsar, this update is required every month, and in this work the phase assignment was performed using the appropriate monthly ephemeris for each observation epoch over the 6-7 year dataset.

Once DL3 and DL3_pulsar are produced using `lstchain` and `PulsarTimingAnalysis`, the dataset is ready for the high-level analysis to extract final science products. Fig. 4.9 schematizes the LST-1 workflow: starting from DL3 files generated with `lstchain`, the `cphase`, `phaseogram` and `spectral` modules of `PulsarTimingAnalysis` are used to add the rotational phase, and build DL4 and DL5 files. The purpose of the high-level analysis (see Section 4.1.7) is to convert event lists into measurable quantities that can be directly compared with theoretical models or with results from other instruments. In this work, the main science outcomes are the phase-resolved spectra of the Crab pulsar, although phaseograms were also derived. Both are presented and discussed in Chapter 5.

4.2.4 Phaseograms

The distribution of rotational phases associated with detected events, namely a histogram of ϕ values (see Eq. 4.8 and Section 2.1.3) is referred to as the *phaseogram*. It is also known as the pulsar light curve or pulse profile, as it traces the variation of emission intensity over one pulsar rotation. The phaseogram is the primary diagnostic for identifying periodic pulsar signals, which are embedded in background noise and, in some cases, steady nebular gamma-ray emission, as for the Crab pulsar.

For a non-variable source, the phaseogram is flat along the phase. Conversely, the presence of a strong periodic component manifests as event excesses at specific phase intervals, superimposed on the uniform background. These pulsed excesses may vary in position or width with energy, offering insight into the emission mechanisms of pulsars (see Section 2.1.3). Gamma-ray pulsar phaseograms often show two peaks, shaped by the observer's viewing geometry. In some cases, a weaker emission between the peaks, commonly termed bridge emission, is visible. The relative peak intensities are highly energy-dependent, with the dominant feature at MeV energies possibly weakening or vanishing at GeV energies.

In this work, phaseograms of the Crab pulsar were obtained using the `phaseogram` module of `PulsarTimingAnalysis`, whose primary task is to automatically compute the phaseogram, model it, and extract the main statistics within the predefined pulsed signal regions specified in a configuration file. It provides user-oriented tools for both statistical extraction and result visualization. In addition to the phaseogram, the main outputs of the module are significance estimation (Li & Ma formula, see Eq. 4.3) for each predefined signal region, periodicity tests (χ^2, Z_n, H-test; see Section 4.1.7, and later), phaseogram fitting using maximum-likelihood and least-squares methods (J. R. Taylor, 1982), and time-dependent results, providing information on the evolution of the pulsed signal with observation time.

Periodicity tests

Statistical tests to quantify the periodicity are commonly employed in pulsar timing analyses to search for periodic signals, but in this work, the focus is placed on spectral analysis, and therefore these methods are only briefly mentioned here. Two types of tests are typically used:

1. Excess estimation: requires assuming a phaseogram shape (number, position, and width of peaks). The counts in the expected signal region are compared with counts in a background phase interval. The difference yields the excess events, and its significance is computed relative to background fluctuations, typically using the Li & Ma formula (Eq. 4.3).
2. Periodicity tests (χ^2, Z_n^2, H-test): assess deviations of the phase distribution from uniformity without assuming any emission profile. These are sensitive to any periodicity, regardless of peak number or shape.

The Crab pulsar shows two emission peaks in each rotation, P1 and P2, which remain aligned at all wavelengths. The phase regions adopted in this work are those defined in Aleksić et al. (2012), and summarized in Table 4.5

- P1 = [0, 0.026, 0.983, 1]. It is located at phase 0, and is the most intense in radio and *Fermi*-LAT data (Abe et al., 2024).
- P2 = [0.377, 0.422]. This peak is the most instense in the VHE regime (Abe et al., 2024, Ansoldi et al., 2016).
- Background (OFF region) = [0.52, 0.87], where no pulsed emission is expected.

Region	Interval
P1	[0, 0.026, 0.983, 1]
P2	[0.377, 0.422]
Background	[0.52, 0.87]

Table 4.5: Phase regions of the two emission peaks of the Crab pulsar P1 and P2 adopted in this work, defined by Aleksić et al. (2012).

The phaseogram was computed in the energy range between 20 GeV and 1 TeV, with 50 bins over the [0,1] interval. Event selection applied cuts on zenith distance such that runs with Zd $\leq$ 50 deg are retained. Phaseogram fitting was performed with a double Gaussian model. Time-resolved analysis was carried out with bins of 5 hours.

4.2.5 Spectral energy distributions (SEDs)

As described in Section 4.1.7, the SED is obtained from Eq. 4.5. LST-1 reconstructs the SED using the forward-folding approach, where an assumed spectral model is convolved with the IRFs and fit to the observed data.

The adopted model in this work is a power law of the form

$$\frac{d\phi}{dE} = \phi_0 \left(\frac{E}{E_0} \right)^{-\Gamma} \tag{4.9}$$

where E_0 is the reference energy, ϕ_0 is the flux at that reference energy, and Γ is the spectral index.

SEDs are computed using the `spectral` module of `PulsarTimingAnalysis`, which is built based on `Gammapy`. Its purpose is to process the data into DL4 files, extract spectra for each pulsar emission peak, and model the gamma-ray emission. The workflow is automated through an external configuration file in which the user specifies the analysis parameters (model, fit energy range, geometry, number of spectral points, etc.), and the main function executes the procedure without requiring direct use of `Gammapy` internals. The most relevant outputs are the SEDs, the best-fit parameters, and flux points.

In this work, the spectral analysis was carried out in the energy range 20 GeV - 1 TeV. The true-energy geometry was defined between 3 GeV and 50 TeV with 100 bins, while the reconstructed-energy geometry covered 20 GeV - 1 TeV with 60 bins. Flux points were extracted in six energy bins across the 20 GeV - 1 TeV interval, with a minimum test statistic threshold of 1.5σ. Event selection applied a zenith distance cut of Zd $\leq$ 50 deg. These settings allowed us to derive phase-resolved spectra for each pulsed emission region, P1 and P2, defined in the previous Section 4.2.4 and summarized in Table 4.5.

5. Results and discussion

Chapter 4 detailed the full LST-1 pulsar analysis chain, from raw data to the production of DL3 and DL3_pulsar datasets, and the production of final science products such as phaseograms and phase-resolved spectral energy distributions (SEDs).

In this Chapter, the scientific results obtained by applying that pipeline to the Crab pulsar observations collected since LST-1 has become operational, from October 2018 to July 2025, are presented. Two high-level products have been derived: the phaseogram and the SED of both emission peaks P1 and P2 (see Section 4.2.4 and 4.2.5, respectively). The discussion is focused on the SEDs, although the phaseogram is also presented and discussed here.

5.1 Phaseogram

The phaseogram computed in an energy range between 20 GeV and 1 TeV, for a total observation time of about 180 hours, is shown in Fig. 5.1. The yellow band defines the region of the first peak P1 [0, 0.026, 0.983, 1], while the green band defines the region of the second one P2 [0.377, 0.422], as summarized in Table 4.5. The gray band refers to the background, or OFF region, where no emission appears [0.52, 0.87].

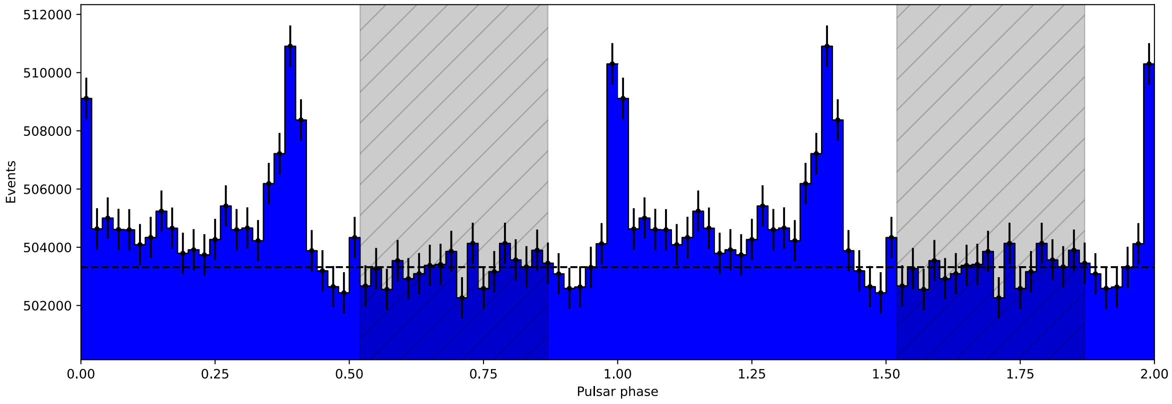

Figure 5.1: Phaseogram of the Crab pulsar from LST-1 data, for a total observation time of about 180 hours. The first peak P1 is defined by the yellow region, while the second peak P2 is defined by the green region. It is also indicated the background region, defined by the gray band. The graph shows two phases for better visualization.

The significance of the gamma-ray signal with respect to the background was computed using Li and Ma (1983) formula (Eq. 4.3), and summarized in Table 5.1. The first peak P1 was detected with a significance of 11.47σ, while the second one P2 with a significance of 11.96σ. It was also computed the significance of the joint pulsed emission P1+P2, resulting to be 15.72σ.

Region	Significance
P1	11.47σ
P2	11.96σ
P1+P2	15.72σ

Table 5.1: Statistical significance of the pulsed emission from the Crab pulsar derived with the Li & Ma formula (Eq. 4.3). Values are reported for the individual peaks P1 and P2, as well as for their combined emission P1+P2.

The significance of the pulsed emission was also tested with three periodicity tests (see Section 4.2.4): χ^2, H-test, and Z_n^2, resulting in 14.25σ, 15.11σ, and 15.70σ, respectively. All of them do not assume any peak position or shape.

Time-resolved analysis

Time-resolved analysis was carried out with bins of 5 hours. The significances for P1, P2, and P1+P2 over the observation time are shown in Fig. 5.2. They follow a trend $\propto \sqrt{t}$ (dashed line), where t is the observation time, reflecting the Poissonian statistics of events. This profile ensures the stability of the analyzed dataset and the performance of LST-1.

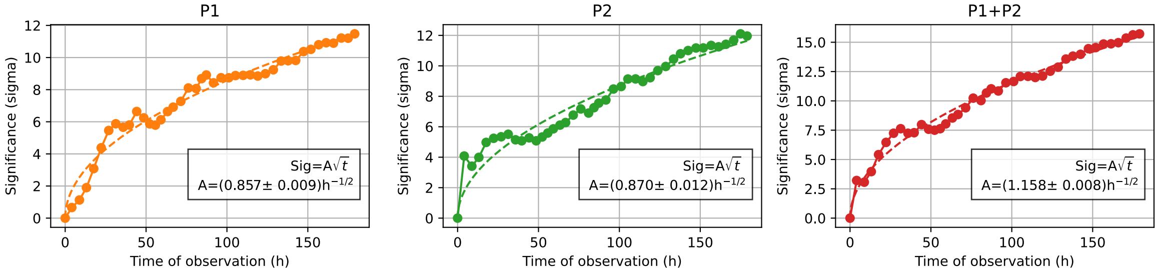

Figure 5.2: Evolution of the detection significance for the Crab pulsar peaks P1, P2, and their combined emission P1+P2 as a function of observation time. The dashed lines show the expected $\propto \sqrt{t}$ dependence, where t is the total observation time.

Fig. 5.3 shows instead the number of excess events as a function of observation time. The excesses are computed with Eq. 4.1 (see Section 4.1.7). As expected (Li and Ma, 1983), they follow a linear trend with time.

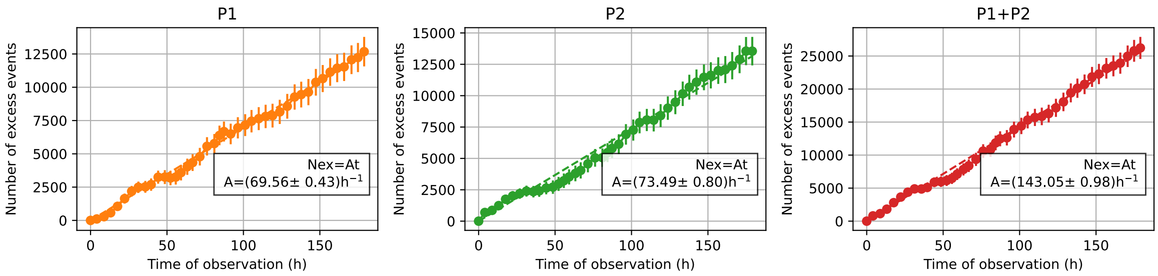

Figure 5.3: Number of excess events from the Crab pulsar as a function of observation time. The excess shows the expected linear dependence on time.

Abe et al. (2024) reported significances of 10.5σ, 12.1σ, and 15.2σ for P1, P2, and P1+P2, respectively, using a reduced dataset corresponding to about 103 hours of observations. In this work, the values obtained for P1 and P1+P2 are higher, confirming that the significance improves as the dataset, and hence the total observation time, increases. However, the value found for P2 is slightly lower. This may be explained through a closer inspection of the significance time trends over observation time shown in Fig. 2 of Abe et al. (2024). The cumulative significance at the endpoint ($\sim$103 hours) sits above the best-fit curve, so it benefits from a positive fluctuation with respect to the expected trend. In the dataset analyzed in this work, instead, the cumulative points closely follow the fit up to $\sim$180 hours (see Fig. 5.2). As a result, the improvement of the overall significance relative to theirs is smaller than one would expect from exposure alone.

P1/P2 ratio

Short-term deviations around the $\sqrt{t}$ trend are common due to run-to-run variations in background and observing conditions, so comparing only the final points can be misleading. As a consequence, to ensure consistency with their results, the P1/P2 ratio has been obtained.[1] Its value resulted to be 0.94 ± 0.11, in agreement with theirs (P1/P2 = 0.84 ± 0.11).

---

[1] P1/P2 ratio has been computed using the following formula: $P1/P2 = \frac{\int_{E_{min}}^{E_{max}} E\phi_{P1}\left(\frac{E}{E_0}\right)^{-\Gamma_{P1}} dE}{\int_{E_{min}}^{E_{max}} E\phi_{P2}\left(\frac{E}{E_0}\right)^{-\Gamma_{P2}} dE}$, where E is the energy, ϕ is the flux at the reference energy E_0, and Γ is the spectral index of the power-law.

These results therefore provide a confirmation of previous LST-1 results, but with a longer dataset extending to mid-2025, resulting in ~ 80 hours of observation time more, and a larger energy range up to 1 TeV.

5.2 Spectral energy distributions (SEDs) of the peaks

As introduced in Section 4.2.5, the SEDs of the peaks P1 and P2 of the Crab pulsar, whose regions are defined in Table 4.5, are obtained in the energy range 20 GeV - 1 TeV.

Compared to previous LST-1 studies (Abe et al., 2024), which were limited to 700 GeV, the results presented here benefit from the larger dataset available (extending up to mid-2025), thus a longer total observation time. This provides the opportunity to extend the spectral analysis at the highest energies accessible to the instrument.

In this work, the adopted model is a power law of the form of Eq. 4.9, also reported in the following equation:

$$\frac{d\phi}{dE} = \phi_0 \left(\frac{E}{E_0}\right)^{-\Gamma} \tag{5.1}$$

where E_0 is the reference energy, ϕ_0 is the flux at that reference energy, and Γ is the spectral index. The adopted model reflects the fact that, unlike the majority of gamma-ray pulsars observed with *Fermi*-LAT that exhibit exponential spectral cutoffs around a few GeV (see Section 2.2.1), the Crab pulsar is one of the very few cases where the spectrum extends well into the TeV domain without evidence of such a cutoff. This peculiar behavior, presented in Section 2.2.2, is consistent with the detection of a hard component up to VHE.

The phase-resolved SEDs of peaks P1 and P2, together with their best-fit power-law models with theirs associated statistical uncertainty obtained by error propagation, are reported in Fig. 5.4. It is shown that six flux points are derived in six energy bins with 1σ statistical uncertainties. The obtained spectral points are reported in Table 5.2, while the corresponding fit parameters are summarized in Table 5.3. Seed parameters for the fitting procedure were set based on Table 3 of Abe et al. (2024). In the fit, ϕ_0 and Γ are treated as free parameters, whereas the reference energy E_0 is kept fixed. The spectral index of P2, $\Gamma_{P2} = 2.80 \pm 0.07$, is harder than the one for P1, $\Gamma_{P1} = 3.0 \pm 0.1$, and the flux of P2 is larger than the flux of P1 over all the energies.

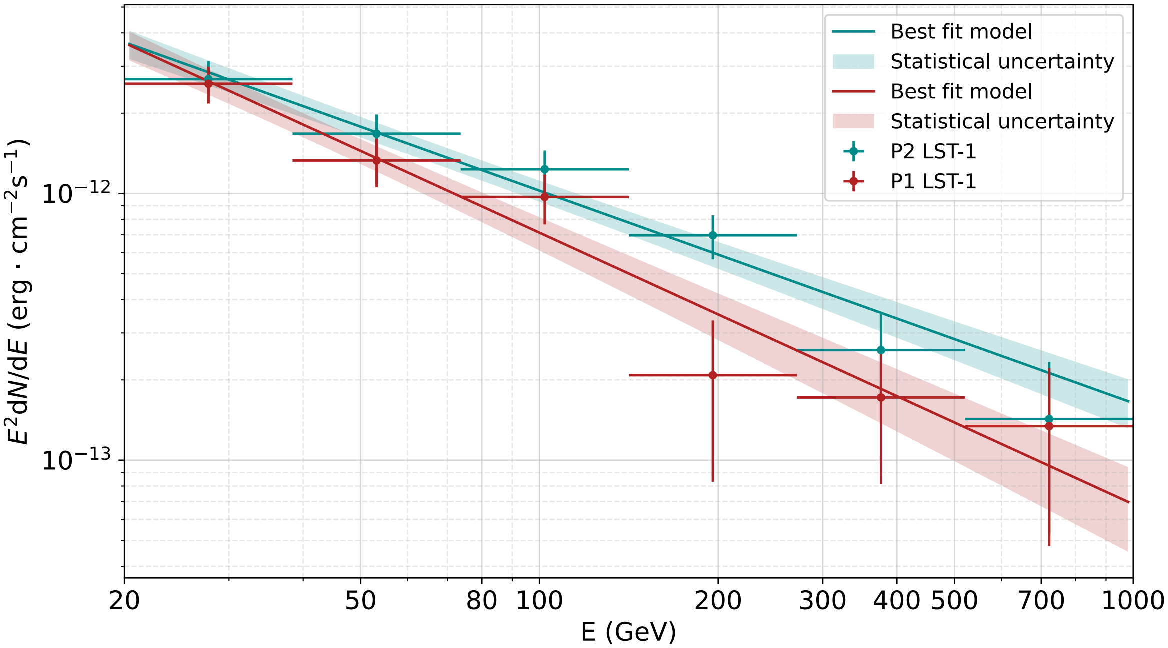

Figure 5.4: Phase-resolved SEDs of the Crab pulsar peaks P1 (red) and P2 (cyan) obtained with LST-1 data between 20 GeV and 1 TeV. The flux points are derived in six energy bins with 1σ statistical uncertainties, the solid lines represent the best-fit power-law models with their the statistical uncertainty band (derived by error propagation). The spectral points are summarized in Table 5.2, while the fit parameters are reported in Table 5.3.

Energy (GeV)	Bin center (GeV)	P1 (erg s^{-1}cm^{-2}) $\times 10^{-13}$	P2 (erg s^{-1}cm^{-2}) $\times 10^{-13}$
20 - 38	27.7	25.8 ± 4.0	26.8 ± 4.5
38 - 74	53.2	13.3 ± 2.7	16.7 ± 3.0
74 - 141	102.1	9.7 ± 2.0	12.3 ± 2.2
141 - 271	195.9	2.1 ± 1.2	7.0 ± 1.3
271 - 521	376.1	1.7 ± 0.9	2.6 ± 0.9
521 - 1000	721.8	1.3 ± 0.9	1.4 ± 0.9

Table 5.2: Spectral points of the Crab pulsar peaks P1 and P2 obtained with LST-1 data between 20 GeV and 1 TeV. The table reports the energy bin, the bin center, and the fluxes expressed as $E^2 dN/dEdAdt$ with 1σ statistical uncertainties.

Region	E_0 (GeV)	ϕ_0 ($\mathrm{cm^{-2}s^{-1}TeV^{-1}}$)	Γ
P1	30	$1.7 \pm 0.2 \times 10^{-9}$	3.0 ± 0.1
P2	40	$8.3 \pm 0.7 \times 10^{-10}$	2.80 ± 0.07

Table 5.3: Best-fit power-law parameters of the phase-resolved SEDs of the Crab pulsar peaks P1 and P2 from 20 GeV to 1 TeV. The table reports the reference energy E_0, the normalization ϕ_0, and the spectral index Γ, derived from the likelihood fit of LST-1 data.

A comparison with the SEDs presented by Abe et al. (2024) indicates a discrepancy: their spectral indices for P1 and P2 are $\Gamma_{P1} = 3.44 \pm 0.15$ and $\Gamma_{P2} = 3.03 \pm 0.09$. This is probably due to the difference at lower energies (below $\sim$ 50 GeV), as shown in Fig. 5.5 for P1 and in Fig. 5.6 for P2, in which the spectral points and the best-fit curve with uncertainties obtained in this work are directly compared to theirs.

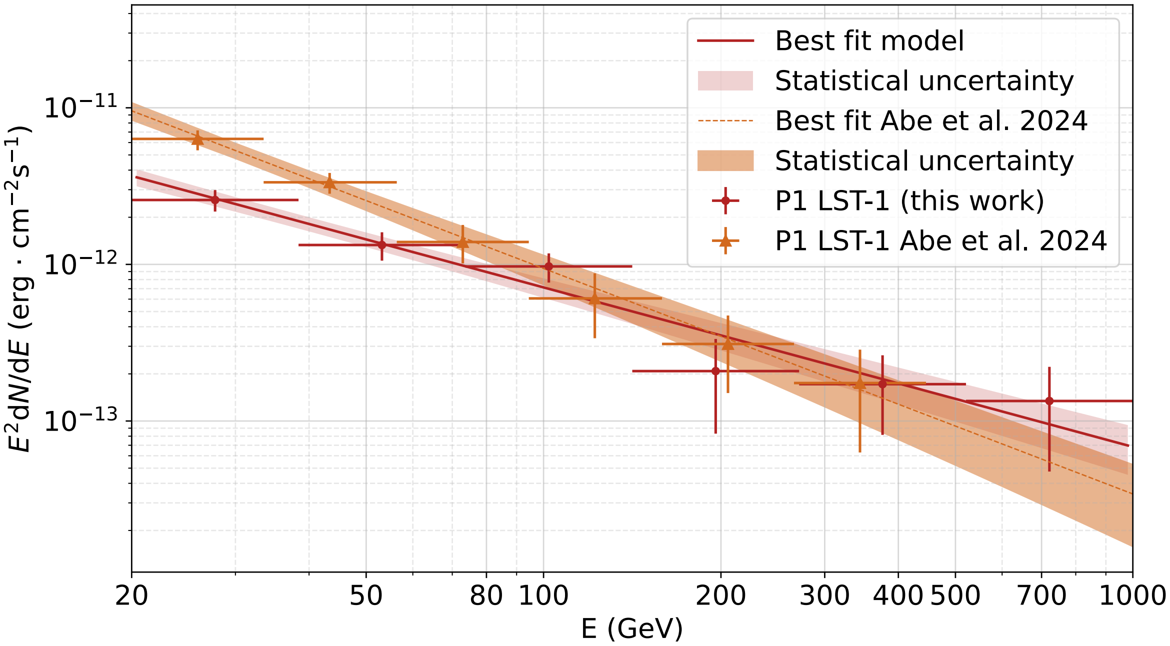

Figure 5.5: Comparison of the SED of peak P1 obtained in this work (red) with the SED reported by Abe et al. (2024) (orange), with their associated statistical uncertainties. The result of this work includes one additional spectral point at higher energies, extending the analysis up to 1 TeV, beyond the last significant bin of the earlier LST-1 results. The discrepancy below ~50 GeV is discussed in the text.

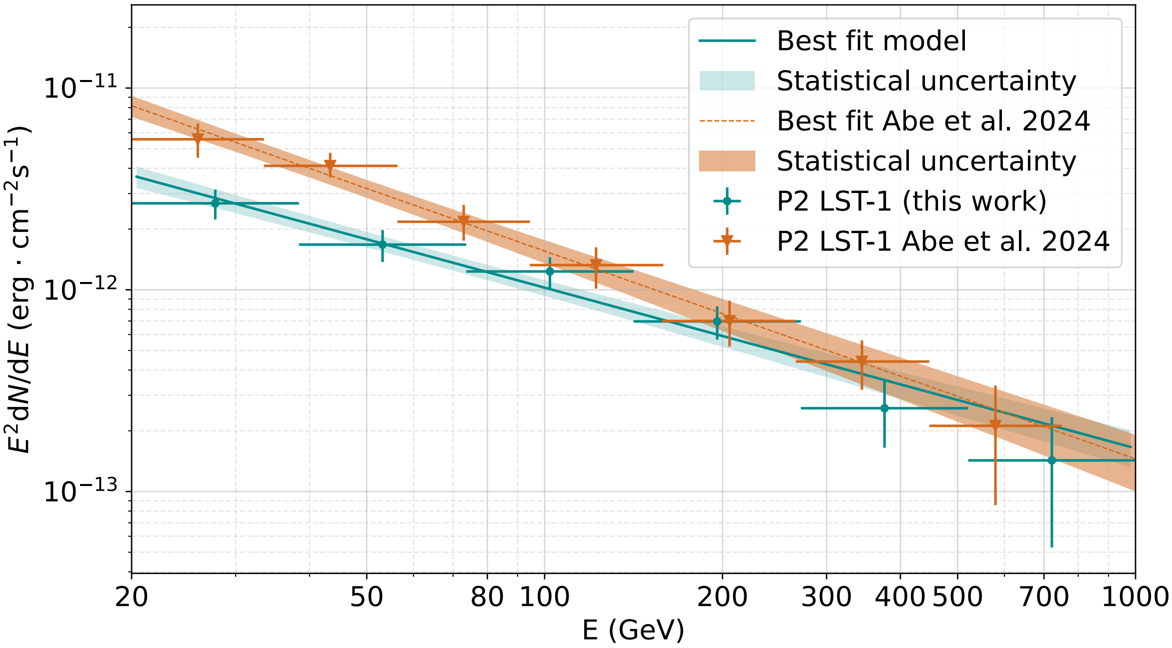

Figure 5.6: Comparison of the SED of peak P2 obtained in this work (cyan) with the results reported by Abe et al. (2024) (orange), with their associated statistical uncertainties. The result of this work includes one additional spectral point at higher energies, extending the analysis up to 1 TeV, beyond the last significant bin of the earlier LST-1 results. The discrepancy below ∼50 GeV is discussed in the text.

The difference observed in Fig. 5.5 and Fig. 5.6 below ∼50 GeV can be related to data analysis choices and threshold-regime systematics. Abe et al. (2024) applied intensity cuts (80 p.e. before August 2021 and 50 p.e. thereafter) together with cut selections on α and Gammaness tuned to a 70% MC efficiency per energy bin (see Section 4.1.5), which alters the acceptance in the first reconstructed-energy bins where images are faint and energy dispersion is largest. In this work, instead, standard cuts of intensity ≥ 70 p.e., Gammaness ≥ 0.7, and $\theta \leq 0.7$ deg were adopted (Table 4.4). In addition, their source-dependent analysis and IRFs derived from all-sky MC productions (tuned to the local NSB) imply different dispersion and systematics: they report reconstructed energies being systematically higher than true energies at the lowest energies, near the energy threshold, and quantify systematic uncertainties on the spectral indices (∼0.34 for P1 and ∼0.21 for P2) and on the flux normalizations (up to ∼45% for P1 and ∼20% for P2). Differences in software versions and in the run selection (see Section 4.1.2) may further contribute to a mismatch confined to 20-50 GeV. Above 50 GeV, where the instrument response is more stable and migration effects are reduced (see Section

4.1.6), the agreement becomes evident. Moreover, the present analysis benefits from a larger dataset, i.e. a larger total observation time (about 80 hours more), improving the statistical precision at higher energies. Although the statistical uncertainties increase toward the TeV domain, the results remain consistent between the two analyses, indicating that the observed difference is specific to the threshold-dominated regime rather than to the high-energy tail of the spectrum. Furthermore, the present analysis provides an additional spectral point for both P1 and P2 at higher energies, extending the reconstruction up to 1 TeV, beyond the last significant bin reported in Abe et al. (2024).

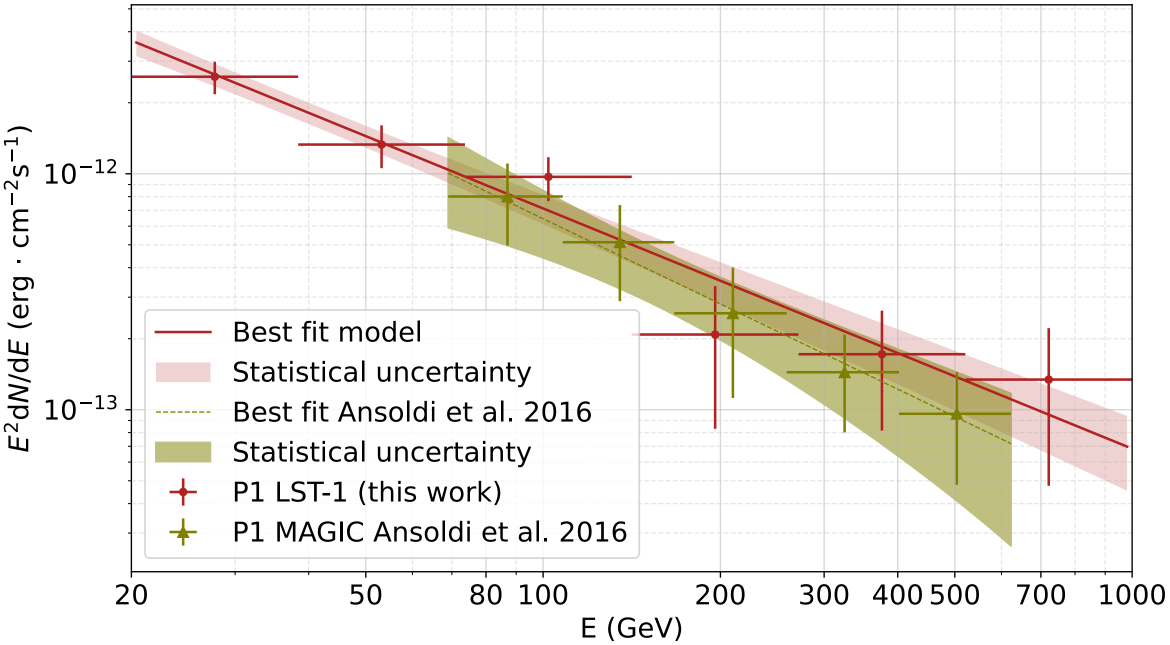

Figure 5.7: Comparison of the SED of peak P1 obtained in this work (red) with the results reported by Ansoldi et al. (2016) (green), with their associated statistical uncertainties. The result of this work includes additional spectral points at lower energies, thanks to the improved threshold of LST-1, and one additional spectral point at higher energies, extending the analysis up to 1 TeV beyond the last significant bin of the MAGIC analysis.

A comparison with the results obtained by Ansoldi et al. (2016) provides additional context and is reported in Fig. 5.7 and Fig. 5.8. They analyzed a dataset of about 320 hours collected between 2007 and 2014 with the two MAGIC telescopes in stereo mode, achieving phase-resolved spectra of the Crab pulsar up to 1.5 TeV. Their analysis yielded spectral indices of $\Gamma_{P1} = 3.2 \pm 0.4$ and $\Gamma_{P2} = 2.9 \pm 0.2$, both normalized at 150 GeV. These values are consistent within uncertainties with those obtained in the present work (see Table 5.3).

For P2 (Fig. 5.8), MAGIC found the emission up to 1.5 TeV, whereas the present analysis confirms the compatibility of the spectrum up to 1 TeV. For P1 (Fig. 5.7), instead, MAGIC reported significant flux points only up to about 600 GeV, while the present work extends the reconstruction up to 1 TeV, providing one additional spectral point beyond those obtained with MAGIC. This strengthens the evidence that both pulsar peaks can be described by power laws without indication of an exponential cutoff up to the TeV domain. Moreover, thanks to the improved energy threshold of LST-1, the present results also provide additional spectral points at lower energies that were not accessible to MAGIC, further extending the overall spectral coverage.

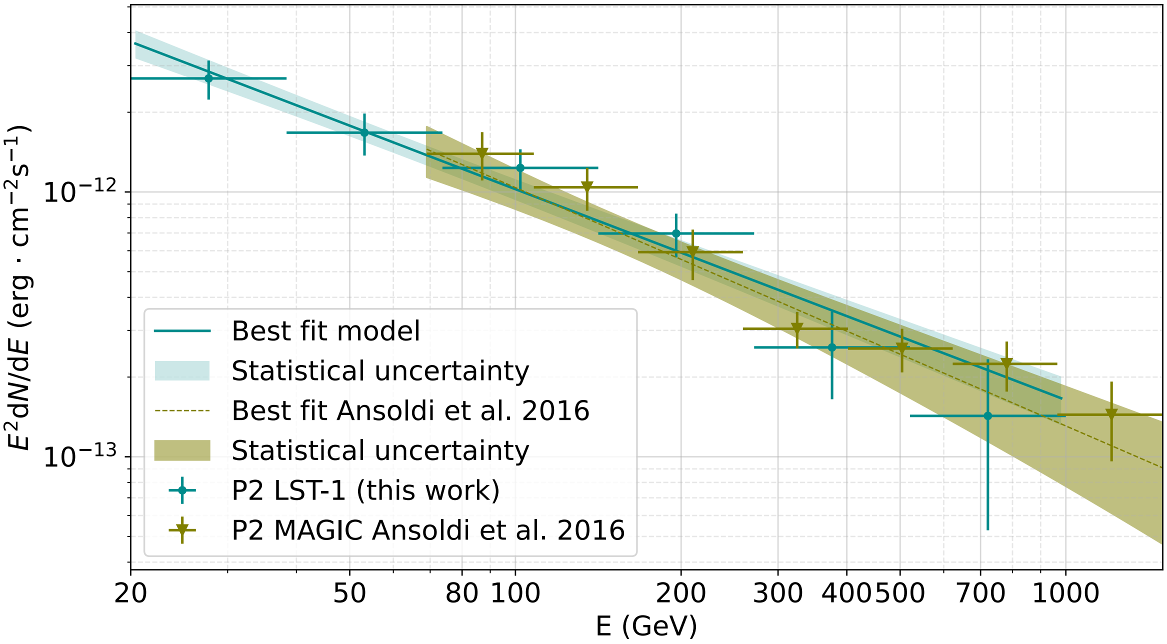

Figure 5.8: Comparison of the SED of peak P2 obtained in this work (cyan) with the results reported by Ansoldi et al. (2016) (green), with their associated statistical uncertainties. The result of this work includes additional spectral points at lower energies, thanks to the improved threshold of LST-1, and confirms the compatibility of the spectrum with MAGIC results up to 1 TeV.

Finally, for completeness, Fig. 5.9 and Fig. 5.10 provide a direct comparison of the spectral points only for peaks P1 and P2, respectively. These summary plots combine the results obtained in this work (red for P1 and cyan for P2) with those reported by Ansoldi et al. (2016) (green) and Abe et al. (2024) (orange), allowing a straightforward visual inspection of the agreement among independent analyses. For P1 (Fig. 5.9), the present work extends the analysis up to ∼1 TeV with respect to previous LST-1 and MAGIC results (Abe et al., 2024, Ansoldi et al., 2016), while for P2 (Fig. 5.10) the analysis is extended up to 1 TeV with respect to LST-1, and demonstrates compatibility with MAGIC results.

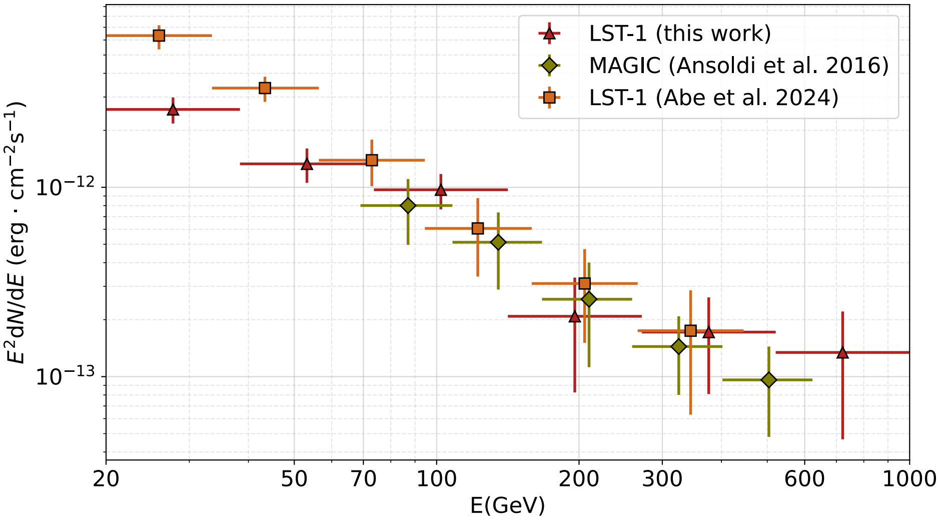

Figure 5.9: Summary plot of the spectral points for peak P1 from this work (red), MAGIC (Ansoldi, Antonelli, Antoranz, et al., 2016) (green), and LST-1 (Abe et al., 2024) (orange). The present analysis provides one additional point up to ∼1 TeV.

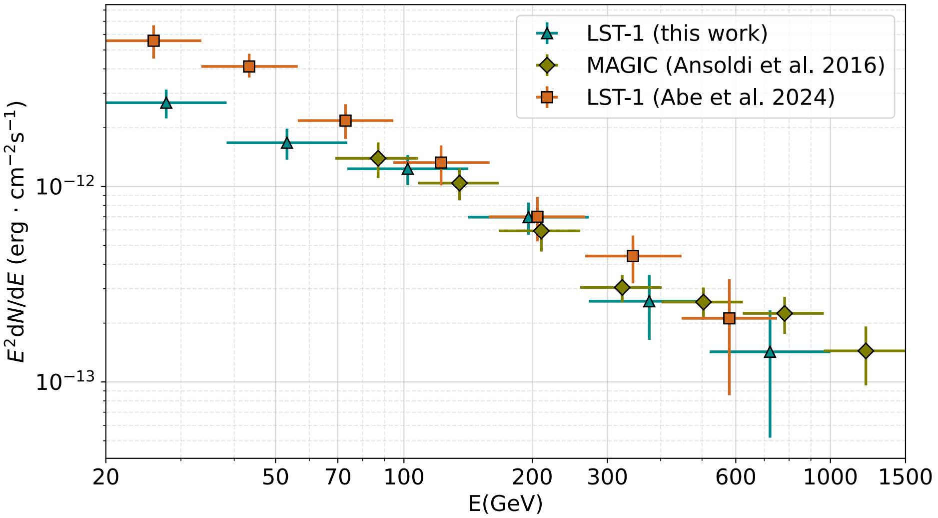

Figure 5.10: Summary plot of the spectral points for peak P2 from this work (cyan), MAGIC (Ansoldi, Antonelli, Antoranz, et al., 2016) (green), and LST-1 (Abe et al., 2024) (orange). The present analysis provides one additional point up to 1 TeV with respect to LST-1, and demonstrate compatibility with MAGIC results.

5.3 Future prospects

The phase-resolved spectra up to ~ 1 TeV reported here strengthen the case for emission mechanisms beyond classical models (polar cap, outer gap, slot gap; see Section 2.3.1). In particular, the persistence of a hard component at VHE suggests IC processes in outer magnetospheric regions or in the current sheet (see Section 2.2.2).

A future step is to test whether the theoretical frameworks recently invoked for the Vela pulsar, which has been detected with H.E.S.S. up to ~ 20 TeV (H. E. S. S. Collaboration, F. Aharonian, et al., 2023), as described in Section 2.3.2, are compatible with the Crab results presented here. In Vela, a separate multi-TeV component from the GeV cutoff has been interpreted in terms of IC scattering of optical-to-infrared photons in the Klein-Nishina regime at VHE. The requirement of Lorentz factors $\gamma \geq 7 \times 10^7$ (H. E. S. S. Collaboration, F. Aharonian, et al., 2023) is in line with scenarios involving acceleration beyond the LC, either along extended field lines or through reconnection in the striped wind current sheet. Comparing the Crab pulsar with the multi-TeV behavior of Vela offers a decisive probe for discriminating between CR/IC and SR/IC models (see Section 2.3.2 and A). Establishing whether the Crab emission can be consistently reproduced within the same frameworks proposed for Vela will be an important test for our theoretical understanding of pulsar emission in the VHE regime.

Conclusions

Gamma-ray astronomy explores the highest-energy part of the electromagnetic spectrum (> 100 keV), dominated by non-thermal processes where particles are accelerated up to relativistic energies. The energy domain is usually subdivided into bands; this thesis concentrates on the VHE regime, spanning 100 GeV to 100 TeV. This field provides a means to investigate the origin of cosmic rays, to study extreme astrophysical conditions in extragalactic and Galactic sources, including pulsars.

Pulsars are among the most significant gamma-ray emitters. These rapidly spinning, strongly magnetized neutron stars generate environments where particles are accelerated to ultra-relativistic energies, producing pulsed radiation that extends from radio frequencies up to gamma rays.

Classical theoretical models such as the polar cap, the outer gap, and the slot gap models place the origin of gamma-ray emission within the pulsar magnetosphere. All of them predict an exponential cutoff, consistent with *Fermi*-LAT observations. However, IACTs unexpectedly detected pulsar emission extending into the VHE band from only two pulsars: the Crab pulsar up to 1.5 TeV, the focus of this thesis, and the Vela pulsar up to 20 TeV. Such detections challenge traditional models and motivate alternative mechanisms. New proposed scenarios for VHE emission include the modified outer gap model, the wind-zone model, and the current-sheet model.

With LST-1 already operational, new opportunities to probe pulsed emission from pulsars in the VHE domain arise, providing the main motivation for this thesis.

The goal of this work was indeed to measure pulsed VHE emission from the Crab pulsar up to 1 TeV using all the available LST-1 dataset so far, employing advanced analysis techniques to produce phase-resolved spectra. The analysis employed the standard LST-1 pipeline, including raw data calibration, image cleaning, event reconstruction, and gamma/hadron separation using Random Forest classifiers trained on Monte Carlo simulations, leading to DL3 datasets with instrument response functions. Pulsar analysis was carried out with a dedicated timing package, which performs barycentric corrections and rotational phase assignments using updated ephemerides. Final scientific products such as phaseograms and phase-resolved spectra were then derived, enabling flux extraction between 20 GeV and 1 TeV for P1 and P2. This aimed to extend earlier results obtained with MAGIC and LST-1

(Ansoldi et al., 2016; Abe et al., 2024), which reported emission up to 450 GeV for P1 and 700 GeV for P2 with LST-1, and 600 GeV for P2 with MAGIC.

The analysis of the overall dataset, from October 2018 to July 2025, resulted in about 180 hours of observation time, 80 hours more than Abe et al. (2024). The produced phaseogram computed in an energy range from 20 GeV to 1 TeV, extended with their phaseogram computed between 20 GeV and 700 GeV, provides the detection of both peaks P1 and P2 with a significance of 11.47σ and 11.96σ, respectively. The combined significance of P1+P2 resulted to be 15.72σ. The results for P1 and P1+P2 are higher than those reported in Abe et al. (2024), confirming that the significance increases with the increase of the total observation time. The value for P2, instead, is slightly lower than expected. This can be explained by the fact that in the earlier dataset the cumulative significance over the total observation time $t \sim$100 hours benefited from a positive fluctuation, whereas in the present analysis the values closely follow the expected $\sqrt{t}$ trend up to 180 hours. Since short-term deviations from this trend are common due to variations in background and observing conditions, the P1/P2 flux ratio was also computed to ensure consistency. The resulting value, 0.94 ± 0.11, is in good agreement with their reported 0.84 ± 0.11.

The second and most important science products obtained in this work are the phase-resolved SEDs of the Crab pulsar peaks P1 and P2 in the 20 GeV - 1 TeV energy range. The spectral points have been fitted using a simple power law since the spectrum of the Crab pulsar extends into the TeV domain (up to 1.5 TeV) without clear evidence of a cutoff (Ansoldi et al., 2016). The spectral indices resulted from the fit are the following: $\Gamma_{P1} = 3.0 \pm 0.1$ for P1 and $\Gamma_{P2} = 2.80 \pm 0.07$ for P2. These are in agreement with Ansoldi et al. (2016), in which they analyzed 320 hours of data collected by the MAGIC telescopes. There is instead a discrepancy with the spectral indices reported by Abe et al. (2024), in which they analyzed LST-1 data. This may originate from the difference in the 20 - 50 GeV range between the spectra obtained in this work and their spectra. Near the energy threshold of the telescope ($\approx$ 20 GeV), data analysis choices and systematic errors play an important role. Moreover, differences in the software versions or in the applied cuts and in the data quality selection may contribute to the mismatch. However, the aim of this work is to constrain the emission at higher energies, and above $\sim$ 50 GeV, where the IRF of the telescope is more stable and migration effects are reduced, the two spectra show good agreement.

The SEDs for P1 and P2 of the Crab pulsar obtained in this work highlight two main results:

- One additional spectral point for the first peak P1 was obtained, up to 1 TeV, extending the analysis of previous studies with MAGIC and LST-1 (Ansoldi et al., 2016; Abe et al., 2024), in which they reported pulsed emission up to ∼600 GeV and ∼350 GeV, respectively.
- One additional spectral point for the second peak P2 was obtained, up to 1 TeV, extending the analysis of previous studies with LST-1 (Abe et al., 2024), which reported the emission up to 700 GeV, and confirming consistency up to 1 TeV with MAGIC previous results (Ansoldi et al., 2016).

Both results confirm that:

- Increasing the dataset, thus the total observation time, the chances to detect the emission at higher energies increase.
- Crab pulsar emission is described by a power law without a clear evidence of a cutoff up to TeV domain.
- There are strong prospects for future detections of the Crab pulsar and for other gamma-ray pulsars.

Regarding the last point, it is worth noticing that these results were achieved with LST-1 operating in mono mode. Future observations with four LSTs and, eventually, the full CTAO open the possibility of detecting emission from other known or candidate pulsars, broadening the accessible source population and enabling more detailed physical interpretation.

An important next step will be to test whether the Crab pulsar emission in the TeV domain can be consistently reproduced within the theoretical models recently proposed for the Vela pulsar (H. E. S. S. Collaboration, F. Aharonian, et al., 2023), providing a decisive step toward a deeper understanding of pulsar emission mechanisms in the VHE regime.

"E so
Che non è una fantasia
Non è stata una follia
Quella stella
La vedi anche tu
Perciò
Io la seguo ed adesso so
Che io la raggiungerò
Perché al mondo
Ci sono anch'io."
Max Pezzali, ne *Il Pianeta Del Tesoro*.

A. Radiative processes

Production of gamma rays due to leptonic acceleration is given by the following radiative processes. A detailed review can be found in Rybicki and Lightman (1979), where all the information provided here comes from.

Synchrotron radiation

Synchrotron radiation (SR) is a prevalent source of non-thermal emission, spanning a broad energy range. It originates from the acceleration of leptons in magnetic fields, as they spiral along field lines with a constant pitch angle α. For a lepton with Lorentz factor γ moving in a magnetic field $\vec{B}$, the total energy loss is given by:

$$-\frac{dE}{dt} = \frac{2\sigma_T c}{2\mu_0} B^2 \gamma^2 \sin(\alpha)^2 \tag{A.1}$$

The spectral distribution of SR is described by:

$$I(\nu) = \frac{\sqrt{3} e^3 B \sin(\alpha)}{4\pi\varepsilon_0 c m_e} F(\nu/\nu_c) \tag{A.2}$$

where

$$F(x) = x \int_x^{\infty} K_{5/3}(z) dz \tag{A.3}$$

Here, $K_{5/3}$ denotes the modified Bessel function of order 5/3, while ω_c is called the synchrotron critical frequency. In the ultra-relativistic limit, ω_c scales with the non-relativistic gyrofrequency ν_g:

$$\nu_c = \frac{3}{2} \gamma^2 \nu_g \sin(\alpha) \tag{A.4}$$

The function $F(\nu/\nu_c)$, illustrated in Fig. A.1, peaks at $\nu = 0.29\nu_c$. This peak corresponds to a spectral maximum at an energy E_{max}, proportional to both the magnetic field strength and the particle energy:

$$E_{max} = h\nu_{max} = 0.29h\nu_c \approx 5 \times 10^{-4} B(T)\gamma^2 \sin\alpha \;\; [\text{eV}] \tag{A.5}$$

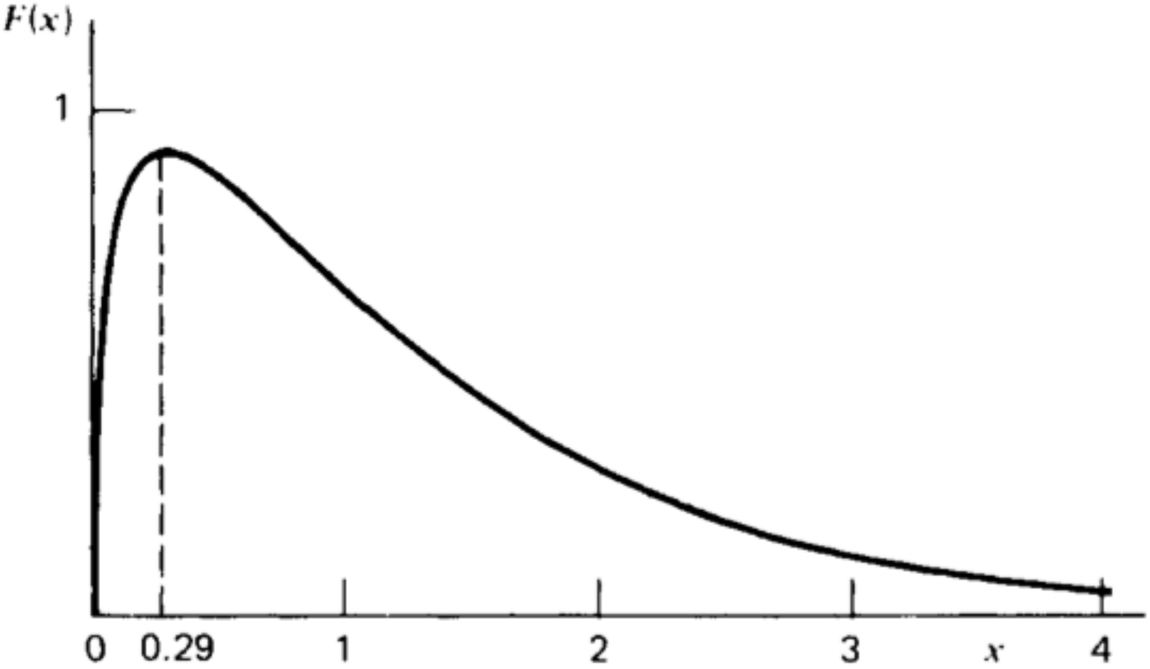

Figure A.1: Function F(x) as a function of x= ν/ν_c, showing a maximum at x=0.29. It describes the normalized spectral distribution of synchrotron radiation.
Credit: Rybicki and Lightman, 1979.

For an electron population with a power law energy distribution $N \propto E^{-\Gamma}$, the resulting photon spectrum also follows a power law, with spectral index $\Gamma' = \frac{\Gamma+1}{2}$.

Curvature radiation

Similar to SR, curvature radiation (CR) is significant for interpreting gamma-ray emission from pulsars. It arises when relativistic charged particles propagate along curved magnetic field lines. When the field-line curvature radius R_c exceeds the particle gyroradius, radiation is produced due to the transverse acceleration required to follow the curved trajectory. The formalism is similar to the synchrotron case, replacing the gyroradius with r_c. In this framework, Eq. A.1 and Eq. A.4 are modified, leading to the following expressions for energy losses and critical frequency:

$$-\frac{dE}{dt} = \frac{2\sigma_T c^3}{2\mu_0 r_c^2 e^2} B^2 \gamma^4 m_e^2 \sin^2(\alpha) \tag{A.6}$$

$$\nu_{c,curv} = \frac{3}{2}\frac{\gamma^3 c}{2\pi r_c} \tag{A.7}$$

For an electron population with a power-law distribution, the curvature radiation spectrum has an index $\Gamma' = \frac{\Gamma - 2}{3}$, distinct from the synchrotron case.

In realistic conditions, both processes act together in the so-called synchro-curvature radiation (SCR), whose gamma-ray spectrum generally deviates from a single power-law shape. Additional contributions from Compton or inverse Compton scattering may be included, yielding synchro-curvature self-Compton (SCSC).

Inverse Compton scattering

Inverse Compton (IC) scattering occurs when a relativistic electron or positron transfers part of its kinetic energy to a photon through scattering, boosting the photon to higher energies (see Fig. A.2). Gamma-ray production requires the initial lepton population to be relativistic. Two scattering regimes are distinguished:

- Thomson regime, in which $\gamma\hbar\omega << m_e c^2$ (photon energy in the electron rest frame is much smaller than the electron rest mass: the flux rises with frequency at low energies and declines sharply beyond a characteristic cutoff. For head-on interactions, the maximum photon energy is $E_{max} \approx 4\gamma^2 E_0$, where E_0 is the mean original photon energy. The mean scattered photon energy is $E_\gamma \approx \frac{4}{3}\gamma^2 E_0$, and the energy loss rate is given by

$$\frac{dE}{dt} = \frac{4}{3}\sigma_T c U_r \left(\frac{v}{c}\gamma\right)^2 \tag{A.8}$$

If the parent electron population follows a power-law energy distribution with spectral index Γ, the IC spectrum will also follow a power law with $\Gamma' = \frac{\Gamma+1}{2}$, identical to the synchrotron case.

- Klein-Nishina regime, in which $\gamma\hbar\omega >> m_e c^2$ (photon energy in the electron rest frame is comparable to or exceeds the electron rest mass): scattering becomes inelastic, and the cross section depends strongly on energy. However, in this regime the cross section is significantly lower than in the Thomson case, which suppresses the IC emission. Here, $E_{max} \approx \gamma m_e c^2$, and the mean gamma-ray energy is $E_\gamma \approx \frac{1}{2}E$, where E is the average energy of the massive particle.

Synchrotron self-Compton

Synchrotron self-Compton (SSC) combines the mechanisms described above. Low-energy photons generated via synchrotron emission interact with the same electron population through inverse Compton scattering, gaining energy in the process. The resulting SSC spectrum is generally harder than the synchrotron spectrum, primarily due to an additional logarithmic dependence of the flux on energy. For an electron distribution following a power law, $N = kE^{-\Gamma}$, the flux scales as k^2 because electrons contribute both to the seed photon field and to the scattering process.

SSC has been invoked to explain the gamma-ray emission observed in sources such as PWNe and AGNs. It becomes particularly relevant when the soft photon density is high and inverse Compton losses are comparable to synchrotron losses. This can be quantified by evaluating the ratio of the energy loss rates for each process:

$$\eta = \frac{\left(\frac{dE}{dt}\right)_{IC}}{\left(\frac{dE}{dt}\right)_{SR}} \tag{A.9}$$

When $\eta > 1$, a synchro-Compton catastrophe is expected, whereby most of the synchrotron radio emission is upscattered into X-ray and gamma-ray energies. Fig. A.2 illustrates a typical SSC spectrum, showing two distinct peaks: one from SR and the other from IC emission.

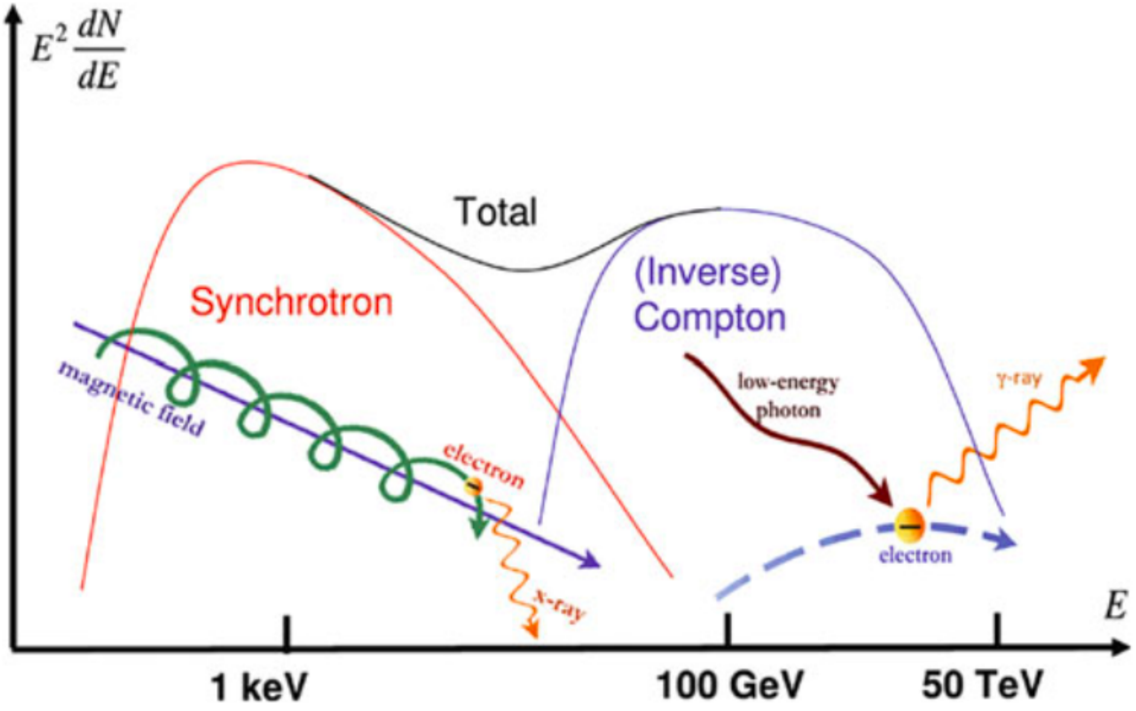

Figure A.2: Illustrative spectral energy distribution of the synchrotron self-Compton (SSC) mechanism. The low-energy peak originates from synchrotron radiation, while the high-energy peak results from inverse Compton scattering of the synchrotron photons by the same electron population.
Credit: De Angelis and Pimenta, 2018.

Bremsstrahlung

Bremsstrahlung, also called free-free emission, arises when charged particles undergo deceleration in the electrostatic field of atomic nuclei, leading to the emission of radiation. This process is involved in various astrophysical scenarios, as well as in the radiation generated during the evolution of atmospheric electromagnetic cascades (see Appendix C), a mechanism exploited by certain ground-based gamma-ray telescopes for the indirect detection of VHE photons reaching Earth.

B. Cherenkov radiation

When a charged particle propagates through a dielectric medium at a velocity greater than the phase velocity of light in that medium, it emits Cherenkov radiation (Rybicki and Lightman, 1979). The effect arises from the polarization of the medium along the path of the particle, followed by the de-excitation of the molecules, which releases photons. If the velocity of the particle is below the light speed in the medium, the wavefronts are nearly isotropic; if it exceeds this threshold, a coherent shockwave is produced in the forward direction, as shown in Fig. B.1 and Fig. B.2.

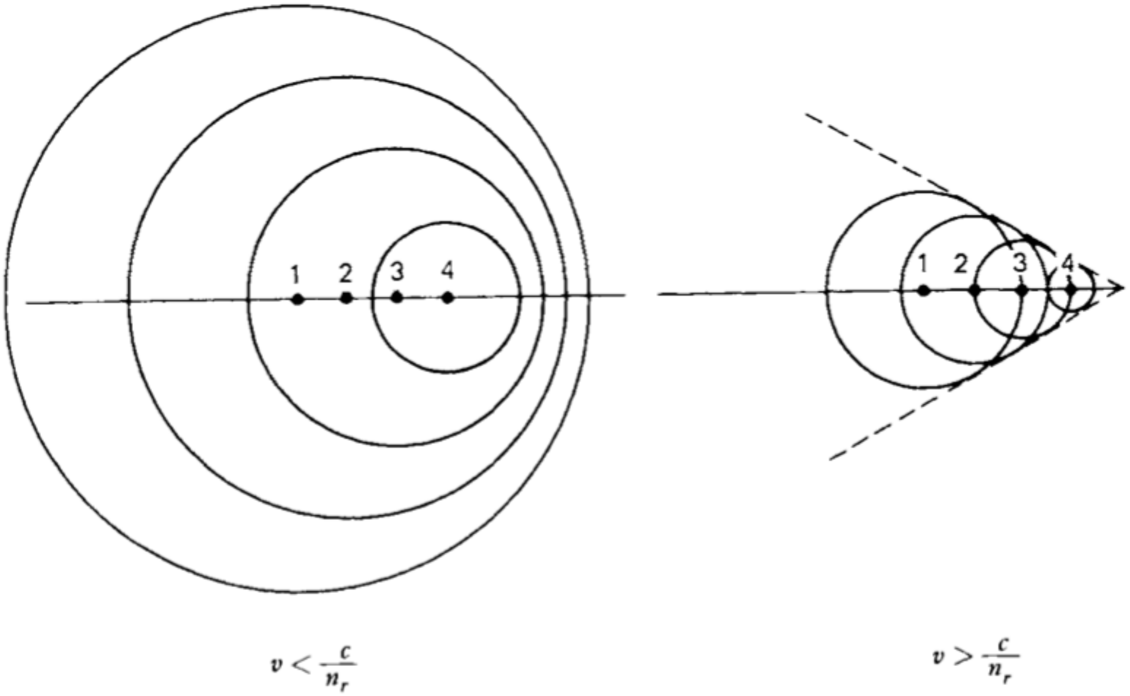

Figure B.1: Formation of Cherenkov radiation by a charged particle traversing a dielectric medium. When the particle velocity exceeds the phase velocity of light in the medium, the emitted wavefronts interfere constructively, producing a coherent shockwave.
Credit: Rybicki and Lightman, 1979.

The emission condition can be expressed as:

$$\beta n_r > 1 \tag{B.1}$$

where $\beta = v/c$ is the particle velocity in units of the vacuum light speed, and n_r is the refractive index of the medium. The corresponding minimum kinetic energy is:

$$E_{min} = 511\ \text{keV} \left[\left(1 - \frac{1}{n_r^2} \right)^{-1/2} - 1 \right] \tag{B.2}$$

showing that the threshold decreases with increasing n_r. Hence, denser media (e.g. water) require lower particle energies for Cherenkov light production compared to the atmosphere.

The radiation is confined within a cone of half-opening angle θ (see Fig. B.2), given by:

$$\theta = \frac{1}{\beta n_r} \tag{B.3}$$

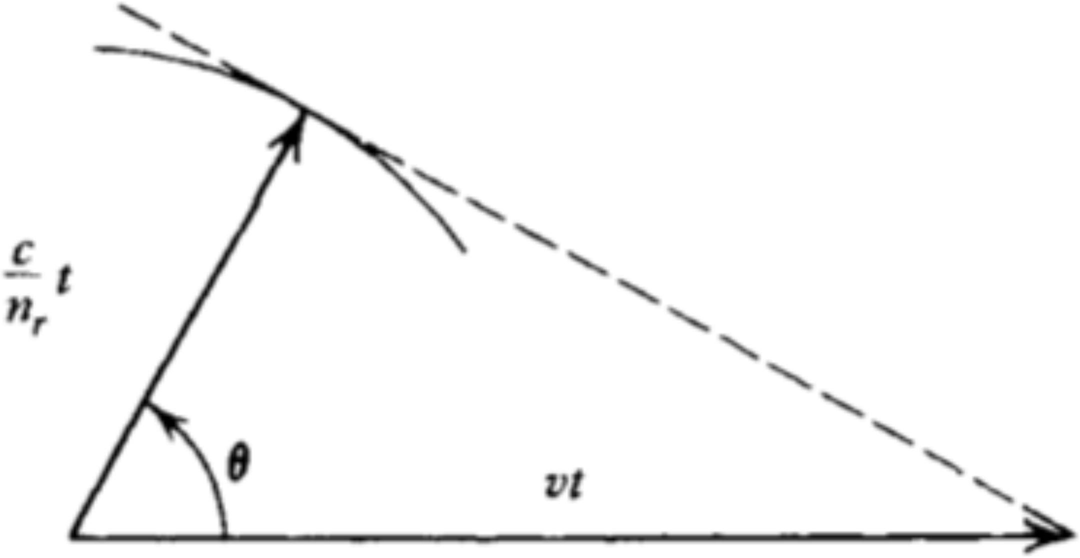

Figure B.2: Geometry of Cherenkov emission: the radiation is confined within a cone of half-opening angle θ, defined by the condition $\theta = \frac{1}{\beta n_r}$.
Credit: Rybicki and Lightman, 1979.

The differential photon yield per unit path length l and per photon energy interval is:

$$\frac{dN}{dE} = l \frac{\alpha}{\hbar c} \sin^2 \theta \tag{B.4}$$

where α is the fine-structure constant and $\hbar$ the reduced Planck constant.

For Cherenkov light from extensive air showers (EAS; see Appendix C), the following properties hold:

- The maximum development of a typical shower occurs at $\sim$10 km a.s.l., producing a light cone with $\theta \sim 1$ deg. At ~ 2 km a.s.l., the light pool radius is around 120 m.
- The spectral distribution peaks in the near-UV, between 300 and 350 nm, with intensities lower than the Night Sky Background (NSB).
- Pulse durations are extremely short, lasting only a few nanoseconds.
- The total Cherenkov light yield is directly related to the energy of the primary particle.

C. Extensive air showers

A gamma ray of energy E_0 entering the atmosphere typically initiates an electromagnetic cascade at altitudes of 20-25 km. In the Heitler model (Heitler, 1954), each interaction converts the gamma ray into an electron-positron pair. These leptons emit photons via Bremsstrahlung (see Appendix A), which generate further pairs. Each interaction approximately halves the energy of the secondary particles, and the process continues until the critical energy $E_{cr} \approx 81$ MeV, where ionization losses dominate. A schematic of this cascade is shown in Fig. C.1.

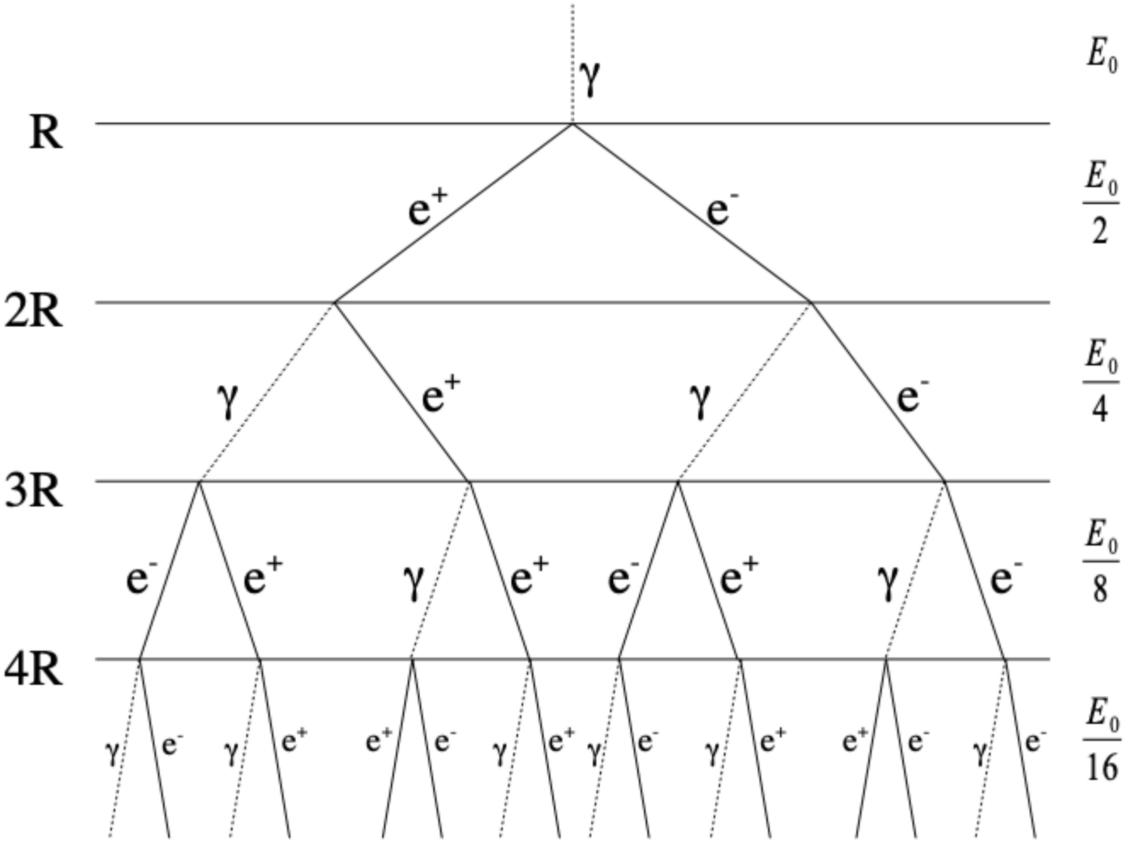

Figure C.1: Schematic illustration of an electromagnetic cascade in the atmosphere according to the Heitler model (Heitler, 1954). A primary gamma ray produces an electron-positron pair, whose Bremsstrahlung photons generate further pairs. The process repeats until particle energies fall below a critical energy.

Credit: Naurois, 2012.

Assuming an exponential decrease of particle energy with atmospheric depth, the altitude of shower maximum can be estimated as:

$$X_{max} = X_0 \ln(N_{max}) = X_0 \ln\left(\frac{E_0}{E_{cr}}\right) \tag{C.1}$$

where X_0 is the radiation length ($X_0 \approx 36.7 gcm^{-2}$ in air).

A more precise description is given by the Greisen's model (Greisen et al., 1956):

$$N(t) = \frac{0.31}{\sqrt{\beta}} \exp\left(t - \frac{3}{2}\ln s\right) \tag{C.2}$$

where N(t) is the number of particles, $t = X/X_0$, $\beta = \ln(E/E_{cr})$, and the shower age s is defined as:

$$s = \frac{3t}{t + 2\beta} \tag{C.3}$$

The parameter s describes the shower development stage: s=0 corresponds to initiation, and s=1 marks maximum development.

Electromagnetic cascades form only one subclass of extensive air showers (EAS). Most EAS are initiated by cosmic rays, primarily protons, interacting with atmospheric nuclei. These collisions produce neutral and charged mesons. Neutral pions decay into photons, which generate secondary electromagnetic showers, while charged pions decay into muons and neutrinos. Although some secondaries penetrate deep into the atmosphere or reach the ground, the electromagnetic component contains the majority of the primary energy. Fig. C.2 compares a gamma-ray-induced shower with a hadron-induced one. Hadronic showers develop more irregularly and represent the dominant background in ground-based gamma-ray observations, making their discrimination a major challenge in the VHE regime.

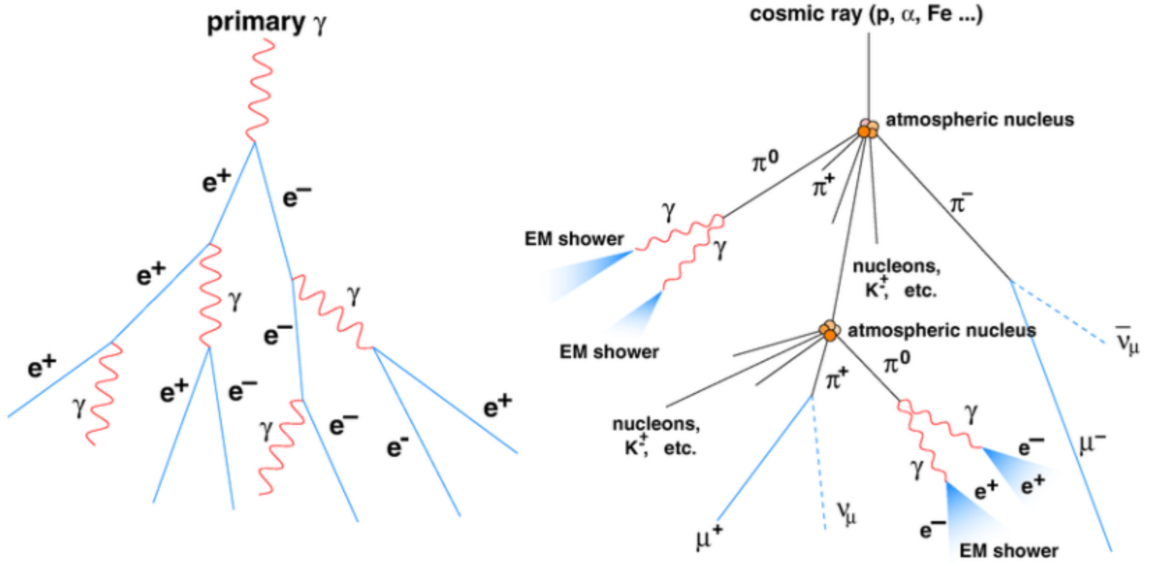

Figure C.2: Comparison between an electromagnetic air shower initiated by a primary gamma ray and a hadronic shower initiated by a proton. Hadronic showers produce both electromagnetic and muonic components, leading to a more irregular development and representing the dominant background in ground-based gamma-ray observations.

Credit: de Angelis, Mansutti, and Persic, 2008.

List of abbreviations

AGN	Active Galactic Nuclei
CTAO	Cherenkov Telescope Array Observatory
CR	Curvature Radiation
DL	Data Level
EAS	Extensive Air Shower
FoV	Field of View
GRB	Gamma-Ray Burst
GW	Gravitational Wave
HE	High Energy
IACT	Imaging Atmospheric Cherenkov Telescope
IC	Inverse Compton
IRF	Instrument Response Function
LAT	Large Area Telescope
LC	Light Cylinder
LHAASO	Large High Altitude Air Shower Observatory
LST	Large-Sized Telescope
MAGIC	Major Atmospheric Gamma Imaging Cherenkov
MC	Monte Carlo
MST	Medium-Sized Telescope
OG	Outer Gap
PC	Polar Cap
PSF	Point Spread Function
PWN	Pulsar Wind Nebula
RF	Random Forest
SED	Spectral Energy Distribution
SiPM	Silicon Photomultiplier
SNR	Supernova Remnant
SR	Synchrotron Radiation
SSC	Synchrotron Self-Compton
SST	Small-Sized Telescope
VHE	Very High Energy
Zd	Zenith distance

List of Figures

1.1 Spectrum of cosmic rays measured by several experiments (after 2000). It follows a power law with distinct features: the knee at $\sim 4.5 \times 10^{15}$ eV, the second knee at $\sim 10^{17}$ eV, the ankle at $\sim 4 \times 10^{18}$ eV, and a final suppression above $\sim 4 \times 10^{20}$ eV. The ankle is generally interpreted as the transition to an extragalactic origin rather than a Galactic one. Credit: Evoli, 2020. 7

1.2 This image displays the entire sky at energies above 1 GeV, derived from five years of observations with *Fermi*-LAT. Brighter regions correspond to more intense gamma-ray emission. The points represent the resolved gamma-ray sources, while the diffuse Galactic emission mainly originates from the interactions of cosmic rays with the interstellar medium and radiation fields. While unresolved sources contributing only a minor fraction. Credit: NASA/DOE/Fermi LAT Collaboration, `https://fermi.gsfc.nasa.gov/ssc/Fermi_5_year.jpg`. 10

1.3 Upper left: Vela pulsar with its wind nebula. Credit: NASA/CXC/Univ of Toronto/M.Durant et al., `https://chandra.harvard.edu/photo/2013/vela/`. Upper right: Cassiopeia A, an example of SNR. Credit: NASA/CXC/SAO/ESA/STScI/CSA/JPL/CalTech/Milisavljevic et al., `https://chandra.harvard.edu/photo/2024/casa/`. Lower left: SS 433, an example of microquasar. Credit: NRAO/AUI/NSF, K. Golap, M. Goss; NASA's Wide Field Survey Explorer (WISE). `https://www.nrao.edu/pr/2013/w50/index.shtml`. Lower right: the Heart nebula, an example of star cluster. Credit: John Corban, ESA/ESO/NASA. Software used Photoshop and FITS Liberator. `https://www.esa.int/ESA_Multimedia/Images/2013/02/The_Heart_nebula`. 13

1.4 Schematic representation of the AGN structure and its classification within the unified model (Antonucci, 1993). The observed type depends on the viewing angle, the presence and strength of jet emission, and the power of the central engine. Credit: Beckmann and Shrader, 2012. 15

1.5 An image of the *Fermi* satellite. Credit: NASA, `https://science.nasa.gov/toolkits/spacecraft-icons`. 18

2.1 Jocelyn Bell at the Mullard Radio Astronomy Observatory and the notes in which she realized she had observed for the first time in history a signal from a pulsar. Credit: `edu.inaf`. 22

2.2 Internal structure of a neutron star and its main characteristics. Credit: Gendreau, Arzoumanian, and Okajima, 2012. 26

2.3 A map showing radio and optical pulsars. They are primarily distributed along the Galactic plane, though several are found at higher Galactic latitudes. The map distinguishes between different sub-populations of pulsars and includes those located in the Magellanic Clouds. Credit: Rami Mandow, `https://www.spaceaustralia.com/feature/milky-ways-cosmic-clocks-pulsars`. 29

2.4 $P-\dot{P}$ diagram showing the current population of pulsars, including those detected by *Fermi*-LAT. Different pulsar classes are color-coded according to the legend. Dashed lines indicate constant magnetic field strength, characteristic age, and spin-down power, highlighting the physical relationships between these parameters. Credit: Smith et al., 2023. 30

2.5 Simulated gamma-ray phaseograms (emission intensity vs rotational phase) of the same pulsar for different magnetic inclination angles and observer viewing angles. Credit: Grenier and A. K. Harding, 2015. 32

2.6 Schematic view of a pulsar magnetosphere. The light cylinder separates the closed-field region, co-rotating with the star, from the open-field region where particles escape. The figure also illustrates the main gamma-ray emission regions: polar cap, slot gap, and outer gap. Credit: Aliu et al., 2008. 33

2.7 Schematic representation of the critical field line in pulsar magnetosphere. The critical line separates regions dominated by opposite charges. Credit: Goldreich and Julian, 1969. 34

2.8 Structure of the equatorial current sheet in pulsar magnetosphere. The discontinuity in the magnetic field and the toroidal component near the last closed field lines form a Y-shaped separatrix, channeling part of the current back to the neutron star. Credit: Cerutti and Beloborodov, 2017. 35

2.9 Gamma-ray pulsar positions projected onto a Milky Way model. Credit: Smith et al., 2023. 38

2.10 Distribution of cutoff energies of gamma-ray pulsars detected by *Fermi*-LAT. Most pulsars show E_c values between 0.5 and 5 GeV, with a typical cutoff near 1 GeV. The dashed vertical line indicates $E_c = 2$ GeV just for reference. Credit: Pathania, Singh, and Yadav, 2023. 39

2.11 Position in galactic coordinate of the four know pulsars detected in the VHE regime. Credit: TeVCat (Wakely and Horan, 2008), `https://tevcat2.tevcat.org`. . . . 41

2.12 Schematic representation of the polar cap (PC) and outer gap (OG) models for gamma-ray pulsar emission. In the PC model, pulsed gamma rays originate from curvature radiation near the neutron star surface, whereas the OG model places the emission in the outer magnetosphere, between the null-charge surface and the light cylinder. Credit: Lopez et al., 2009. 45

2.13 Phase-resolved spectral energy distribution (SED) of the Vela pulsar (P2 peak) combining *Fermi*-LAT and H.E.S.S. data (both stereo and mono). The GeV component is consistent with curvature or synchrotron radiation, while the hard extension up to 20 TeV requires inverse-Compton scattering in the Klein-Nishina regime. Model curves illustrate CR/IC and SR/IC scenarios. Credit: H. E. S. S. Collaboration, F. Aharonian, et al., 2023. 47

2.14 Schematic view of the main pulsar VHE emission models. Electrons can be accelerated (1) along magnetic field lines inside the light cylinder (LC), in outer-gap regions or just beyond it (separatrix/current sheet), or (2) through magnetic reconnection in the equatorial current sheet of the stripped wind beyond the LC. GeV photons are mainly produced via curvature or synchrotron radiation, while TeV emission arises from inverse-Compton scattering of optical-IR photons. Spatial scales are not respected: the pulsar radius is ~ 10 km, while the LC radius is ~ 4300 km. Credit: H. E. S. S. Collaboration, F. Aharonian, et al., 2023. 48

2.15 Schematic of the pulsar wind model: particle acceleration occurs in a narrow region beyond the light cylinder, where the Poynting-dominated outflow converts into particle kinetic energy. Credit: Aharonian, Bogovalov, and Khangulyan, 2012a. . . . 49

2.16 Phase-resolved SED of P1 (black circles) and P2 (blue circles) of the Crab pulsar obtained from the MAGIC telescopes dataset. The Crab Nebula spectrum (open black squares) is also shown for comparison. Credit: Ansoldi et al., 2016. 50

2.17 Schematic view of the stripped pulsar wind and the associated current sheet. If the magnetic and rotational axes are misaligned, the current sheet oscillates with the pulsar spin, producing a striped pattern that separates regions of opposite polarity. The observed pulse profile arises when the line of sight intersects this geometry, with particle acceleration and emission occurring in the reconnection layers of the sheet. Credit: Mochol, 2017. 51
2.18 The Crab Nebula as seen by Hubble Space Telescope (left) and James Webb Space Telescope (right). Credit: NASA, ESA, J. Hester and A. Loll (Arizona State University), `https://science.nasa.gov/asset/hubble/a-giant-hubble-mosaic-of-the-crab-nebula/`; NASA, ESA, CSA, STScI, T. Temim (Princeton University), `https://www.nasa.gov/missions/webb/the-crab-nebula-seen-in-new-light-by-nasas-webb/`. 52
2.19 Composited image of the Crab Nebula (left image) with X-ray observations by Chandra (upper right), optical by the Hubble Space Telescope (middle right), and infrared by Spitzer Space Telescope (lower right). The Crab pulsar is located at the center of the Nebula and is intense in X-rays. Credit: NASA/CXC/SAO/STScI/JPL-Caltech, `https://chandra.harvard.edu/photo/2018/crab/`. 53
2.20 Broadband emission of the Crab Nebula, spanning from radio to PeV gamma rays. VHE gamma-ray data from multiple instruments, including MAGIC, VERITAS, TIBET ASγ, and LHAASO, are displayed. The observed spectrum is reproduced by combining different emission processes across the electromagnetic spectrum. Two prominent components are evident: synchrotron radiation and inverse Compton, the latter described by the SSC process. Credit: Dirson and Horns, 2023. 54
2.21 Crab pulsar phaseograms across the electromagnetic spectrum, from radio to very high energy gamma rays. The phaseogram shows emission intensity versus rotational phase, typically plotted over two cycles for clarity. A property of the Crab is the phase stability of its two peaks across all bands, while their relative amplitudes and morphology change. Credit: Abdo, Ackermann, et al., 2010. 55
2.22 Early radio pulse profiles of the Crab pulsar, obtained in 1968 by integrating a large number of periods to enhance the signal-to-noise ratio. It shows the characteristic double-peaked structure that has remained stable over decades. Credit: Comella et al., 1969. 56

3.1 Artistic representation of the Imaging Atmospheric Cherenkov Telescopes (IACTs) technique. Cherenkov light produced in an atmospheric shower is reflected by a large mirror and focused onto a camera, where the shower image is recorded. Credit: CTAO/ESO, `https://www.eso.org/public/images/eso1841x/`. 59
3.2 The three telescope classes foreseen in the CTAO design, compared to the average human height. Small-Sized Telescopes (SSTs) will probe the highest energies, Medium-Sized Telescopes (MSTs) the intermediate range, and Large-Sized Telescopes (LSTs) the lowest energies. Credit: `https://www.ctao.org/emission-to-discovery/telescopes/`. 60
3.3 Layout of the CTAO Northern and Southern array. Credit: Gueta, 2022. 61
3.4 Differential flux sensitivity of CTAO (for 50 hours of observation) compared with current instruments. Credit: `https://www.ctao.org/for-scientists/performance/`. 62
3.5 Angular resolution of CTAO compared with current instruments. Credit: `https://www.ctao.org/for-scientists/performance/`. 63
3.6 Picture of the prototype for the Large-Sized Telescopes, LST-1. 64

4.1 Flowchart of the LST-1 analysis chain. Raw data (R0) are sequentially processed to generate calibrated data (R1), calibrated images (DL1a), cleaned and parameterized images (DL1b), reconstructed datasets (DL2), and filtered DL3 files for scientific analysis. Supplementary Monte Carlo simulations and calibration datasets are required to model the telescope and electronics response. Credit: Mas Aguilar, 2025. . 70
4.2 Schematic view of the ON/OFF and Wobble observation modes. In ON/OFF mode, the source is placed at the camera center during one run, while a separate run on a source-free field provides the background estimate. In Wobble mode, both ON and OFF regions are derived from the same run, with the source observed at an offset of ±0.4 deg from the camera center. Credit: Mas Aguilar, 2025. 71
4.3 Simulated gamma-ray shower image in the camera with NSB noise, shown after applying three different sets of cleaning parameters (reported in each graph). In the first image, high thresholds remove part of the shower image, while in the last panel residual NSB noise remains visible after cleaning. Credit: Mas Aguilar, 2025. . . . 75
4.4 Main Hillas parameters defined by the shower geometry and the source location. Credit: Carreto Fidalgo, 2019. 76

4.5 Examples of θ^2 and α distributions from data taken with LST-1. The low-value excess corresponds to gamma rays originating from the source. Credit: Mas Aguilar, 2025. 79

4.6 Distribution of run durations (left) and zenith distances (right) for the Crab pulsar observations with LST-1 from October 2018 until July 2025. 85

4.7 Total observation time as a function of zenith distance for all accepted runs after run-quality selection. The vertical dashed and dotted red lines indicate the limits at Zd = 70 deg and Zd = 50 deg, respectively. Horizontal lines mark the corresponding total exposures: ∼ 209 hr and ∼ 180 hr. 86

4.8 Quality selection summary. Gray histograms represent all runs available in LST-1 dataset, outlined histograms are runs after the source selection + date range preselection, and vertical lines show thresholds adopted in the data quality selection. Panels from top-left to bottom-right display: σ_δ, Zd, diffuse NSB std, mean fit -value, dR/dI at 422 p.e., fraction around dR/dI mode, spectral index, max Lomb–Scargle amplitude of dR/dI at 422 p.e., Zd-corrected intensity threshold (50% of the peak), and (uncorrected) intensity at peak rate. 88

4.9 Scheme of the LST-1 pulsar analysis chain. The brown-shaded block represents the procedure to produce DL3 files through `lstchain`, which serve as the input for the pulsar analysis. The blue-shaded block represents the timing analysis performed with `PulsarTimingAnalysis`, which is carried out from the DL3 level and produces files in which each event is assigned a rotational phase of the pulsar. Then, the dataset is ready for high-level analysis which uses `PulsarTimingAnalysis` through `Gammapy` to produce phaseograms and SEDs. Credit: Mas Aguilar, 2025. 92

5.1 Phaseogram of the Crab pulsar from LST-1 data, for a total observation time of about 180 hours. The first peak P1 is defined by the yellow region, while the second peak P2 is defined by the green region. It is also indicated the background region, defined by the gray band. The graph shows two phases for better visualization. 97

5.2 Evolution of the detection significance for the Crab pulsar peaks P1, P2, and their combined emission P1+P2 as a function of observation time. The dashed lines show the expected $\propto \sqrt{t}$ dependence, where t is the total observation time. 98

5.3 Number of excess events from the Crab pulsar as a function of observation time. The excess shows the expected linear dependence on time. 99

5.4 Phase-resolved SEDs of the Crab pulsar peaks P1 (red) and P2 (cyan) obtained with LST-1 data between 20 GeV and 1 TeV. The flux points are derived in six energy bins with 1σ statistical uncertainties, the solid lines represent the best-fit power-law models with their the statistical uncertainty band (derived by error propagation). The spectral points are summarized in Table 5.2, while the fit parameters are reported in Table 5.3. 101

5.5 Comparison of the SED of peak P1 obtained in this work (red) with the SED reported by Abe et al. (2024) (orange), with their associated statistical uncertainties. The result of this work includes one additional spectral point at higher energies, extending the analysis up to 1 TeV, beyond the last significant bin of the earlier LST-1 results. The discrepancy below ∼50 GeV is discussed in the text. 102

5.6 Comparison of the SED of peak P2 obtained in this work (cyan) with the results reported by Abe et al. (2024) (orange), with their associated statistical uncertainties. The result of this work includes one additional spectral point at higher energies, extending the analysis up to 1 TeV, beyond the last significant bin of the earlier LST-1 results. The discrepancy below ∼50 GeV is discussed in the text. 103

5.7 Comparison of the SED of peak P1 obtained in this work (red) with the results reported by Ansoldi et al. (2016) (green), with their associated statistical uncertainties. The result of this work includes additional spectral points at lower energies, thanks to the improved threshold of LST-1, and one additional spectral point at higher energies, extending the analysis up to 1 TeV beyond the last significant bin of the MAGIC analysis. 104

5.8 Comparison of the SED of peak P2 obtained in this work (cyan) with the results reported by Ansoldi et al. (2016) (green), with their associated statistical uncertainties. The result of this work includes additional spectral points at lower energies, thanks to the improved threshold of LST-1, and confirms the compatibility of the spectrum with MAGIC results up to 1 TeV. 105

5.9 Summary plot of the spectral points for peak P1 from this work (red), MAGIC (Ansoldi, Antonelli, Antoranz, et al., 2016) (green), and LST-1 (Abe et al., 2024) (orange). The present analysis provides one additional point up to ∼1 TeV. 106

5.10 Summary plot of the spectral points for peak P2 from this work (cyan), MAGIC (Ansoldi, Antonelli, Antoranz, et al., 2016) (green), and LST-1 (Abe et al., 2024) (orange). The present analysis provides one additional point up to 1 TeV with respect to LST-1, and demonstrate compatibility with MAGIC results. 106

A.1 Function F(x) as a function of x= ν/ν_c, showing a maximum at x=0.29. It describes the normalized spectral distribution of synchrotron radiation. Credit: Rybicki and Lightman, 1979. 113

A.2 Illustrative spectral energy distribution of the synchrotron self-Compton (SSC) mechanism. The low-energy peak originates from synchrotron radiation, while the high-energy peak results from inverse Compton scattering of the synchrotron photons by the same electron population. Credit: De Angelis and Pimenta, 2018. 116

B.1 Formation of Cherenkov radiation by a charged particle traversing a dielectric medium. When the particle velocity exceeds the phase velocity of light in the medium, the emitted wavefronts interfere constructively, producing a coherent shockwave. Credit: Rybicki and Lightman, 1979. 117

B.2 Geometry of Cherenkov emission: the radiation is confined within a cone of half-opening angle θ, defined by the condition $\theta = \frac{1}{\beta n_r}$. Credit: Rybicki and Lightman, 1979. 118

C.1 Schematic illustration of an electromagnetic cascade in the atmosphere according to the Heitler model (Heitler, 1954). A primary gamma ray produces an electron-positron pair, whose Bremsstrahlung photons generate further pairs. The process repeats until particle energies fall below a critical energy. Credit: Naurois, 2012. . . 120

C.2 Comparison between an electromagnetic air shower initiated by a primary gamma ray and a hadronic shower initiated by a proton. Hadronic showers produce both electromagnetic and muonic components, leading to a more irregular development and representing the dominant background in ground-based gamma-ray observations. Credit: de Angelis, Mansutti, and Persic, 2008. 122

List of Tables

4.1 Data levels in the LST-1 analysis chain. The processing reduces raw data (R0) to final science products (DL5). The table lists, for each level, its designation, corresponding primary data file levels, and file contents. 69

4.2 Parameters stored in the Event List table of the DL3 files generated with `lstchain`. The first column specifies the parameter name, the second provides its description, and the third indicates whether it is mandatory or not. 82

4.3 Number of runs remaining after each quality cut. Percentages are relative to the number of runs after the zenith selection (1366 runs). After applying quality selection criteria, 779 runs are retained. *Presence requirement for each run to contain interleaved flat-field (FF) and pedestal events. 87

4.4 Standard event-selection cuts applied during the DL2 → DL3 conversion with `lstchain`. 90

4.5 Phase regions of the two emission peaks of the Crab pulsar P1 and P2 adopted in this work, defined by Aleksić et al. (2012). 95

5.1 Statistical significance of the pulsed emission from the Crab pulsar derived with the Li & Ma formula (Eq. 4.3). Values are reported for the individual peaks P1 and P2, as well as for their combined emission P1+P2. 98

5.2 Spectral points of the Crab pulsar peaks P1 and P2 obtained with LST-1 data between 20 GeV and 1 TeV. The table reports the energy bin, the bin center, and the fluxes expressed as $E^2 dN/dEdAdt$ with 1σ statistical uncertainties. 101

5.3 Best-fit power-law parameters of the phase-resolved SEDs of the Crab pulsar peaks P1 and P2 from 20 GeV to 1 TeV. The table reports the reference energy E_0, the normalization ϕ_0, and the spectral index Γ, derived from the likelihood fit of LST-1 data. 102

Bibliography

Abbott, B. P. et al. (Oct. 2017). “GW170817: Observation of Gravitational Waves from a Binary Neutron Star Inspiral”. In: *Phys. Rev. Lett.* 119.16, 161101, p. 161101. DOI: `10.1103/PhysRevLett.119.161101`. arXiv: `1710.05832 [gr-qc]`.

Abdo, A. A., M. Ackermann, et al. (Jan. 2010). “Fermi Large Area Telescope Observations of the Crab Pulsar And Nebula”. In: *ApJ* 708.2, pp. 1254–1267. DOI: `10.1088/0004-637X/708/2/1254`. arXiv: `0911.2412 [astro-ph.HE]`.

Abdo, A. A., B. Allen, et al. (Aug. 2007). “TeV Gamma-Ray Sources from a Survey of the Galactic Plane with Milagro”. In: *ApJ* 664.2, pp. L91–L94. DOI: `10.1086/520717`. arXiv: `0705.0707 [astro-ph]`.

Abdo, A. A., B. T. Allen, et al. (May 2012). “Observation and Spectral Measurements of the Crab Nebula with Milagro”. In: *ApJ* 750.1, 63, p. 63. DOI: `10.1088/0004-637X/750/1/63`. arXiv: `1110.0409 [astro-ph.HE]`.

Abe et al. (Oct. 2024). “A detailed study of the very high-energy Crab pulsar emission with the LST-1”. In: *A&A* 690, A167, A167. DOI: `10.1051/0004-6361/202450059`. arXiv: `2407.02343 [astro-ph.HE]`.

Abe, K. et al. (June 2025). “Detection of the Geminga pulsar at energies down to 20 GeV with the LST-1 of CTAO”. In: *A&A* 698, A283, A283. DOI: `10.1051/0004-6361/202554350`. arXiv: `2505.21632 [astro-ph.HE]`.

Abe, K. et al. (Oct. 2024). “A detailed study of the very high-energy Crab pulsar emission with the LST-1”. In: *A&A* 690, A167, A167. DOI: `10.1051/0004-6361/202450059`. arXiv: `2407.02343 [astro-ph.HE]`.

Abe, S., J. Abhir, et al. (Oct. 2024). “Prospects for a survey of the galactic plane with the Cherenkov Telescope Array”. In: *J. Cosmology Astropart. Phys.* 2024.10, 081, p. 081. DOI: `10.1088/1475-7516/2024/10/081`. arXiv: `2310.02828 [astro-ph.HE]`.

Abe, S., A. Aguasca-Cabot, et al. (May 2023). “Multiwavelength study of the galactic PeVatron candidate LHAASO J2108+5157”. In: *A&A* 673, A75, A75. DOI: `10.1051/0004-6361/202245086`. arXiv: `2210.00775 [astro-ph.HE]`.

Abeysekara, A. U. et al. (Aug. 2019). “Measurement of the Crab Nebula Spectrum Past 100 TeV with HAWC”. In: *ApJ* 881.2, 134, p. 134. DOI: `10.3847/1538-4357/ab2f7d`. arXiv: `1905.12518 [astro-ph.HE]`.

Abeysekara, A. U., A. Albert, R. Alfaro, C. Alvarez, J. D. Álvarez, M. Araya, et al. (July 2023). "The High-Altitude Water Cherenkov (HAWC) observatory in México: The primary detector". In: *Nuclear Instruments and Methods in Physics Research A* 1052, 168253, p. 168253. DOI: `10.1016/j.nima.2023.168253`. arXiv: `2304.00730 [astro-ph.HE]`.

Abeysekara, A. U., A. Albert, R. Alfaro, C. Alvarez, J. D. Álvarez, R. Arceo, et al. (July 2017). "The 2HWC HAWC Observatory Gamma-Ray Catalog". In: *ApJ* 843.1, 40, p. 40. DOI: `10.3847/1538-4357/aa7556`. arXiv: `1702.02992 [astro-ph.HE]`.

Abeysekara, A. U., A. Archer, et al. (July 2018). "A Very High Energy γ-Ray Survey toward the Cygnus Region of the Galaxy". In: *ApJ* 861.2, 134, p. 134. DOI: `10.3847/1538-4357/aac4a2`. arXiv: `1805.05989 [astro-ph.HE]`.

Acciari, V. A. et al. (Apr. 2022). "Proton acceleration in thermonuclear nova explosions revealed by gamma rays". In: *Nature Astronomy* 6, pp. 689–697. DOI: `10.1038/s41550-022-01640-z`. arXiv: `2202.07681 [astro-ph.HE]`.

Ackermann, M., M. Ajello, et al. (Jan. 2015). "The Spectrum of Isotropic Diffuse Gamma-Ray Emission between 100 MeV and 820 GeV". In: *ApJ* 799.1, 86, p. 86. DOI: `10.1088/0004-637X/799/1/86`. arXiv: `1410.3696 [astro-ph.HE]`.

Ackermann, M., A. Albert, et al. (Sept. 2014). "The Spectrum and Morphology of the Fermi Bubbles". In: *ApJ* 793.1, 64, p. 64. DOI: `10.1088/0004-637X/793/1/64`. arXiv: `1407.7905 [astro-ph.HE]`.

Aharonian, S. V. Bogovalov, and D. Khangulyan (Feb. 2012a). "Abrupt acceleration of a 'cold' ultrarelativistic wind from the Crab pulsar". In: *Nature* 482.7386, pp. 507–509. DOI: `10.1038/nature10793`.

— (Feb. 2012b). "Abrupt acceleration of a 'cold' ultrarelativistic wind from the Crab pulsar". In: *Nature* 482.7386, pp. 507–509. DOI: `10.1038/nature10793`.

Aharonian, F. et al. (Apr. 2001). "Evidence for TeV gamma ray emission from Cassiopeia A". In: *A&A* 370, pp. 112–120. DOI: `10.1051/0004-6361:20010243`. arXiv: `astro-ph/0102391 [astro-ph]`.

— (May 2003). "Is the giant radio galaxy M 87 a TeV gamma-ray emitter?" In: *A&A* 403, pp. L1–L5. DOI: `10.1051/0004-6361:20030372`. arXiv: `astro-ph/0302155 [astro-ph]`.

Aharonian, F., A. Akhperjanian, et al. (Oct. 2004). "The Crab Nebula and Pulsar between 500 GeV and 80 TeV: Observations with the HEGRA Stereoscopic Air Cerenkov

Telescopes”. In: *ApJ* 614.2, pp. 897–913. DOI: `10.1086/423931`. arXiv: `astro-ph/0407118 [astro-ph]`.

Aharonian, F., A. G. Akhperjanian, et al. (May 2007). “Search for pulsed VHE gamma-ray emission from young pulsars with HESS”. In: *A&A* 466.2, pp. 543–554. DOI: `10.1051/0004-6361:20066737`. arXiv: `astro-ph/0702336 [astro-ph]`.

Aharonian, F. A. and G. Heinzelmann (Jan. 1998). “The HEGRA Experiment Status and Recent Results”. In: *Nuclear Physics B Proceedings Supplements* 60.3, pp. 193–198. DOI: `10.1016/S0920-5632(97)00514-8`. arXiv: `astro-ph/9702059 [astro-ph]`.

Albert, A. et al. (June 2020). “HAWC J2227+610 and Its Association with G106.3+2.7, a New Potential Galactic PeVatron”. In: *ApJ* 896.2, L29, p. L29. DOI: `10.3847/2041-8213/ab96cc`. arXiv: `2005.13699 [astro-ph.HE]`.

Aleksić, J. et al. (Nov. 2011). “Observations of the Crab Pulsar between 25 and 100 GeV with the MAGIC I Telescope”. In: *ApJ* 742.1, 43, p. 43. DOI: `10.1088/0004-637X/742/1/43`. arXiv: `1108.5391 [astro-ph.HE]`.

— (Apr. 2012). “Phase-resolved energy spectra of the Crab pulsar in the range of 50-400 GeV measured with the MAGIC telescopes”. In: *A&A* 540, A69, A69. DOI: `10.1051/0004-6361/201118166`. arXiv: `1109.6124 [astro-ph.HE]`.

Aliu, E. et al. (Nov. 2008). “Observation of Pulsed γ-Rays Above 25 GeV from the Crab Pulsar with MAGIC”. In: *Science* 322.5905, p. 1221. DOI: `10.1126/science.1164718`. arXiv: `0809.2998 [astro-ph]`.

Amenomori, M., Z. W. Bai, et al. (Apr. 1991). “Status and performance of the AS array of the Tibet AS$_{gamma}$ experiment”. In: *High Energy Gamma Ray Astronomy*. Ed. by James Matthews. Vol. 220. American Institute of Physics Conference Series, pp. 257–264. DOI: `10.1063/1.40305`.

Amenomori, M., Y. W. Bao, et al. (Apr. 2021). “First Detection of sub-PeV Diffuse Gamma Rays from the Galactic Disk: Evidence for Ubiquitous Galactic Cosmic Rays beyond PeV Energies”. In: *Phys. Rev. Lett.* 126.14, 141101, p. 141101. DOI: `10.1103/PhysRevLett.126.141101`. arXiv: `2104.05181 [astro-ph.HE]`.

Ansoldi, S. et al. (Jan. 2016). “Teraelectronvolt pulsed emission from the Crab Pulsar detected by MAGIC”. In: *A&A* 585, A133, A133. DOI: `10.1051/0004-6361/201526853`. arXiv: `1510.07048 [astro-ph.HE]`.

Ansoldi, S., L. A. Antonelli, P. Antoranz, et al. (Jan. 2016). "Teraelectronvolt pulsed emission from the Crab Pulsar detected by MAGIC". In: *A&A* 585, A133, A133. DOI: `10.1051/0004-6361/201526853`. arXiv: `1510.07048 [astro-ph.HE]`.

Ansoldi, S., L. A. Antonelli, C. Arcaro, et al. (Aug. 2018). "The Blazar TXS 0506+056 Associated with a High-energy Neutrino: Insights into Extragalactic Jets and Cosmic-Ray Acceleration". In: *ApJ* 863.1, L10, p. L10. DOI: `10.3847/2041-8213/aad083`. arXiv: `1807.04300 [astro-ph.HE]`.

Antonucci, Robert (Jan. 1993). "Unified models for active galactic nuclei and quasars." In: *ARA&A* 31, pp. 473–521. DOI: `10.1146/annurev.aa.31.090193.002353`.

Arons, J. (Jan. 1981). "The slot gap model of pulsars". In: *Pulsars: 13 Years of Research on Neutron Stars*. Ed. by W. Sieber and R. Wielebinski. Vol. 95. IAU Symposium, pp. 69–85.

Baade, W. and F. Zwicky (May 1934). "Cosmic Rays from Super-novae". In: *Proceedings of the National Academy of Science* 20.5, pp. 259–263. DOI: `10.1073/pnas.20.5.259`.

Ballet, J. et al. (July 2023). "Fermi Large Area Telescope Fourth Source Catalog Data Release 4 (4FGL-DR4)". In: *arXiv e-prints*, arXiv:2307.12546, arXiv:2307.12546. DOI: `10.48550/arXiv.2307.12546`. arXiv: `2307.12546 [astro-ph.HE]`.

Barrau, A. et al. (Oct. 1998). "The CAT imaging telescope for very-high-energy gamma-ray astronomy." In: *Nuclear Instruments and Methods in Physics Research A* 416.2, pp. 278–292. DOI: `10.1016/S0168-9002(98)00749-9`. arXiv: `astro-ph/9804046 [astro-ph]`.

Beckmann, V. and C. Shrader (Jan. 2012). "The AGN phenomenon: open issues". In: *Proceedings of "An INTEGRAL view of the high-energy sky (the first 10 years)" - 9th INTEGRAL Workshop and celebration of the 10th anniversary of the launch (INTEGRAL 2012). 15-19 October 2012. Bibliotheque Nationale de France*, 69, p. 69. DOI: `10.22323/1.176.0069`. arXiv: `1302.1397 [astro-ph.HE]`.

Bell, S. J. and A. Hewish (Mar. 1967). "Angular Size and Flux Density of the Small Source in the Crab Nebula at 81.5 Mc/s". In: *Nature* 213.5082, pp. 1214–1216. DOI: `10.1038/2131214a0`.

Benbow, Wystan (Feb. 2005). "The Status and Performance of H.E.S.S." In: *High Energy Gamma-Ray Astronomy*. Ed. by Felix A. Aharonian, Heinz J. Völk, and Dieter Horns. Vol. 745. American Institute of Physics Conference Series, pp. 611–616. DOI: `10.1063/1.1878471`.

Bennett, Kevin (Apr. 1990). “COS-B: The highlights”. In: *Nuclear Physics B Proceedings Supplements* 14.2, pp. 23–34. DOI: `10.1016/0920-5632(90)90362-X`.

Bernardini, P. and ARGO-YBJ Collaboration (July 2008). “ARGO-YBJ experiment in Tibet”. In: *Journal of Physics Conference Series*. Vol. 120. Journal of Physics Conference Series, 062022, p. 062022. DOI: `10.1088/1742-6596/120/6/062022`.

Bernlöhr, Konrad (Oct. 2008). “Simulation of imaging atmospheric Cherenkov telescopes with CORSIKA and sim_ telarray”. In: *Astroparticle Physics* 30.3, pp. 149–158. DOI: `10.1016/j.astropartphys.2008.07.009`. arXiv: `0808.2253 [astro-ph]`.

Bose, D. et al. (Jan. 2022). “Galactic and extragalactic sources of very high energy gamma rays”. In: *European Physical Journal Special Topics* 231.1, pp. 27–66. DOI: `10.1140/epjs/s11734-022-00434-8`. arXiv: `2201.06789 [astro-ph.HE]`.

Breiman, Leo (Jan. 2001). “Random Forests.” In: *Machine Learning* 45, pp. 5–32. DOI: `10.1023/A:1010933404324`.

Cameron, Robert A. and Fermi LAT Collaboration (Jan. 2009). “The On-orbit Performance of the Large Area Telescope on Fermi”. In: *American Astronomical Society Meeting Abstracts #213*. Vol. 213. American Astronomical Society Meeting Abstracts, 468.02, p. 468.02.

Cao, Zhen, F. Aharonian, Q. An, Bai Axikegu Y. X., et al. (Oct. 2023). “Measurement of Ultra-High-Energy Diffuse Gamma-Ray Emission of the Galactic Plane from 10 TeV to 1 PeV with LHAASO-KM2A”. In: *Phys. Rev. Lett.* 131.15, 151001, p. 151001. DOI: `10.1103/PhysRevLett.131.151001`. arXiv: `2305.05372 [astro-ph.HE]`.

Cao, Zhen, F. Aharonian, Q. An, Axikegu, et al. (Mar. 2024). “The First LHAASO Catalog of Gamma-Ray Sources”. In: *ApJS* 271.1, 25, p. 25. DOI: `10.3847/1538-4365/acfd29`. arXiv: `2305.17030 [astro-ph.HE]`.

Cao, Zhen, F. A. Aharonian, et al. (June 2021). “Ultrahigh-energy photons up to 1.4 petaelectronvolts from 12 γ-ray Galactic sources”. In: *Nature* 594.7861, pp. 33–36. DOI: `10.1038/s41586-021-03498-z`.

Carreto Fidalgo, David (2019). *Revealing the Most Energetic Light from Pulsars and Their Nebulae*. DOI: `10.1007/978-3-030-24194-0`.

Carroll, Bradley W. and Dale A. Ostlie (2017). *An introduction to modern astrophysics, Second Edition*.

Cawley, M. F. et al. (May 1990). “A High Resolution Imaging Detector for Tev Gamma-Ray Astronomy”. In: *Experimental Astronomy* 1.3, pp. 173–193. DOI: 10.1007/BF00462039.

Cerutti, Benoit and Andrei M. Beloborodov (July 2017). “Electrodynamics of Pulsar Magnetospheres”. In: *Space Sci. Rev.* 207.1-4, pp. 111–136. DOI: 10.1007/s11214-016-0315-7. arXiv: 1611.04331 [astro-ph.HE].

Chai, Yating, Kwong-Sang Cheng, and Jumpei Takata (June 2016). “Probing Gamma-ray Emission of Geminga and Vela with Non-stationary Models”. In: *Journal of Astronomy and Space Sciences* 33, pp. 75–92. DOI: 10.5140/JASS.2016.33.2.75.

Champion, C. et al. (Oct. 2017). “TiCkS: A Flexible White-Rabbit Based Time-Stamping Board”. In: *arXiv e-prints*, arXiv:1710.07128, arXiv:1710.07128. DOI: 10.48550/arXiv.1710.07128. arXiv: 1710.07128 [astro-ph.IM].

Cheng, K., M. Ruderman, and L. Zhang (May 2000). “A Three-dimensional Outer-magnetospheric Gap Model for Gamma-ray Pulsars: I. The Crab Pulsar”. In: *Highly Energetic Physical Processes and Mechanisms for Emission from Astrophysical Plasmas*. Ed. by P. C. H. Martens, S. Tsuruta, and M. A. Weber. Vol. 195. IAU Symposium, p. 223.

Cheng, K. S., C. Ho, and M. Ruderman (Jan. 1986). “Energetic Radiation from Rapidly Spinning Pulsars. I. Outer Magnetosphere Gaps”. In: *ApJ* 300, p. 500. DOI: 10.1086/163829.

Clear, J. et al. (Mar. 1987). “A detailed analysis of the high energy gamma-ray emission from the Crab pulsar and nebula.” In: *A&A* 174, pp. 85–94.

Comella, J. M. et al. (Feb. 1969). “Crab Nebula Pulsar NP 0532”. In: *Nature* 221.5179, pp. 453–454. DOI: 10.1038/221453a0.

Coroniti, F. V. (Feb. 1990). “Magnetically Striped Relativistic Magnetohydrodynamic Winds: The Crab Nebula Revisited”. In: *ApJ* 349, p. 538. DOI: 10.1086/168340.

Cortina, J. and C. l. Project (July 2019). “Status of the Large Size Telescopes of the Cherenkov Telescope Array”. In: *36th International Cosmic Ray Conference (ICRC2019)*. Vol. 36. International Cosmic Ray Conference, 653, p. 653. DOI: 10.22323/1.358.0653. arXiv: 1907.10146 [astro-ph.IM].

Cristofari, Pierre (Aug. 2021). “The Hunt for Pevatrons: The Case of Supernova Remnants”. In: *Universe* 7.9, 324, p. 324. DOI: 10.3390/universe7090324. arXiv: 2110.07956 [astro-ph.HE].

CTA-LST Project et al. (Sept. 2024). “First Science Results from CTA LST-1 Telescope and status of LST-2-4”. In: *38th International Cosmic Ray Conference*, 731, p. 731.

de Angelis, A., O. Mansutti, and M. Persic (Apr. 2008). “Very-high energy gamma astrophysics”. In: *Nuovo Cimento Rivista Serie* 31.4, pp. 187–246. DOI: `10.1393/ncr/i2008-10032-2`. arXiv: `0712.0315 [astro-ph]`.

de Angelis, A., V. Tatischeff, et al. (Aug. 2018). “Science with e-ASTROGAM. A space mission for MeV-GeV gamma-ray astrophysics”. In: *Journal of High Energy Astrophysics* 19, pp. 1–106. DOI: `10.1016/j.jheap.2018.07.001`. arXiv: `1711.01265 [astro-ph.HE]`.

De Angelis, Alessandro and Mário Pimenta (2018). *Introduction to Particle and Astroparticle Physics*. DOI: `10.1007/978-3-319-78181-5`.

De Lotto, Barbara and Magic Collaboration (July 2012). “The MAGIC telescopes: performance, results and future perspectives”. In: *Journal of Physics Conference Series*. Vol. 375. Journal of Physics Conference Series, 052021, p. 052021. DOI: `10.1088/1742-6596/375/1/052021`.

Deil, C. et al. (July 2017). “Gammapy - A prototype for the CTA science tools”. In: *35th International Cosmic Ray Conference (ICRC2017)*. Vol. 301. International Cosmic Ray Conference, 766, p. 766. DOI: `10.22323/1.301.0766`. arXiv: `1709.01751 [astro-ph.IM]`.

Dirson, L. and D. Horns (Mar. 2023). “Phenomenological modelling of the Crab Nebula’s broadband energy spectrum and its apparent extension”. In: *A&A* 671, A67, A67. DOI: `10.1051/0004-6361/202243578`. arXiv: `2203.11502 [astro-ph.HE]`.

Domingo-Santamaria, E. et al. (Jan. 2005). “The DISP analysis method for point-like or extended gamma source searches/studies with the MAGIC Telescope”. In: *29th International Cosmic Ray Conference (ICRC29), Volume 5*. Ed. by B. Sripathi Acharya et al. Vol. 5. International Cosmic Ray Conference, p. 363.

Dominik, R. M. et al. (Sept. 2024). “Interpolation of Instrument Response Functions for the Cherenkov Telescope Array in the Context of pyirf”. In: *38th International Cosmic Ray Conference*, 618, p. 618.

Donath, Axel et al. (Oct. 2023). “Gammapy: A Python package for gamma-ray astronomy”. In: *A&A* 678, A157, A157. DOI: `10.1051/0004-6361/202346488`. arXiv: `2308.13584 [astro-ph.IM]`.

Doroshenko, Victor et al. (Dec. 2022). “Determination of X-ray pulsar geometry with IXPE polarimetry”. In: *Nature Astronomy* 6, pp. 1433–1443. DOI: `10.1038/s41550-022-01799-5`. arXiv: `2206.07138 [astro-ph.HE]`.

Erber, Thomas (Oct. 1966). “High-Energy Electromagnetic Conversion Processes in Intense Magnetic Fields”. In: *Reviews of Modern Physics* 38.4, pp. 626–659. DOI: `10.1103/RevModPhys.38.626`.

Evoli, Carmelo (Dec. 2020). *The Cosmic-Ray Energy Spectrum*. DOI: `10.5281/zenodo.4396125`. URL: `https://doi.org/10.5281/zenodo.4396125`.

Fermi LAT Collaboration et al. (Dec. 2009). “Modulated High-Energy Gamma-Ray Emission from the Microquasar Cygnus X-3”. In: *Science* 326.5959, p. 1512. DOI: `10.1126/science.1182174`.

Fierro, J. M. et al. (Feb. 1998). “Phase-resolved Studies of the High-Energy Gamma-Ray Emission from the Crab, Geminga, and VELA Pulsars”. In: *ApJ* 494.2, pp. 734–746. DOI: `10.1086/305219`. arXiv: `astro-ph/9709123 [astro-ph]`.

Fritz, G. et al. (May 1969). “X-ray Pulsar in the Crab Nebula”. In: *Science* 164.3880, pp. 709–712. DOI: `10.1126/science.164.3880.709`.

Fritz, Gilbert et al. (Mar. 1971). “The X-Ray Spectra of the Crab Nebula and NP 0532”. In: *ApJ* 164, p. L55. DOI: `10.1086/180691`.

Gaensler, Bryan M. and Patrick O. Slane (Sept. 2006). “The Evolution and Structure of Pulsar Wind Nebulae”. In: *ARA&A* 44.1, pp. 17–47. DOI: `10.1146/annurev.astro.44.051905.092528`. arXiv: `astro-ph/0601081 [astro-ph]`.

Garcia, Enrique, Thomas Vuillaume, and Lukas Nickel (Nov. 2022). “The lstMCpipe library”. In: *arXiv e-prints*, arXiv:2212.00120, arXiv:2212.00120. DOI: `10.48550/arXiv.2212.00120`. arXiv: `2212.00120 [astro-ph.IM]`.

Gendreau, Keith C., Zaven Arzoumanian, and Takashi Okajima (Sept. 2012). “The Neutron star Interior Composition ExploreR (NICER): an Explorer mission of opportunity for soft x-ray timing spectroscopy”. In: *Space Telescopes and Instrumentation 2012: Ultraviolet to Gamma Ray*. Ed. by Tadayuki Takahashi, Stephen S. Murray, and Jan-Willem A. den Herder. Vol. 8443. Society of Photo-Optical Instrumentation Engineers (SPIE) Conference Series, 844313, p. 844313. DOI: `10.1117/12.926396`.

Goldreich, Peter and William H. Julian (Aug. 1969). “Pulsar Electrodynamics”. In: *ApJ* 157, p. 869. DOI: `10.1086/150119`.

Greisen, K. et al. (1956). *Progress in Cosmic Ray Physics. Vol. 3*. Ed. by J. G. Wilson. North-Holland Publishing Co. URL: `https://books.google.es/books?id=V_E8ygAACAAJ`.

Grenier, Isabelle A. and Alice K. Harding (Aug. 2015). "Gamma-ray pulsars: A gold mine". In: *Comptes Rendus Physique* 16.6-7, pp. 641–660. DOI: `10.1016/j.crhy.2015.08.013`. arXiv: `1509.08823 [astro-ph.HE]`.

Gueta, O. (Mar. 2022). "The Cherenkov Telescope Array: layout, design and performance". In: *37th International Cosmic Ray Conference*, 885, p. 885. DOI: `10.22323/1.395.0885`. arXiv: `2108.04512 [astro-ph.IM]`.

H. E. S. S. Collaboration et al. (Dec. 2018). "First ground-based measurement of sub-20 GeV to 100 GeV γ-Rays from the Vela pulsar with H.E.S.S. II". In: *A&A* 620, A66, A66. DOI: `10.1051/0004-6361/201732153`. arXiv: `1807.01302 [astro-ph.HE]`.

H. E. S. S. Collaboration, H. Abdalla, et al. (Apr. 2018). "The H.E.S.S. Galactic plane survey". In: *A&A* 612, A1, A1. DOI: `10.1051/0004-6361/201732098`. arXiv: `1804.02432 [astro-ph.HE]`.

H. E. S. S. Collaboration, F. Aharonian, et al. (Nov. 2023). "Discovery of a radiation component from the Vela pulsar reaching 20 teraelectronvolts". In: *Nature Astronomy* 7, pp. 1341–1350. DOI: `10.1038/s41550-023-02052-3`. arXiv: `2310.06181 [astro-ph.HE]`.

Harding, Alice and Alexander Muslimov (June 2005). "Pulsar Slot Gaps and Unidentified Egret Sources". In: *Ap&SS* 297.1-4, pp. 63–70. DOI: `10.1007/s10509-005-7576-z`. arXiv: `astro-ph/0409047 [astro-ph]`.

Harding, Alice K. (Sept. 2013). "Pulsar Polar Cap and Slot Gap Models: Confronting Fermi Data". In: *Journal of Astronomy and Space Sciences* 30, pp. 145–152. DOI: `10.5140/JASS.2013.30.3.145`.

Harding, Alice K., Constantinos Kalapotharakos, et al. (Dec. 2018). "Multi-TeV Emission from the Vela Pulsar". In: *ApJ* 869.1, L18, p. L18. DOI: `10.3847/2041-8213/aaf3b2`. arXiv: `1811.11157 [astro-ph.HE]`.

Harding, Alice K., Christo Venter, and Constantinos Kalapotharakos (Dec. 2021). "Very-high-energy Emission from Pulsars". In: *ApJ* 923.2, 194, p. 194. DOI: `10.3847/1538-4357/ac3084`. arXiv: `2110.09412 [astro-ph.HE]`.

Hartman, R. C. et al. (July 1999). "The Third EGRET Catalog of High-Energy Gamma-Ray Sources". In: *ApJS* 123.1, pp. 79–202. DOI: `10.1086/313231`.

Heitler, W. (1954). *Quantum theory of radiation*.

Hess, Victor F. (1912). “Über Beobachtungen der durchdringenden Strahlung bei sieben Freiballonfahrten”. In: *Phys. Z.* 13, pp. 1084–1091.

Hillas, A. M. (Aug. 1985). “Cerenkov Light Images of EAS Produced by Primary Gamma Rays and by Nuclei”. In: *19th International Cosmic Ray Conference (ICRC19), Volume 3*. Ed. by F. C. Jones. Vol. 3. International Cosmic Ray Conference, p. 445.

Hirotani, Kouichi (Nov. 2008). “Outer-Gap versus Slot-Gap Models for Pulsar High-Energy Emissions: The Case of the Crab Pulsar”. In: *ApJ* 688.1, p. L25. DOI: `10.1086/595000`. arXiv: `0810.0865 [astro-ph]`.

— (Apr. 2013). “Luminosity Evolution of Gamma-Ray Pulsars”. In: *ApJ* 766.2, 98, p. 98. DOI: `10.1088/0004-637X/766/2/98`. arXiv: `1301.5717 [astro-ph.HE]`.

— (Jan. 2015). “Three-dimensional Non-vacuum Pulsar Outer-gap Model: Localized Acceleration Electric Field in the Higher Altitudes”. In: *ApJ* 798.2, L40, p. L40. DOI: `10.1088/2041-8205/798/2/L40`. arXiv: `1412.2876 [astro-ph.HE]`.

Hoffmann, Dirk and Julien Houles (Dec. 2012). “Prototyping a 10 Gigabit-Ethernet Event-Builder for the CTA Camera Server”. In: *Journal of Physics Conference Series*. Vol. 396. Journal of Physics Conference Series, 012024, p. 012024. DOI: `10.1088/1742-6596/396/1/012024`.

Holler, M. et al. (Sept. 2015). “Observations of the Crab Nebula with H.E.S.S. Phase II”. In: *arXiv e-prints*, arXiv:1509.02902, arXiv:1509.02902. DOI: `10.48550/arXiv.1509.02902`. arXiv: `1509.02902 [astro-ph.HE]`.

Holloway, N. J. and M. H. L. Pryce (Jan. 1981). “Properties of gaps in pulsar magnetospheres”. In: *MNRAS* 194, pp. 95–110. DOI: `10.1093/mnras/194.1.95`.

Huentemeyer, Petra et al. (Sept. 2019). “The Southern Wide-Field Gamma-Ray Observatory (SWGO): A Next-Generation Ground-Based Survey Instrument”. In: *Bulletin of the American Astronomical Society*. Vol. 51, 109, p. 109. DOI: `10.48550/arXiv.1907.07737`. arXiv: `1907.07737 [astro-ph.IM]`.

IceCube Collaboration et al. (July 2018). “Neutrino emission from the direction of the blazar TXS 0506+056 prior to the IceCube-170922A alert”. In: *Science* 361.6398, pp. 147–151. DOI: `10.1126/science.aat2890`. arXiv: `1807.08794 [astro-ph.HE]`.

Illiano, G. et al. (Jan. 2023). “Investigating the origin of optical and X-ray pulsations of the transitional millisecond pulsar PSR J1023+0038”. In: *A&A* 669, A26, A26. DOI: `10.1051/0004-6361/202244637`. arXiv: `2211.12975 [astro-ph.HE]`.

Kawata, K. and Tibet ASgamma Collaboration (July 2019). “100 TeV Gamma-Ray Observation of the Crab Nebula with the Tibet Air Shower Array”. In: *36th International Cosmic Ray Conference (ICRC2019)*. Vol. 36. International Cosmic Ray Conference, 712, p. 712. DOI: `10.22323/1.358.0712`.

Kierans, Carolyn, Tadayuki Takahashi, and Gottfried Kanbach (2022). “Compton Telescopes for Gamma-Ray Astrophysics”. In: *Handbook of X-ray and Gamma-ray Astrophysics*. Ed. by Cosimo Bambi and Andrea Sangangelo, 18, p. 18. DOI: `10.1007/978-981-16-4544-0_46-1`.

Kierans, Carolyn A. (Jan. 2021). “AMEGO: exploring the extreme multimessenger universe”. In: *Society of Photo-Optical Instrumentation Engineers (SPIE) Conference Series*. Ed. by Jan-Willem A. den Herder, Shouleh Nikzad, and Kazuhiro Nakazawa. Vol. 11444. Society of Photo-Optical Instrumentation Engineers (SPIE) Conference Series, 1144431, p. 1144431. DOI: `10.1117/12.2562352`. arXiv: `2101.03105 [astro-ph.IM]`.

Klebesadel, Ray W., Ian B. Strong, and Roy A. Olson (June 1973). “Observations of Gamma-Ray Bursts of Cosmic Origin”. In: *ApJ* 182, p. L85. DOI: `10.1086/181225`.

Kniffen, D. A. et al. (Oct. 1974). “Gamma radiation from the Crab Nebula above 35 MeV”. In: *Nature* 251.5474, pp. 397–399. DOI: `10.1038/251397a0`.

Kobayashi, Y. et al. (Mar. 2022). “Camera Calibration of the CTA-LST prototype”. In: *37th International Cosmic Ray Conference*, 720, p. 720. DOI: `10.22323/1.395.0720`. arXiv: `2108.05035 [astro-ph.IM]`.

Kraushaar, W. L., G. W. Clark, and G. Garmire (Feb. 1969). “OSO-III High-Energy Gamma-Ray Experiment”. In: *Sol. Phys.* 6.2, pp. 228–234. DOI: `10.1007/BF00150947`.

Kraushaar, W. L., G. W. Clark, G. P. Garmire, et al. (Nov. 1972). “High-Energy Cosmic Gamma-Ray Observations from the OSO-3 Satellite”. In: *ApJ* 177, p. 341. DOI: `10.1086/151713`.

Kraushaar, William L. and George W. Clark (May 1962). “Gamma Ray Astronomy”. In: *Scientific American* 206.5, pp. 52–61. DOI: `10.1038/scientificamerican0562-52`.

Kuiper, L. et al. (Nov. 2001). “The Crab pulsar in the 0.75-30 MeV range as seen by CGRO COMPTEL. A coherent high-energy picture from soft X-rays up to high-energy gamma-rays”. In: *A&A* 378, pp. 918–935. DOI: `10.1051/0004-6361:20011256`. arXiv: `astro-ph/0109200 [astro-ph]`.

Lewis, D. A. (July 1990). “Optical characteristics of the whipple observatory TeV gamma-ray imaging telescope”. In: *Experimental Astronomy* 1.4, pp. 213–226. DOI: `10.1007/BF00428516`.

Lhaaso Collaboration et al. (July 2021). “Peta-electron volt gamma-ray emission from the Crab Nebula”. In: *Science* 373, pp. 425–430. DOI: `10.1126/science.abg5137`. arXiv: `2111.06545 [astro-ph.HE]`.

Li, T. -P. and Y. -Q. Ma (Sept. 1983). “Analysis methods for results in gamma-ray astronomy.” In: *ApJ* 272, pp. 317–324. DOI: `10.1086/161295`.

Linden, Tim et al. (Nov. 2017). “Using HAWC to discover invisible pulsars”. In: *Phys. Rev. D* 96.10, 103016, p. 103016. DOI: `10.1103/PhysRevD.96.103016`. arXiv: `1703.09704 [astro-ph.HE]`.

Linhoff, Maximilian et al. (Sept. 2023). *cta-observatory/pyirf: v0.10.1 – 2023-09-15*. Version v0.10.1. DOI: `10.5281/zenodo.8348922`.

Lopez, M. et al. (July 2009). “Detection of the crab pulsar with MAGIC”. In: *arXiv e-prints*, arXiv:0907.0832, arXiv:0907.0832. DOI: `10.48550/arXiv.0907.0832`. arXiv: `0907.0832 [astro-ph.HE]`.

López-Coto, Ruben et al. (July 2022). “lstchain: An Analysis Pipeline for LST-1, the First Prototype Large-Sized Telescope of CTA”. In: *Astronomical Data Analysis Software and Systems XXX*. Ed. by Jose Enrique Ruiz, Francesco Pierfedereci, and Peter Teuben. Vol. 532. Astronomical Society of the Pacific Conference Series, p. 357.

Lovelace, R. V. E., J. M. Sutton, and H. D. Craft (Nov. 1968). “Pulsar NP 0532 Near Crab Nebula”. In: *IAU Circ.* 2113, p. 1.

Luo, Jing et al. (Feb. 2019). *PINT: High-precision pulsar timing analysis package*. Astrophysics Source Code Library, record ascl:1902.007.

Lyne, A. G., C. A. Jordan, et al. (Jan. 2015). “45 years of rotation of the Crab pulsar”. In: *MNRAS* 446.1, pp. 857–864. DOI: `10.1093/mnras/stu2118`. arXiv: `1410.0886 [astro-ph.HE]`.

Lyne, A. G., R. S. Pritchard, and F. Graham Smith (Dec. 1993). “23 years of Crab pulsar rotational history.” In: *MNRAS* 265, pp. 1003–1012. DOI: `10.1093/mnras/265.4.1003`.

Maggiore, Michele (2007). *Gravitational Waves: Volume 1: Theory and Experiments*. DOI: `10.1093/acprof:oso/9780198570745.001.0001`.

MAGIC Collaboration et al. (Nov. 2020a). “Detection of the Geminga pulsar with MAGIC hints at a power-law tail emission beyond 15 GeV”. In: *A&A* 643, L14, p. L14. DOI: `10.1051/0004-6361/202039131`. arXiv: `2011.10412 [astro-ph.HE]`.

— (Mar. 2020b). “MAGIC very large zenith angle observations of the Crab Nebula up to 100 TeV”. In: *A&A* 635, A158, A158. DOI: `10.1051/0004-6361/201936899`. arXiv: `2001.09566 [astro-ph.HE]`.

MAGIC Collaboration et al. (Nov. 2019). “Teraelectronvolt emission from the γ-ray burst GRB 190114C”. In: *Nature* 575.7783, pp. 455–458. DOI: `10.1038/s41586-019-1750-x`. arXiv: `2006.07249 [astro-ph.HE]`.

Marelli, M. et al. (Apr. 2015). “Radio-quiet and Radio-loud Pulsars: Similar in Gamma-Rays but Different in X-Rays”. In: *ApJ* 802.2, 78, p. 78. DOI: `10.1088/0004-637X/802/2/78`. arXiv: `1501.06215 [astro-ph.HE]`.

Mas, Alvaro and Daniel Morcuende (Aug. 2024). *cta-observatory/PulsarTimingAnalysis: v0.5*. Version v0.5. DOI: `10.5281/zenodo.13385378`. URL: `https://doi.org/10.5281/zenodo.13385378`.

Mas Aguilar, Álvaro (2025). “Search for very high energy emission from pulsars with LST-1 telescope”. English. Advisor: Marcos López Moya. Doctoral thesis. Madrid, Spain: Universidad Complutense de Madrid. URL: `https://hdl.handle.net/20.500.14352/122413`.

McCann, A. (May 2015). “A Stacked Analysis of 115 Pulsars Observed by the FERMI LAT”. In: *ApJ* 804.2, 86, p. 86. DOI: `10.1088/0004-637X/804/2/86`. arXiv: `1412.2422 [astro-ph.HE]`.

Meagher, K. and VERITAS Collaboration (July 2015). “Six years of VERITAS observations of the Crab Nebula”. In: *34th International Cosmic Ray Conference (ICRC2015)*. Vol. 34. International Cosmic Ray Conference, 792, p. 792. DOI: `10.22323/1.236.0792`. arXiv: `1508.06442 [astro-ph.HE]`.

Menchiari, S. et al. (Mar. 2025). “Contribution of young massive stellar clusters to the Galactic diffuse γ-ray emission”. In: *A&A* 695, A175, A175. DOI: `10.1051/0004-6361/202450621`. arXiv: `2406.04087 [astro-ph.HE]`.

Mignani, R. P., N. Rea, et al. (Oct. 2016). “Observations of three young γ-ray pulsars with the Gran Telescopio Canarias”. In: *MNRAS* 461.4, pp. 4317–4328. DOI: `10.1093/mnras/stw1629`. arXiv: `1606.04711 [astro-ph.HE]`.

Mignani, R. P., V. Testa, M. Marelli, A. De Luca, M. Pierbattista, et al. (Dec. 2016). “Searching for the optical counterparts of two young γ-ray pulsars”. In: *MNRAS* 463.3, pp. 2932–2938. DOI: `10.1093/mnras/stw2226`. arXiv: `1607.04995 [astro-ph.HE]`.

Mignani, R. P., V. Testa, M. Marelli, A. De Luca, D. Salvetti, et al. (July 2016). “A Candidate Optical Counterpart to the Middle Aged γ-RAY Pulsar PSRJ1741-2054”. In: *ApJ* 825.2, 151, p. 151. DOI: `10.3847/0004-637X/825/2/151`. arXiv: `1605.02786 [astro-ph.HE]`.

Mineo, T., G. Cusumano, et al. (Nov. 1997). “A BeppoSAX observation of the Crab Pulsar (PSR B0531+21)”. In: *A&A* 327, pp. L21–L24.

Mineo, T., C. Ferrigno, et al. (May 2006). “INTEGRAL observations of the Crab pulsar”. In: *A&A* 450.2, pp. 617–623. DOI: `10.1051/0004-6361:20054305`. arXiv: `astro-ph/0601641 [astro-ph]`.

Mirzoyan, R. (Jan. 1997). “On the Calibration Accuracy of Light Sensors in Atmospheric Cherenkov Fluorescence and Neutrino Experiments”. In: *International Cosmic Ray Conference*. Vol. 7. International Cosmic Ray Conference, p. 265.

Mochol, Iwona (Jan. 2017). “Pulsar Striped Winds”. In: *Modelling Pulsar Wind Nebulae*. Ed. by Diego F. Torres. Vol. 446. Astrophysics and Space Science Library, p. 135. DOI: `10.1007/978-3-319-63031-1_7`. arXiv: `1702.00720 [astro-ph.HE]`.

Moralejo et al. (Feb. 2025). *cta-observatory/cta-lstchain: v0.10.18 – 2025-02-17*. Zenodo. DOI: `10.5281/zenodo.14883336`. URL: `https://doi.org/10.5281/zenodo.14883336`.

Morrison, P. (Mar. 1958). “On gamma-ray astronomy”. In: *Il Nuovo Cimento* 7.6, pp. 858–865. DOI: `10.1007/BF02745590`.

Nather, R. E., B. Warner, and M. Macfarlane (Feb. 1969). “Optical Pulsations in the Crab Nebula Pulsar”. In: *Nature* 221.5180, pp. 527–529. DOI: `10.1038/221527a0`.

Naurois, Mathieu de (Mar. 2012). “Very High Energy astronomy from H.E.S.S. to CTA. Opening of a new astronomical window on the non-thermal Universe”. Accreditation to supervise research. Université Pierre et Marie Curie - Paris VI. URL: `https://theses.hal.science/tel-00687872`.

Nepomuk Otte, A. (Dec. 2007). “Observation of the Crab Nebula with the MAGIC telescope”. In: *arXiv e-prints*, arXiv:0712.1386, arXiv:0712.1386. DOI: `10.48550/arXiv.0712.1386`. arXiv: `0712.1386 [astro-ph]`.

Nguyen, T. and VERITAS Collaboration (July 2015). "Updated results from VERITAS on the Crab pulsar". In: *34th International Cosmic Ray Conference (ICRC2015)*. Vol. 34. International Cosmic Ray Conference, 828, p. 828. DOI: `10.22323/1.236.0828`. arXiv: `1508.07268 [astro-ph.HE]`.

Noethe, M. et al. (Mar. 2022). "Prototype Open Event Reconstruction Pipeline for the Cherenkov Telescope Array". In: *37th International Cosmic Ray Conference*, 744, p. 744. DOI: `10.22323/1.395.0744`. arXiv: `2110.11097 [astro-ph.IM]`.

Nolan, P. L. et al. (June 1993). "Observations of the Crab Pulsar and Nebula by the EGRET Telescope on the Compton Gamma-Ray Observatory". In: *ApJ* 409, p. 697. DOI: `10.1086/172699`.

Ohm, Stefan (June 2016). "Starburst galaxies as seen by gamma-ray telescopes". In: *Comptes Rendus Physique* 17.6, pp. 585–593. DOI: `10.1016/j.crhy.2016.04.003`.

Oppenheimer, J. R. and G. M. Volkoff (Feb. 1939). "On Massive Neutron Cores". In: *Physical Review* 55.4, pp. 374–381. DOI: `10.1103/PhysRev.55.374`.

Pacini, F. (Nov. 1967). "Energy Emission from a Neutron Star". In: *Nature* 216.5115, pp. 567–568. DOI: `10.1038/216567a0`.

Pathania, Atul, Krishna Kumar Singh, and Kuldeep Kumar Yadav (Aug. 2023). "Gamma Ray Pulsars and Opportunities for the MACE Telescope". In: *Galaxies* 11.4, 91, p. 91. DOI: `10.3390/galaxies11040091`.

Pétri, Jérôme (Aug. 2012). "High-energy emission from the pulsar striped wind: a synchrotron model for gamma-ray pulsars". In: *MNRAS* 424.3, pp. 2023–2027. DOI: `10.1111/j.1365-2966.2012.21350.x`. arXiv: `1205.5101 [astro-ph.HE]`.

— (Oct. 2016). "Theory of pulsar magnetosphere and wind". In: *Journal of Plasma Physics* 82.5, 635820502, p. 635820502. DOI: `10.1017/S0022377816000763`. arXiv: `1608.04895 [astro-ph.HE]`.

Philippov, A. and M. Kramer (Aug. 2022). "Pulsar Magnetospheres and Their Radiation". In: *ARA&A* 60, pp. 495–558. DOI: `10.1146/annurev-astro-052920-112338`.

Philippov, Alexander, Andrey Timokhin, and Anatoly Spitkovsky (June 2020). "Origin of Pulsar Radio Emission". In: *Phys. Rev. Lett.* 124.24, 245101, p. 245101. DOI: `10.1103/PhysRevLett.124.245101`. arXiv: `2001.02236 [astro-ph.HE]`.

Philippov, Anatoly Spitkovsky, and Benoit Cerutti (Mar. 2015). "Ab Initio Pulsar Magnetosphere: Three-dimensional Particle-in-cell Simulations of Oblique Pulsars". In:

ApJ 801.1, L19, p. L19. DOI: 10.1088/2041-8205/801/1/L19. arXiv: 1412.0673 [astro-ph.HE].

Potekhin, A. Yu (Aug. 2014). "Atmospheres and radiating surfaces of neutron stars". In: *Physics Uspekhi* 57.8, 735-770, pp. 735–770. DOI: 10.3367/UFNe.0184.201408a.0793. arXiv: 1403.0074 [astro-ph.SR].

Pravdo, Steven H., Lorella Angelini, and Alice K. Harding (Dec. 1997). "X-Ray Spectral Evolution of the Crab Pulse". In: *ApJ* 491.2, pp. 808–815. DOI: 10.1086/304996.

Punch, M. et al. (Aug. 1992). "Detection of TeV photons from the active galaxy Markarian 421". In: *Nature* 358.6386, pp. 477–478. DOI: 10.1038/358477a0.

Quinn, J. et al. (Jan. 1996). "Detection of Gamma Rays with E > 300 GeV from Markarian 501". In: *ApJ* 456, p. L83. DOI: 10.1086/309878.

Romani, Roger W. (Oct. 1996). "Gamma-Ray Pulsars: Radiation Processes in the Outer Magnetosphere". In: *ApJ* 470, p. 469. DOI: 10.1086/177878.

Ruderman, M. A. and P. G. Sutherland (Feb. 1975). "Theory of pulsars: polar gaps, sparks, and coherent microwave radiation." In: *ApJ* 196, pp. 51–72. DOI: 10.1086/153393.

Rybicki, George B. and Alan P. Lightman (1979). *Radiative processes in astrophysics*.

Schoenfelder, V. et al. (June 1993). "Instrument Description and Performance of the Imaging Gamma-Ray Telescope COMPTEL aboard the Compton Gamma-Ray Observatory". In: *ApJS* 86, p. 657. DOI: 10.1086/191794.

Schonfelder, V. (May 1995). "A survey of COMPTEL results". In: *Advances in Space Research* 15.5, pp. 1–12. DOI: 10.1016/0273-1177(94)00027-X.

Schönfelder, V. (July 2002). "The history of gamma-ray astronomy". In: *Astronomische Nachrichten* 323.6, pp. 524–529. DOI: 10.1002/1521-3994(200212)323:6<524::AID-ASNA524>3.0.CO;2-Z.

Sitarek, Julian et al. (Sept. 2013). "Analysis techniques and performance of the Domino Ring Sampler version 4 based readout for the MAGIC telescopes". In: *Nuclear Instruments and Methods in Physics Research A* 723, pp. 109–120. DOI: 10.1016/j.nima.2013.05.014. arXiv: 1305.1007 [astro-ph.IM].

Smith, D. A. et al. (Dec. 2023). "The Third Fermi Large Area Telescope Catalog of Gamma-Ray Pulsars". In: *ApJ* 958.2, 191, p. 191. DOI: 10.3847/1538-4357/acee67. arXiv: 2307.11132 [astro-ph.HE].

Spir-Jacob, M. et al. (July 2019). “H.E.S.S. Observations of Pulsars at Very High Energies”. In: *36th International Cosmic Ray Conference (ICRC2019)*. Vol. 36. International Cosmic Ray Conference, 799, p. 799. DOI: 10.22323/1.358.0799.

Spitkovsky, Anatoly (Sept. 2006). “Time-dependent Force-free Pulsar Magnetospheres: Axisymmetric and Oblique Rotators”. In: *ApJ* 648.1, pp. L51–L54. DOI: 10.1086/507518. arXiv: astro-ph/0603147 [astro-ph].

Staelin, David H. and Edward C. Reifenstein III (Dec. 1968). “Pulsating Radio Sources near the Crab Nebula”. In: *Science* 162.3861, pp. 1481–1483. DOI: 10.1126/science.162.3861.1481.

Stoop, M. et al. (Feb. 2023). “The early evolution of young massive clusters. The kinematic history of NGC 6611/M16”. In: *A&A* 670, A108, A108. DOI: 10.1051/0004-6361/202244511. arXiv: 2207.08452 [astro-ph.GA].

Su, Meng, Tracy R. Slatyer, and Douglas P. Finkbeiner (Dec. 2010). “Giant Gamma-ray Bubbles from Fermi-LAT: Active Galactic Nucleus Activity or Bipolar Galactic Wind?” In: *ApJ* 724.2, pp. 1044–1082. DOI: 10.1088/0004-637X/724/2/1044. arXiv: 1005.5480 [astro-ph.HE].

Sudoh, Takahiro, Tim Linden, and John F. Beacom (Aug. 2019). “TeV halos are everywhere: Prospects for new discoveries”. In: *Phys. Rev. D* 100.4, 043016, p. 043016. DOI: 10.1103/PhysRevD.100.043016. arXiv: 1902.08203 [astro-ph.HE].

Taylor, J. H. and R. N. Manchester (Jan. 1977). “Recent observations of pulsars.” In: *ARA&A* 15, pp. 19–44. DOI: 10.1146/annurev.aa.15.090177.000315.

Taylor, John R. (1982). *An introduction to error analysis. The study of uncertainties in physical measurements*.

Tejedor, Luis A. et al. (Mar. 2022). “A Trigger Interface Board for the Large and Medium Sized telescopes of the Cherenkov Telescope Array”. In: *Nuclear Instruments and Methods in Physics Research A* 1027, 166058, p. 166058. DOI: 10.1016/j.nima.2021.166058.

Ter Haar, D. (Apr. 1950). “Cosmogonical Problems and Stellar Energy”. In: *Reviews of Modern Physics* 22.2, pp. 119–152. DOI: 10.1103/RevModPhys.22.119.

Thompson, D. J. (Nov. 2008). “Gamma ray astrophysics: the EGRET results”. In: *Reports on Progress in Physics* 71.11, 116901, p. 116901. DOI: 10.1088/0034-4885/71/11/116901. arXiv: 0811.0738 [astro-ph].

Thompson, David J. and Alexander A. Moiseev (2022). “Pair Production Detectors for Gamma-Ray Astrophysics”. In: *Handbook of X-ray and Gamma-ray Astrophysics*. Ed. by Cosimo Bambi and Andrea Sangangelo, 54, p. 54. DOI: `10.1007/978-981-16-4544-0_159-1`.

Tibet ASγ Collaboration et al. (Jan. 2021). “Potential PeVatron supernova remnant G106.3+2.7 seen in the highest-energy gamma rays”. In: *Nature Astronomy* 5, pp. 460–464. DOI: `10.1038/s41550-020-01294-9`. arXiv: `2109.02898 [astro-ph.HE]`.

Tomsick, John and COSI Team (May 2024). “The COSI Mission Overview”. In: *AAS High Energy Astrophysics Division Meeting #21*. Vol. 21. AAS/High Energy Astrophysics Division, 406.03, p. 406.03.

Toor, A. and F. D. Seward (Sept. 1977). “Observation of X-rays from the Crab pulsar.” In: *ApJ* 216, pp. 560–564. DOI: `10.1086/155497`.

Vecchiotti, Vittoria et al. (Nov. 2024). “Interpreting the LHAASO Galactic diffuse emission data”. In: *arXiv e-prints*, arXiv:2411.11439, arXiv:2411.11439. DOI: `10.48550/arXiv.2411.11439`. arXiv: `2411.11439 [astro-ph.HE]`.

Vercellone, S. et al. (Aug. 2022). “ASTRI Mini-Array core science at the Observatorio del Teide”. In: *Journal of High Energy Astrophysics* 35, pp. 1–42. DOI: `10.1016/j.jheap.2022.05.005`. arXiv: `2208.03177 [astro-ph.HE]`.

VERITAS Collaboration (Oct. 2011). “Detection of Pulsed Gamma Rays Above 100 GeV from the Crab Pulsar”. In: *Science* 334.6052, p. 69. DOI: `10.1126/science.1208192`. arXiv: `1108.3797 [astro-ph.HE]`.

Wakely, S. P. and D. Horan (2008). “TeVCat: An online catalog for Very High Energy Gamma-Ray Astronomy”. In: *International Cosmic Ray Conference* 3, pp. 1341–1344.

Weekes, T. C. et al. (July 1989). “Observation of TeV Gamma Rays from the Crab Nebula Using the Atmospheric Cerenkov Imaging Technique”. In: *ApJ* 342, p. 379. DOI: `10.1086/167599`.

Winston, E. et al. (Dec. 2011). “The Structure of the Star-forming Cluster RCW 38”. In: *ApJ* 743.2, 166, p. 166. DOI: `10.1088/0004-637X/743/2/166`. arXiv: `1110.2660 [astro-ph.SR]`.

Yan, Lin-Li et al. (Apr. 2022). “A Study on the X-Ray Pulse Profile and Spectrum of the Crab Pulsar Using NICER and Insight-HXMT’s Observations”. In: *ApJ* 928.2, 183, p. 183. DOI: `10.3847/1538-4357/ac581c`. arXiv: `2204.05828 [astro-ph.HE]`.

Yang, H. -Y. Karen, Mateusz Ruszkowski, and Ellen G. Zweibel (Feb. 2018). “Unveiling the Origin of the Fermi Bubbles”. In: *Galaxies* 6.1, 29, p. 29. DOI: `10.3390/galaxies6010029`. arXiv: `1802.03890 [astro-ph.HE]`.

Zhang, Rui et al. (Nov. 2023). “Galactic Diffuse γ-Ray Emission from GeV to PeV Energies in Light of Up-to-date Cosmic-Ray Measurements”. In: *ApJ* 957.1, 43, p. 43. DOI: `10.3847/1538-4357/acf842`. arXiv: `2305.06948 [astro-ph.HE]`.

Acknowledgments

I would first like to express my deepest gratitude to my supervisor, Elisa Prandini, whose guidance, support, and continuous encouragement made this work possible. I am also grateful to the University of Padova and to the Consejo Superior de Investigaciones Científicas for providing me with the opportunity and resources to pursue this research. My sincere thanks go to the VHEGA research group at the Instituto de Astrofísica de Andalucía in Granada, in particular to my supervisors, Rubén López Coto and Stefano Menchiari, for their mentorship and valuable advice, as well as to all the members of the group for creating such a stimulating and collaborative environment.

Finally, I wish to extend my heartfelt gratitude to my family, my friends, and all the people who have accompanied and supported me throughout this journey.